Active Magnetic Regenerator Experimental Optimization

by

Armando Tura
Bachelor in Engineering, University of Victoria, 2002

A Dissertation Submitted in Partial fulfillment of the Requirements for the Degree of

MASTER OF APPLIED SCIENCE

in the

Department of Mechanical Engineering

Active Magnetic Regenerator Experimental Optimization

by

Armando Tura
Bachelor in Engineering, University of Victoria, 2002

Supervisory Committee:

Dr. Andrew Rowe	(Department of Mechanical Engineering)
Supervisor	
Dr. Sadik Dost	(Department of Mechanical Engineering)
Department Member	
Dr. Peter Oshkai	(Department of Mechanical Engineering)
Department Member	

Supervisory Committee:

Dr. Andrew Rowe	(Department of Mechanical Engineering)
Supervisor	
Dr. Sadik Dost	(Department of Mechanical Engineering)
Department Member	
Dr. Peter Oshkai	(Department of Mechanical Engineering)
Department Member	

Abstract

A technology that has the potential to create more efficient and compact refrigeration devices is an Active Magnetic Regenerative Refrigerator (AMRR). An AMRR can operate over a broad range of temperatures, as long as the appropriate refrigerant is implemented. Thus this flexible technology can be used for small, efficient, and simple room temperature refrigerators, as well as efficient gas liquefaction plants (AMRLs). Active Magnetic Regenerator Refrigeration exploits the magnetocaloric effect displayed by magnetic materials whereby a reversible temperature change is induced when the material is exposed to a magnetic field. By using the magnetic materials in a regenerator as the heat storage medium and as the means of work input, one creates an Active Magnetic Regenerator (AMR).

In this work, an experimental study of Active Magnetic Regenerators composed of single and multi-materials is carried out. AMRs made up of Gd, $Gd_{.74}Tb_{.26}$, and $Gd_{.85}Er_{.15}$ are studied in cycles rejecting heat between 270 K and 311 K. A variety of operating conditions were tested and regenerator performance with respect to heat load, utilization, and frequency was examined. AMR behavior was qualitatively interpreted and a path for performance improvement and future investigations laid.

Table of Contents

Table of Contents iv
List of Figures vi
List of Tables x
Nomenclature xi
Acronyms xi
Symbols xi
Subscripts xii
Chapter 1 Introduction 1
1.1 Motivation 1
1.2 Magnetic Refrigeration 1
1.2.1 Key Parameters 6
1.2.2 Temperature Profile and Cooling Power 6
1.2.3 Layering 7
1.3 Objectives 9
Chapter 2 Magnetic Refrigeration Theory 10
2.1 The Magnetocaloric Effect 10
2.2 Materials 12
2.3 AMR Theory 15
Chapter 3 Apparatus Overview 22
3.1 Design Challenges 22
3.2 The AMRTA 22
3.2.1 Apparatus Design 23
3.2.2 Instrumentation 32
3.2.3 Upgrades 33
Chapter 4 Experimental Results 37
4.1 Single Layer Regenerators 38
4.1.1 Methodology 38
4.2 Multi-Layered Regenerators 44
4.2.1 Multiple Layer Experimental Strategy and Results 45
Chapter 5 Discussion 58
5.1 Parameter Sensitivity Study 58

5.2 Predicting Layered AMR Performance 73
5.3 Heat Leaks 79
5.3.1 Finite Element Analysis (FEA) 80
5.4 Initial conditions 82
Chapter 6 Conclusions 86
6.1 Single Material Bed 86
6.2 Layered Material Bed 87
6.3 Recommendations 88
References 89
Appendix A - Instrumentation A-1
Appendix B- Sample Data Log B-1

List of Figures

Figure 1-1. Magnetocaloric effect of Gd for a 0-2 T applied field change [1]. 2

Figure 1-2. The AMR temperature profile at periodic steady state [1]. 5

Figure 1-3. The ideal MCE as compared to gadolinium with a 0-2 T field change (Material A), and another material with a Curie temperature near 265 K (Material B)..... 8

Figure 2-1. Graphical representation of the MCE [9]. 10

Figure 2-2. MCE as function of temperature for Gd, $Gd_{.74}Tb_{.26}$, and $G_{.85}Er_{.15}$ for 0-2 T.. 13

Figure 2-3. Specific heat vs temperature for Gd, $Gd_{.74}Tb_{.26}$, and $G_{.85}Er_{.15}$ at 0 T [11]. ... 14

Figure 2-4. Specific heat vs temperature for Gd, $Gd_{.74}Tb_{.26}$, and $G_{.85}Er_{.15}$ at 2 T [11]. ... 14

Figure 2-5. A schematic representation of an AMR showing the net work and heat flux at a differential section [3]. 15

Figure 2-6. Hypothetical cycle for the magnetic refrigerant at some cross-section of the AMR [3]. 16

Figure 3-1. Magnet internal assembly (coldbox not shown) [3]. 23

Figure 3-2. $\mu_0 H_a(z)$ normalized distribution along Z axis. 24

Figure 3-3. Phasing among field, transfer fluid flow, and regenerator linear velocity. 26

Figure 3-4. AMRTA layout. 26

Figure 3-5. AMRTA assembly. 26

Figure 3-6. Schematic of the gas transfer and cooling fluid system for the AMR Test Apparatus. 27

Figure 3-7. Internal cross-section of the Festo fluid displacer. 28

Figure 3-8. Cylinder assembly. 29

Figure 3-9. Cylinder internal layout. 30

Figure 3-10. Single, two, and three puck regenerators..... 30

Figure 4-1. Temperature as function of time for a Gd-$Gd_{.74}Tb_{.26}$ two layer regenerator. 37

Figure 4-2. Pressure and utilization relationship for 10 atm, single puck AMR. 40

Figure 4-3. Gadolinium single puck regenerator temperature span versus pressure at various T_H. 40

Figure 4-4. Gadolinium single puck regenerator temperature span as T_H is varied at 0.65 Hz and pressures of 3, 6, and atm. 41

Figure 4-5. Gd, $Gd_{.74}Tb_{.26}$ and $Gd_{.85}Er_{.15}$ single puck temperature span versus T_H with no load at 0.65 Hz and 9.5 atm. 42

Figure 4-6. Gd single puck temperature span versus heat load at 0.8 Hz and 9.5 atm.. 43

Figure 4-7. Gd single puck temperature span for 0 and 6 W at 0.8 Hz and 9.5 and 4.75 atm. 43

Figure 4-8. Pressure drop for a single puck AMR at room temperature. 44

Figure 4-9. Gd-Gd AMR temperature span versus T_H at 9.5 atm and 0.65 Hz. 47

Figure 4-10. Gd-Gd AMR temperature distribution versus T_H at 9.5 atm and 0.65 Hz... 48

Figure 4-11. Gd-Gd heat load sensitivity curves. 48

Figure 4-12. Gd-$Gd_{.74}Tb_{.26}$ AMR temperature span versus T_H at 9.5 atm and 0.65 Hz.. 49

Figure 4-13. Gd-$Gd_{.74}Tb_{.26}$ hot, cold and interface T versus T_H at 9.5 atm and 0.65 Hz. 50

Figure 4-14. Gd-$Gd_{.74}Tb_{.26}$ temperature span versus T_H at 9.7, 8, 5 atm and 0.65 Hz with one o-ring missing. 51

Figure 4-15. Gd-$Gd_{.74}Tb_{.26}$ frequency sensitivity test at 9.7 atm and T_H = 304 K for temperature span and pressure drop. 52

Figure 4-16. Gd-$Gd_{.74}Tb_{.26}$ heat load sensitivity at 9.7 atm, T_H = 306 K and 0.8 Hz..... 52

Figure 4-17. Gd-$Gd_{.85}Er_{.15}$ AMR temperature span versus T_H at 9.5 atm and 0.65 Hz... 53

Figure 4-18. Gd-$Gd_{.85}Er_{.15}$ hot, cold and interface temperatures vs T_H at 9.5 atm and 0.65 Hz. 54

Figure 4-19. Gd-$Gd_{.85}Er_{.15}$ heat load sensitivity at 9.5 atm, T_H = 306, 298, 290 K and 0.8 Hz. 54

Figure 4-20. Gd-$Gd_{.74}Tb_{.26}$-$Gd_{.85}Er_{.15}$ temperature span versus T_H at 9.5, 6, 3 atm and 0.65 Hz. 56

Figure 4-21. Gd-$Gd_{.74}Tb_{.26}$-$Gd_{.85}Er_{.15}$ hot, cold and interface temperatures versus T_H at 9.5 atm and 0.65 Hz. 56

Figure 4-22. Gd-$Gd_{.74}Tb_{.26}$-$Gd_{.85}Er_{.15}$ heat load sensitivity curves. 57

Figure 5-1. Summary of no-load 9.5 atm and 0.65 Hz results. 58

Figure 5-2. Ideal Gadolinium MCE compared to real MCE and single puck AMR data. 59

Figure 5-3. Heat load sensitivity as function of T_H for several AMRs tested. 61

Figure 5-4. Gd AMR temperature span sensitivity to pressure as a function of T_H. 62

Figure 5-5. Gd AMR temperature span sensitivity to pressure as function of operating pressure. 63

Figure 5-6. Temperature span sensitivity to frequency as function of T_H at 0.65 Hz..... 64

Figure 5-7. Gd-Gd and Gd temperature span vs T_H. 66

Figure 5-8. Temperature span sensitivity to pressure as a function of operating pressure for the Gd, Gd-Gd, and Gd-$Gd_{.74}Tb_{.26}$-$Gd_{.85}Er_{.15}$ AMRs. 67

Figure 5-9. Gd-Gd, $Gd_{.74}Tb_{.26}$, and Gd temperature span vs T_H. 68

Figure 5-10. $Gd_{.74}Tb_{.26}$ AMR and $Gd_{.74}Tb_{.26}$ temperature span bottom layer versus T_H and $T_{interface}$ respectively. 68

Figure 5-11. Gd-Gd, $Gd_{.74}Tb_{.26}$, Gd-$Gd_{.85}Er_{.15}$, and Gd temperature spans vs T_H. 69

Figure 5-12. $Gd_{.85}Er_{.15}$ AMR, and $Gd_{.85}Er_{.15}$ cold layer temperature span vs T_H and $T_{interface}$ respectively. 70

Figure 5-13. Gd, Gd-Gd, Gd-$Gd_{.74}Tb_{.26}$, Gd-$Gd_{.85}Er_{.15}$, and Gd-$Gd_{.74}Tb_{.26}$-$Gd_{.85}Er_{.15}$ AMR temperature span results. 72

Figure 5-14. Temperature spans of the pucks when used as individual AMRs and as part of the three layer regenerator. 72

Figure 5-15. Temperature spans of Gd-$Gd_{.85}Er_{.15}$ and Gd- $Gd_{.74}Tb_{.}26$-$Gd_{.85}Er_{.15}$ as a function of applied load. 73

Figure 5-16. Gd-Gd layered AMR temperature span vs T_H compared to predicted from single puck data 74

Figure 5-17. Layer temperature span vs T_{Hrel} for the Gd-Gd layered AMR. 75

Figure 5-18. Gd-$Gd_{.74}Tb_{.26}$ layered AMR temperature span data compared to that predicted from single puck data. 76

Figure 5-19. Gd-$Gd_{.85}Er_{.15}$ layered AMR temperature span vs T_H compared to predicted from single puck data..... 77

Figure 5-20. Temperature and specific heat profile for Gd-$Gd_{.74}Tb_{.26}$ with T_H = 304 K... 78

Figure 5-21. Cylinder top end picture and the 3-D model showing domains and boundary conditions. 80

Figure 5-22. Regenerator and rail temperatures as a function of time for $Gd_{.85}Er_{.15}$ with T_H at 290 K, helium pressure at 9.5 atm, and frequency at 0.65 Hz with different initial conditions. 83

Figure 5-23. Regenerator and rail temperatures as a function of time for $Gd_{.85}Er_{.15}$ with hot end precooling at 278 K for 1000 seconds. 84

List of Tables

Table 1-1. Variables in an AMR system. 6

Table 3-1. New field generator specifications. 25

Table 3-2. AMRTA specifications. 31

Table 3-3. Instrumented properties in the apparatus. 32

Table 4-1. Single layer regenerator experiments. 39

Table 4-2. Two layer regenerator experiments 46

Table 4-3. Three layer regenerator experiments. 55

Table 5-1. Heat flux versus bearing temperature. 81

Nomenclature

Acronyms

AMR(R)	Active Magnetic Regenerator (Refrigerator)
MCE	Magnetocaloric Effect (adiabatic temperature change)
MR	Magnetic Refrigerator
RTD	Resistive Temperature Device

Symbols

A	Cross sectional area/ Surface area
B	Magnetic flux density
C	Heat capacity
D	Diameter
E	Energy
H	Magnetic field intensity
h	Heat transfer coefficient
I	Current
k	Thermal conductivity
L	Inductance/ Length
M	Magnetization
m	Mass/ Mass magnetization
N	Number of atoms
N_{tu}	Number of transfer units
p	Pressure
Q	Energy flux/ heat transfer
r	Radius
Re	Reynold's number
S,s	Entropy, entropy per unit mass/ Entropy generation/ Stroke/
T	Temperature
t	Time
W	Work

Greek

Φ	Utilization
α	Porosity
β	Balance/ Isothermal compressibility
γ	Molecular field coefficient
φ	Fluid thermal capacity
μ	Viscosity/ magnetic permeability
ρ	Density
τ	Period

Subscripts

ref	Reference value
Curie	Curie point
C	Cold
H	Hot
x	Location
low	Low
high	High
B	Constant field/ Blow
ad	Adiabatic
b	Bed
f	Fluid
P	Pressure/ particle
s	Solid
g	Generation
min	Minimum
max	Maximum
M	Magnetic
rev	Reversible
irr	Irreversible
d	Demagnetizing/ Displacer
o	Outer
I	Inner

Acknowledgements

Much of the work in this thesis would not have been possible without the financial support of the Natural Sciences and Engineering Research Council of Canada as well as Natural Resources Canada. I would also like to thank my advisor, Andrew Rowe, for his support. His personality made this experience very enjoyable and instructive. Finally I would like to thank everyone in the group and department who provided valuable assistance by sharing their own expertise.

Chapter 1
Introduction

1.1 Motivation

Refrigeration is a pervasive technology that has been instrumental in transforming industrial societies throughout the world. Modern refrigeration equipment is reliable, inexpensive, and mature. It is not unrealistic to say there are few design variables that have not been thoroughly studied and optimized in near-room temperature devices. However, one of the difficulties with conventional vapour-compression refrigeration cycles is that most of the better refrigerants are ozone depleting substances consisting of chlorinated fluorocarbons (H/CFCs.) In contrast, magnetic refrigeration (MR) makes use of a magnetic solid as the refrigerant. As the refrigeration temperature decreases, magnetic refrigeration has the potential to offer significantly higher efficiencies than conventional gas cycles in more compact devices. Research into magnetic refrigeration is currently being pursued using low magnetic fields near room temperature in hopes of enabling commercial devices using permanent magnets as the field source. Another avenue of research is low-temperature applications. These devices could be used for cryogenic refrigeration and liquefaction of gases such as hydrogen and natural gas. In particular, current methods of hydrogen liquefaction are capital intensive and relatively inefficient. Magnetic refrigeration has the potential to provide compact and highly efficient devices over a broad range of operating temperatures. Opportunities for improved performance exist with further engineering refinements [1].

1.2 Magnetic Refrigeration

Background

Magnetic refrigeration exploits a property of magnetic materials called the magnetocaloric effect (MCE): the temperature of ferromagnetic materials is observed to rise upon application of a magnetic field. When a material is magnetized, its magnetic moments are aligned, leading to a reduction in its magnetic entropy. If this process is done adiabatically and reversibly the total entropy is constant. Thus, a reduction in magnetic entropy is compensated by an increase in lattice entropy resulting in a temperature increase. MCE can be defined as adiabatic temperature change due to

magnetization, or, alternatively, isothermal magnetic entropy change. This property is a strong function of magnetic field intensity and temperature, and is maximized at the magnetic material ordering temperature, known as the Curie temperature. Figure 1-1 shows Gadolinium MCE for a 2 T field. Interestingly, some antiferromagnetic materials cool down rather than warming up under magnetization [2].

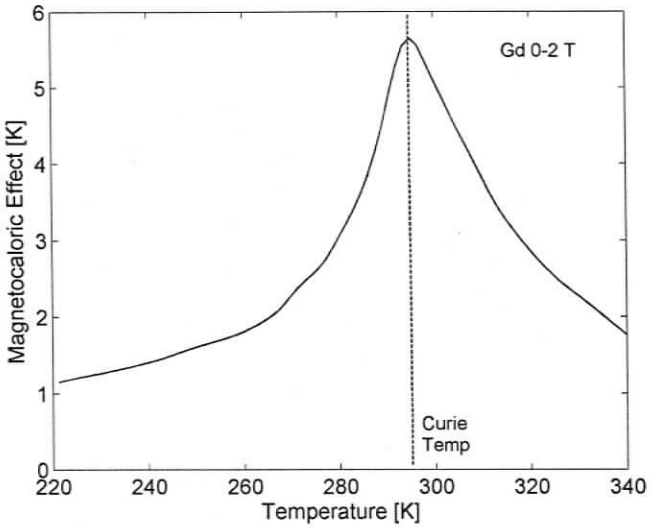

Figure 1-1. Magnetocaloric effect of Gd for a 0-2 T applied field change [1].

Subsequently one can think of using magnetic work to generate thermal cycles, just as compression work is used with gas-cycle refrigeration systems. For instance a Carnot cycle can be obtained by replacing the work of compression with isentropic magnetization. Magnetic refrigeration was first demonstrated for subkelvin cooling using a "batch cooling" method. The magnetic material, $Gd_2(SO4)_38H_2O$, magnetized at 1.5 K and 0.8 T, was adiabatically demagnetized, thus reducing its temperature to 0.25 K [2]. The batch cooling method is still used for reaching extremely low temperatures, however it cannot be considered a true refrigerator because it does not accomplish a continuous thermal cycle. A cyclic process is necessary for a practical refrigeration device.

Magnetic Refrigeration History

Until the 1970s, magnetic refrigeration remained a means of cooling for low temperatures only. For a material to have a significant magnetocaloric effect, the magnetic entropy change must be large relative to the total entropy of the material. At low temperatures, the lattice and electronic contributions to the entropy are relatively small. Thus, with moderate field changes, it was presumed that magnetic cooling was

only effective at low temperatures where the small magnetic entropy changes are relatively large compared to the total entropy [3].

In the 1970s, some exciting progress occurred in magnetic refrigeration. The first breakthrough came with the work of Brown [4][3]. He developed a magnetic refrigerator near room temperature using a reciprocating device based on the Ericsson cycle. Gd was used as refrigerant, a water-alcohol mixture as heat transfer fluid, and a water-cooled 7 T electromagnet. Research on a number of different devices, mostly with rotating and reciprocating geometries, quickly followed.

Then in 1982 a new concept was introduced by Barclay that became known as an Active Magnetic Regenerator (AMR). Unlike previous gas cycles, or magnetic cycles, the AMR concept coupled what had been two separate processes into a single component [3]. Instead of using a separate material as a regenerator to recuperate the heat from the magnetic material, the AMR concept made use of the refrigerant itself as the regenerator. In essence, a temperature gradient is established throughout the AMR and a fluid is used to transfer heat from the cold end to the hot. This subtle but important idea produced a new magnetic cycle distinct from Carnot, Ericsson, Brayton, or Stirling. In the AMR, each section of the regenerator bed undergoes its own cycle; the entire mass of working material no longer experiences a similar cycle at uniform temperature. This concept was given further complexity when the use of multiple magnetic refrigerants in a single AMR was introduced. Early AMR development was focused on the 77 to 20 K range to liquefy hydrogen [3].

During the past decade materials research has been prolific and there have been some interesting new alloys discovered that have the potential to be good magnetic refrigerants for room temperature applications. In particular, a series of ternary alloys in the $Gd_5(Si_xGe_{1-x})_4$ family was found to display high entropy changes due to a first-order phase transition. More recently, a transition metal based compound, $MnFeP_{0.45}As_{0.55}$, has been reported to have a large magnetic entropy change near room temperature again due to a first order phase change. As a result experimental devices have progressed to room temperature applications as time has passed. In 1990 the US Navy David Taylor Research Center in Maryland, conducted a test for room temperature refrigeration using a layered regenerator with a mixed composition of gadolinium and terbium [5]. The magnetic field intensity was varied between 0 and 7 T by ramping the current in the superconducting magnet up and down, in 70 second cycles. Temperature

spans up to 50 K were obtained, however the layering concept failed (larger temperature spans were achieved without terbium). While the Cryofuels group at the University of Victoria began working on a rotary AMR to liquefy natural gas, the Astronautics Corporation in cooperation with the Oak Ridge National Laboratory built and tested a medium scale magnetic refrigerator near the liquefaction temperature of nitrogen [6]. The design made use of two 2 kg regenerators reciprocating in a 7 T superconducting magnet. The device produced up to 25 W of cooling, and under no load and a heat rejection temperature of 82 K the cold end of the regenerator reached 44 K. Later, at the Ames Laboratory in Iowa, the Astronautics Corporation built and successfully tested a proof of concept reciprocating room temperature device capable of producing 500 W of cooling power and a coefficient of performance of 6 or more [7]. A helium-immersed superconducting magnet with a field up to 7 T was used. In 1998, researchers at Astronautics Corporation reported a room-temperature device using Gd refrigerant and a water-glycol heat transfer fluid. The cooling power of this device was high, but more significantly, they were able to show refrigeration with an applied field as low as 1.7 Tesla. In collaboration with the Ames Laboratory, this work is now being directed towards the development of a commercial refrigerator near room temperature using permanent magnets. In 2002 an Active Magnetic Test Apparatus was completed and tested by the Cryofuel Systems group at the University of Victoria. The design and construction was carried out by A. Rowe as part of his doctorate research [3]. The reciprocating device made use of a 2 T superconducting magnet and two AMRs with a mass of up to 135 g each. The refrigerator was designed for flexibility, with the main objective of characterizing a broad range of regenerators, for room temperature and cryogenic applications.

Active Magnetic Regenerator

For most contemporary materials, the MCE is modest even near the transition temperature: a material with an adiabatic temperature change larger than 2 K/T is unusual. For example, a sample of gadolinium near room temperature will exhibit a temperature change of approximately 10 K with the application of a 5 T magnetic field. Gadolinium is considered one of the best magnetocaloric materials. It is difficult to produce a useful temperature span based on a Carnot cycle when the effective isentropic temperature change is small. Given the above constraint, one can see the attraction of the active magnetic regenerator (AMR) cycle [1]. A passive regenerator is a highly effective recuperative heat exchanger working in conjunction with a single

pulsating fluid stream. If the passive, high heat capacity, material is replaced with an active magnetic material, an AMR is obtained. Acting as a regenerator as well as the means of work input, with the appropriate synchronization of a pulsating fluid and magnetic field, the AMR increases the temperature span many times the adiabatic temperature change as can be seen in Figure 1-2.

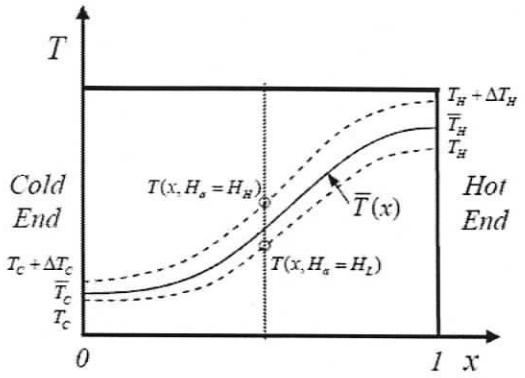

Figure 1-2. The AMR temperature profile at periodic steady state [1].

Like any refrigerator, an AMR operating at periodic steady-state produces a net flow of heat from a cold source to a hot sink. However, a unique feature of an AMR cycle is that at every section of the bed the refrigerant is undergoing its own unique local cycle. Although, the net heat transfer cycle occurs between reservoirs at $\overline{T}_C$ and $\overline{T}_H$, the bulk of the working material does not have to interact with these reservoirs directly. This is conceptually similar to a cascade system of a large number of magnetic refrigerators.

There has been a substantial amount of work regarding the development of materials that should make for good magnetic refrigerants. The assessment of the suitability of these materials has largely rested upon characterization of key thermodynamic properties such as magnetic entropy change, heat capacity, and adiabatic temperature change. It is becoming clear that these properties alone are insufficient in identifying materials that perform well in AMR cycles. Issues such as hysteresis, cost, purity, ease of regenerator manufacture, and relaxation rate all influence the design and performance of AMR coolers. Most importantly, there has been little information reported concerning the dynamic characterization of AMRs and demonstrating actual cooling powers and temperature spans. Systematic investigation of materials in AMR cycles is needed to aid in the development of this technology [8].

With the above in mind an Active Magnetic Regenerator Test Apparatus (AMRTA) has been designed and built with the objective of dynamically characterizing magnetic materials in AMR refrigeration (AMRR) cycles at room and cryogenic temperatures. The apparatus has the ability of monitoring and controlling a large number of variables on which the process depends.

1.2.1 Key Parameters

A large number of parameters affects the behavior and the performance of an AMR as illustrated in Table 1-1. These parameters can be categorized as geometric, magnetic, thermofluid, or operational. It is a challenging and lengthy task to experimentally test the system sensitivity for each variable. Furthermore numerical modeling has so far proven to support and predict results only marginally, largely due to the complexity and the non-linearity of the problem as well as uncertainties associated with the material properties.

Table 1-1. Variables in an AMR system.

Geometric	***Magnetic***	***Thermofluid/Operational***
Porosity	Field intensity	Heat transfer fluid
Regenerator shape	AMR material	Utilization, Φ
Regenerator aspect ratio	Field distribution	Frequency
Particle size	Flux shimming	Pressure
		Heat sink temperature
		Cooling
		Phasing

In this work, AMR porosity and shape, field intensity and distribution, heat transfer fluid type and phasing are fixed parameters, while the experimental focus is on understanding how heat rejection temperature, heat loads, utilization, frequency, magnetic material and AMR aspect ratio influence the performance of the system.

1.2.2 Temperature Profile and Cooling Power

Given an AMR and a set of parameters as defined in Table 1-1, the interest is to pinpoint the performance and to understand the physics underlying the phenomenon. Performance can be quantified by evaluating cooling power, temperature span between hot and cold end, and sensitivity to heat load. In addition, understanding AMR behavior

requires knowledge of its thermodynamic properties during operation which can be derived from the AMR temperature distribution. Thus, knowing the temperature distribution allows for the evaluation of cooling power, temperature span, heat load sensitivity, and thermo-magnetic properties of the system.

A practical experimental difficulty is measuring the temperature distribution throughout an AMR in operation. Only a few strategic points along the AMR bed are monitored in the AMRTA. Given the regenerator cylindrical geometry, adiabatic walls, and approximate uniform cross-sectional velocity profile of the fluid, the AMR can be approximated as a 1-D system, simplifying the task of mapping the temperature distribution, which can be condensed to a temperature (1-D) profile. It is expected that a 1-D approximation is most accurate for high aspect ratio regenerators. In a three layer regenerator the AMRTA can monitor the temperatures at the ends and the interfaces; therefore 4 points can be used to coarsely reconstruct the operating temperature profile.

1.2.3 Layering

A general scaling relationship giving the ideal MCE as a function of temperature is [3],

$$\Delta T^{\text{ideal}}(T) = \left(\Delta T_{\text{ref}} + T_{\text{ref}}\right)\left(\frac{T}{T_{\text{ref}}}\right)^{\beta} - T \tag{1.1}$$

where ΔT_{ref} is the MCE at a specified reference temperature, T_{ref}, and β is a parameter describing the capacity ratio of the fluid flux for the low and high field flows. For the basic AMR cycle, β is equal to one. In this case, the ideal MCE scales linearly with temperature as,

$$\Delta T^{ideal}(T) = \left(\frac{\Delta T_{ref}}{T_{ref}}\right) T \tag{1.2}$$

If the reference temperature is set to be the heat rejection temperature T_H, then ΔT_{ref} is the MCE of the refrigerant at T_H. Assuming the refrigerant is gadolinium and the reference temperature is equal to the Curie point, the ideal MCE can be plotted as shown in Figure 1-3. Clearly, as the temperature moves away from the Curie point of Gd, the real MCE is significantly less than ideal MCE. Thus, the temperature span produce by a real material is much less than can theoretically be supported operating with a heat rejection temperature (T_H) near the Curie temperature.

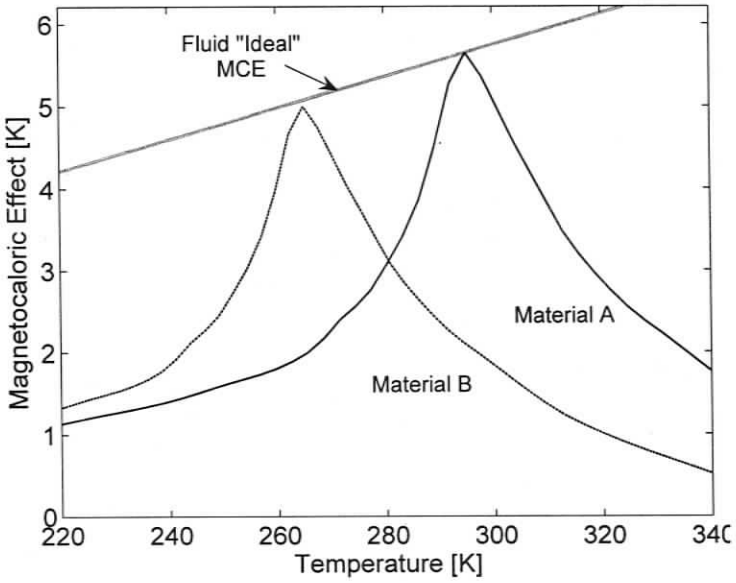

Figure 1-3. The ideal MCE as compared to gadolinium with a 0-2 T field change (Material A), and another material with a Curie temperature near 265 K (Material B).

To compensate for non-ideal material properties, the creation of a single AMR made up of more than one material has been proposed. By layering the AMR with magnetic refrigerants that have increasing Curie temperatures, it may be possible to more closely match the ideal MCE at different locations in the AMR. An example of concept is shown in Figure 1-3. However, a number of questions arise:

- How much of each material should be used per layer?
- What aspect ratio should each have?
- How many layers are required to maximize performance?
- Where does the AMR operate if an MCE peak exceeds the ideal scaling?
- How is the temperature profile affected?
- What is the performance sensitivity to heat load and T_H?
- How does utilization affect performance?
- How do initial conditions affect the steady state regime?

Addressing some of these issues for single and multi-material AMRs has been the objective of many numerical studies and a few experimental studies. The relatively slow progress in answering some of these questions and developing magnetic refrigerators with better performance can be attributed to the complexity of the problem on many different levels. Even the intuitive idea that a layered regenerator should outperform one composed of a single material has been a challenging task to validate.

1.3 Objectives

Magnetic refrigeration seems to be a promising technology for hydrogen and natural gas liquefaction, as well as room temperature refrigeration [1]. Compactness and efficiency are its key features. However, the complex nonlinear physics underlying the concept has frustrated experimental and numerical analysis for the past three decades [3]. Results have proven that the technology has potential, but understanding its principles and predicting its performance have been extremely difficult.

The objective of this work is to determine under what conditions layering of materials increases regenerator performance as compared to single material AMRs and to verify the impact of a number of variables on the performance of single and multi-material AMRs near room temperature. Experiments are conducted with AMRs consisting of Gd, $Gd_{.74}Tb_{.26}$, and $Gd_{.85}Er_{.15}$. The independent variables manipulated are gas pressure, frequency, cooling load, and heat rejection temperature, while the fixed parameters are magnetic field intensity (2 T), and regenerator particle size.

Chapter 2
Magnetic Refrigeration Theory

2.1 The Magnetocaloric Effect

Magnetic refrigeration exploits a property displayed by certain magnetic materials: the magnetocaloric effect (MCE). In these materials, a significant change in entropy can be effected by the application or removal of a magnetic field, H. For materials with a simple magnetic work mode, the MCE depends only on the absolute temperature of the material, T and the magnetic field change, ΔH (which expresses the difference H_f-H_i) [9]. The MCE can be interpreted as the isothermal entropy change or adiabatic temperature change as it is defined in the following expressions:

$$\Delta S_M(T,\Delta H) = S(T,H_f) - S(T,H_i) \qquad (2.1)$$

$$\Delta T_{ad}(T,\Delta H) = T(S,H_f) - T(S,H_i) \qquad (2.2)$$

Equations (2.1) and (2.2) are graphically illustrated in Figure 2-1(a), where the vertical

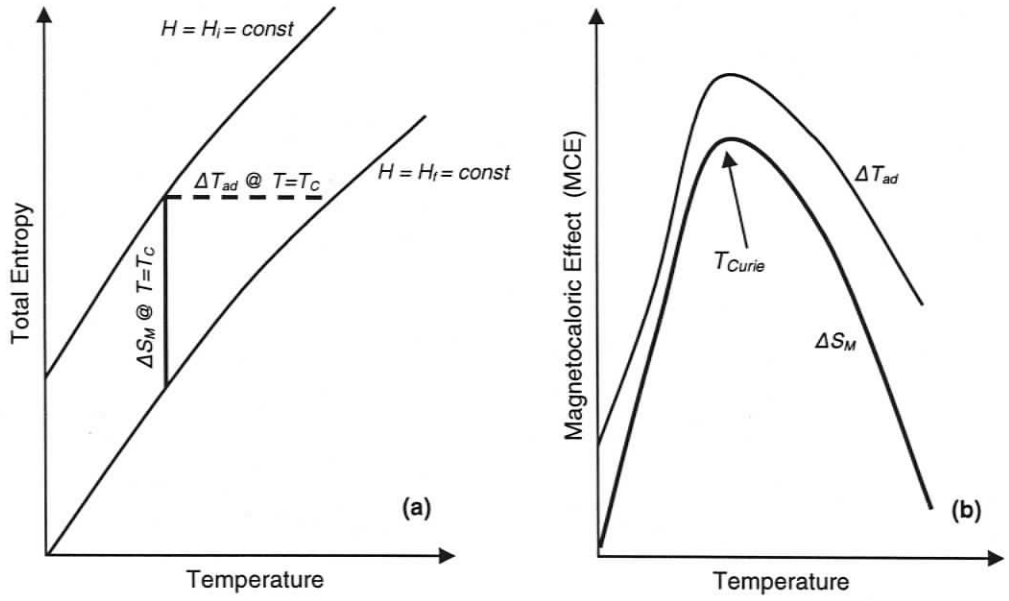

Figure 2-1. Graphical representation of the MCE [9].

line is the isothermal entropy change and the horizontal line is the isentropic (adiabatic)

temperature change. Both transformations occur between the same *S(T,H)* curves. Figure 2-1(b) illustrates ΔS_M and ΔT_{ad} for a range of temperatures in the proximity of the Curie temperature, T_{Curie} for $\Delta H = H_f - H_i$. In general, H_i is set to zero. Also a correlation between the MCE and magnetization can be derived. By varying the magnetic field, work is performed and the internal energy of the system changes. Thus, a differential variation in internal energy can be accomplished by a magnetic work interaction given by the product of the applied magnetic field, *H*, and the variation in magnetization, *m* [3]:

$$\delta w_m = \mu_0 H dm \tag{2.3}$$

Since for a material that has a simple magnetic work mode, $s = s(T,H)$, a differential change in entropy can be written as:

$$ds = \left(\frac{\partial s}{\partial T}\right)_H dT + \left(\frac{\partial s}{\partial H}\right)_T dH \tag{2.4}$$

where *s* is the entropy per unit mass. Using the definition of heat capacity, the above can be rewritten as,

$$ds(T,H) = \frac{c_B(T,H)}{T} dT + \left(\frac{\partial s}{\partial H}\right)_T dH. \tag{2.5}$$

If an isentropic field change is produced, the temperature change is:

$$dT = -\frac{T}{c_H(T,H)}\left(\frac{\partial s}{\partial H}\right)_T dH \tag{2.6}$$

and using Maxwell's relations for the equivalence of the second derivatives

$$dT = -\frac{T}{c_H(T,H)}\left(\frac{\partial m(T,H)}{\partial T}\right)_H dH \qquad (2.7)$$

From this simple explanation, one can deduce that a material with no significant work modes other than magnetic should have a high ratio of magnetic entropy change to total entropy to produce a large adiabatic temperature change. The MCE for a change in magnetic field from 0 to H is related to Equation (2.7) by

$$MCE = -\int_0^H \frac{T}{c_H(T,H)}\left(\frac{\partial m(T,H)}{\partial T}\right)_H dH \ . \qquad (2.8)$$

2.2 Materials

Although a broad range of materials that display a significant MCE for a wide spectrum of temperatures are available, research on the development of new materials is still more active than research on AMR cycles. A good refrigerant needs to feature a number of properties to perform satisfactorily in an AMR [4]:

a. An MCE as large as possible, over a broad temperature range allows large cooling power and temperature span, with low sensitivity to heat rejection temperature.

b. Minimal magnetic and thermal hysteresis allows high operating frequency and, consequently, large cooling power.

c. High specific heat improves power density.

d. High thermal conductivity improves regenerator effectiveness.

e. Large electrical resistance minimizes eddy currents.

f. Good mechanical properties simplify manufacturing process.

g. Low material cost is necessary for a commercial viability.

Currently, first order phase transition materials seem impractical for magnetic refrigeration even if they display a very large MCE. This may be due to hysteresis in the phase transformation and narrow MCE curves in the T_{Curie} vicinity. Gadolinium alloys are presently the prototype materials for room temperature magnetic refrigeration because of their good thermo-magnetic properties and since they are best characterized

materials [3] in terms of magnetization, heat capacity, and magnetocaloric effect. Thus, they are the choice for both experimental and numerical work that is being carried out. In particular, Gd, $Gd_{.74}Tb_{.26}$, and $Gd_{.85}Er_{.15}$ were used for room temperature refrigeration tests. Experiments were performed both using each material individually and in layered AMRs.

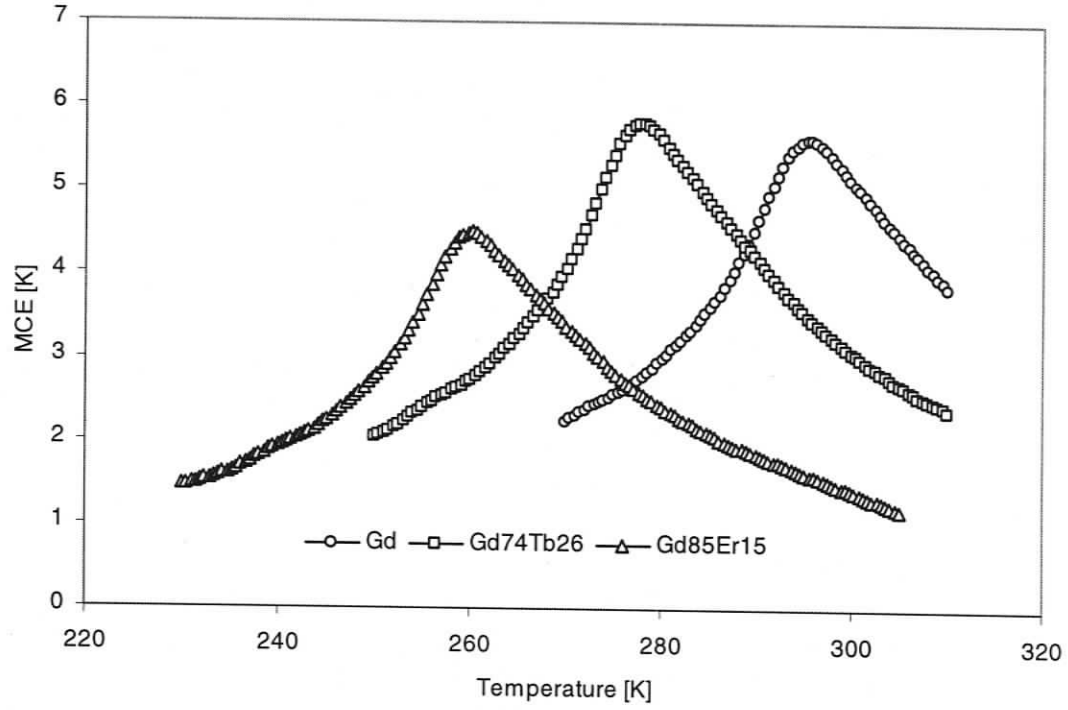

Figure 2-2. MCE as function of temperature for Gd, $Gd_{.74}Tb_{.26}$, and $G_{.85}Er_{.15}$ for 0-2 T.

Figure 2-2 illustrates the MCE for these materials as function of temperature when subject to a 2 T field in the vicinity of their para-ferromagnetic second order transition. The Curie temperature is ~294 K for Gd, ~278 K for $Gd_{.74}Tb_{.26}$, and ~260 K for $Gd_{.85}Er_{.15}$. Further, the MCE peaks are 5.6 K, 5.8 K, and 4.5 K, respectively. It is important to highlight the fact that the MCE can be significantly altered by impurities. The materials were chosen with T_{Curie} approximately 15 K apart with the objective of creating a broader MCE when testing as a layered regenerator. Figure 2-3 and Figure 2-4 show the specific heats of each material for 0 T and 2 T, respectively. For both cases all materials follow a similar pattern, with $Gd_{.74}Tb_{.26}$ displaying the largest value, while $Gd_{.85}Er_{.15}$ has the smallest peak specific heat. The $Gd_{.85}Er_{.15}$ specific heat curves suggest that the Curie temperature is at 265 K rather than 260 K. That is because MCE data was obtained by the Hydrogen Research Institute, at the Université du Québec à Trois-Rivières, while the

specific heat data was found by the Ames Laboratory, at Iowa State University. AMRTA experimental results suggest that 265 K should be used as Curie temperature.

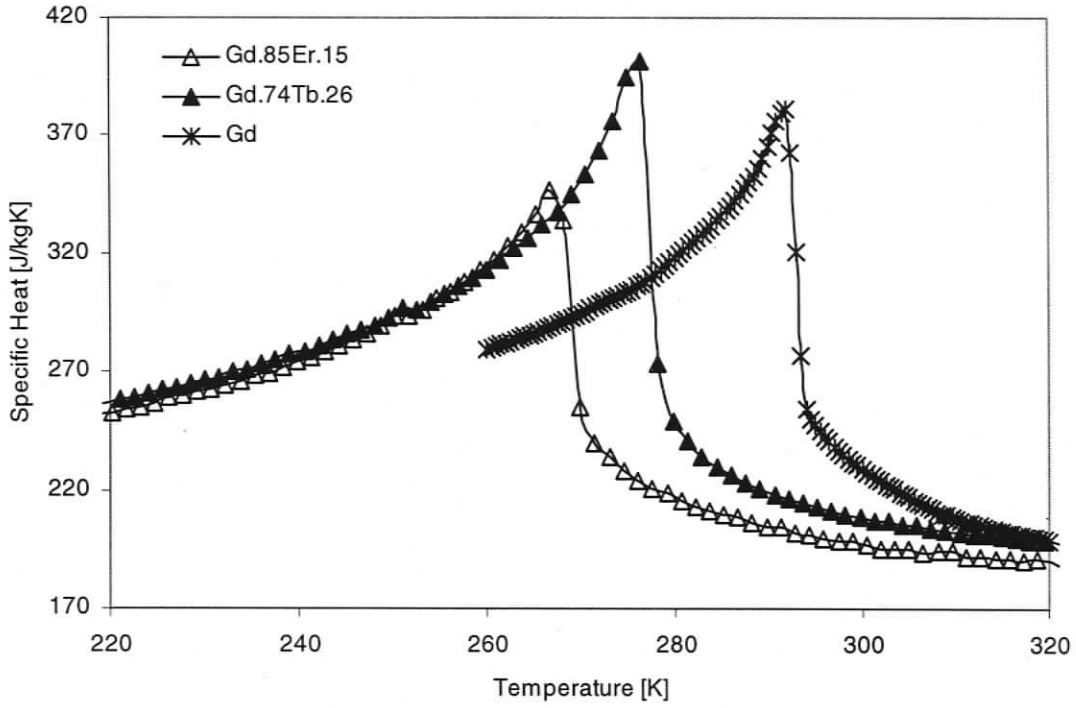

Figure 2-3. Specific heat vs temperature for Gd, $Gd_{.74}Tb_{.26}$, and $G_{.85}Er_{.15}$ at 0 T [11].

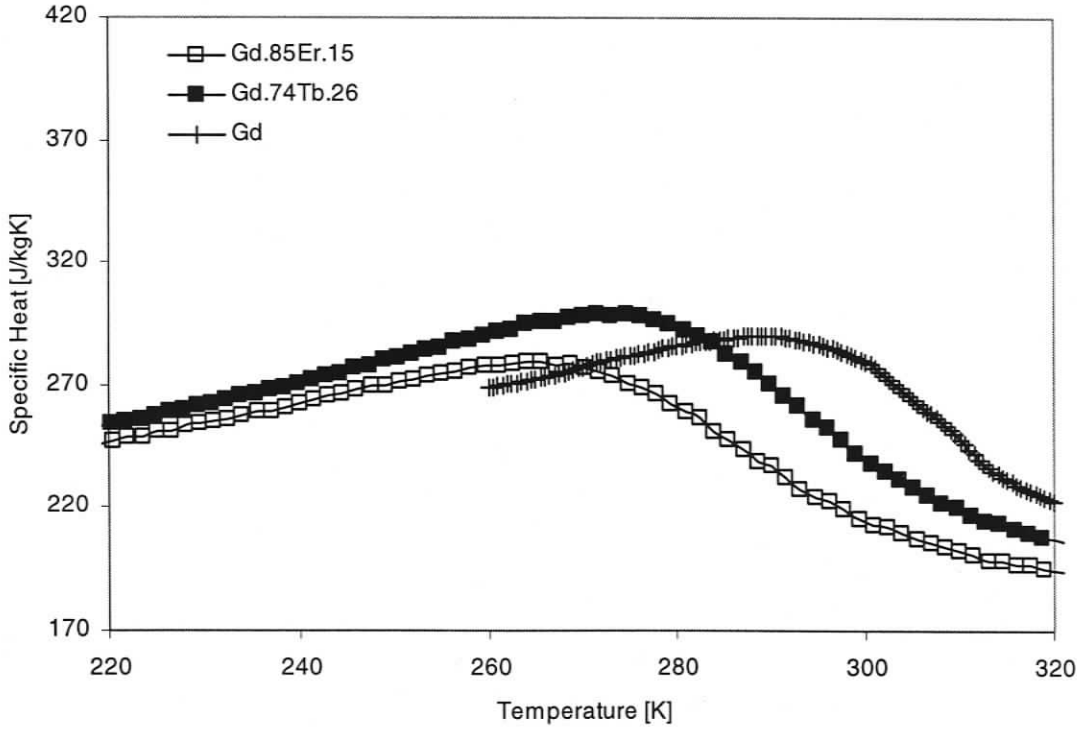

Figure 2-4. Specific heat vs temperature for Gd, $Gd_{.74}Tb_{.26}$, and $G_{.85}Er_{.15}$ at 2 T [11].

2.3 AMR Theory

The system under consideration is shown schematically in Figure 2-5. The envelope of an AMR bed is shown with a dashed line while a section of infinitesimal thickness is drawn with a solid line. The bed is made up of a porous solid material that is the magnetic refrigerant and a fluid within the pores acts as the heat transfer medium. The fluid transfers heat between a cold heat exchanger, the refrigerant, and a hot heat exchanger. The capacity rates of the fluid are shown as $\dot{\varphi}$ ($\dot{\varphi} = \dot{m}c_p$). Over a complete cycle, heat is absorbed at the cold end and rejected at the hot end. The AMR should be recognized as the combined solid-fluid system [3].

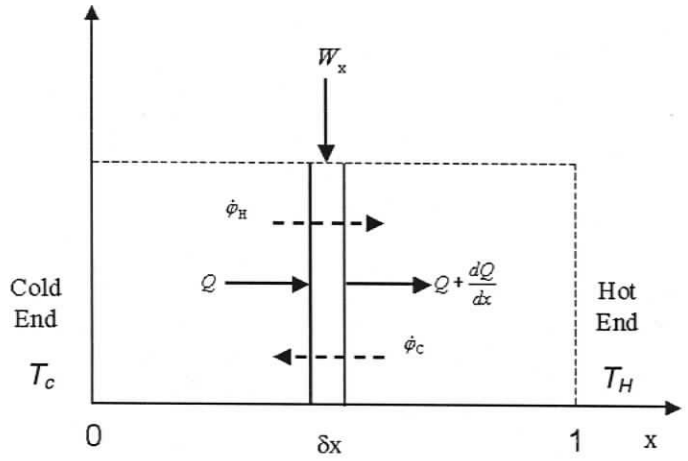

Figure 2-5. A schematic representation of an AMR showing the net work and heat flux at a differential section [3].

Most AMR devices built and tested to date have mimicked a reverse magnetic Brayton cycle in each section of the regenerator bed by using four distinct steps represented in Figure 2-6:

a. The bed is in a demagnetized state. Fluid flows through the regenerator entering the bed at a temperature T_H. As the fluid flows through the bed it exchanges heat with the solid refrigerant and exits the bed at T_C
b. The bed is exposed to a high magnetic field and the temperature of the refrigerant increases due to the magnetocaloric effect by $\Delta T(T)$
c. After absorbing a heat load and increasing its temperature by ΔT_C, the fluid enters the cold end of the regenerator, absorbs heat from the solid and exits the AMR at a temperature $T+\Delta T_H$

d. The AMR is demagnetized, the temperature decreases due to the magnetocaloric effect, and the cycle repeats

Figure 2-6 shows the assumed refrigerant cycle occurring in the differential section at some location in the AMR. The cycle as described above is equivalent to the process starting at point '*a*' and proceeding alphabetically to return to the starting point.

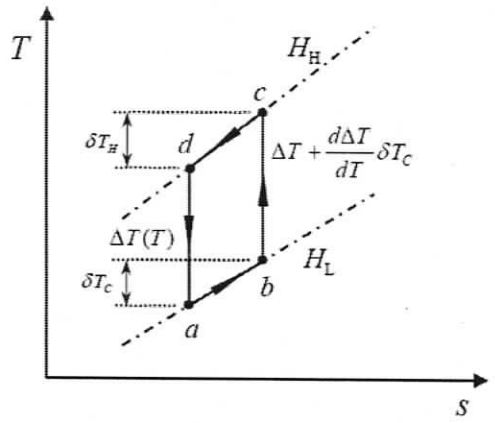

Figure 2-6. Hypothetical cycle for the magnetic refrigerant at some cross-section of the AMR [3].

It is assumed that the magnitude of the MCE for the process b-c is described by a first order Taylor series approximation in reference to point a. In the reversible case, the resulting area within the T-s diagram is equivalent to the magnetic work input per unit mass for a complete cycle.

If the details of the AMR are ignored and one focuses on the absorption of heat by the fluid flowing through the cold reservoir, the cooling power can be determined from,

$$\dot{Q}_c = \oint \dot{m}_f(t) c_p T_f(t) dt \qquad (2.9)$$

where $\dot{m}_f(t)$ is the fluid mass flow rate as a function of time, c_p is the fluid heat capacity, and T_f is the fluid temperature at the exit of the AMR. For a complete cycle the integral can be written as,

$$\dot{Q}_c = \left(m_f c_p\right) \Delta T_f \qquad (2.10)$$

where ΔT_f is the effective temperature change of the fluid as it flows through the cold heat exchanger, and m_f is the mass of fluid that flows through the AMR when it is demagnetized. If the regenerator has a very high number of thermal transfer units (NTU), the temperature of the fluid exiting the AMR will closely match the temperature of the solid refrigerant at the cold end. In addition, if the thermal mass of the refrigerant is much greater than the thermal capacity of the total fluid flux through the regenerator, the temperature of the solid will not change much. The ratio of the fluid thermal capacity to the regenerator thermal mass is called the utilization and is defined as,

$$\Phi = \frac{m_f c_p}{M c_B} \tag{2.11}$$

where M is the mass of refrigerant in the regenerator and C_B is the average heat capacity of the refrigerant. In the limit of very small utilization and large NTU, and assuming parasitic heat leaks are insignificant, the temperature change of the fluid as it absorbs heat through the cold heat exchanger is equal to the magnetocaloric effect of the refrigerant at the cold end of the regenerator, $\Delta T_f = \Delta T_C$. In terms of passive regenerators, Φ is sometimes referred to as the matrix capacity rate ratio and varies little throughout the regenerator for constant fluid heat capacity. For an AMR, the local utilization is a function of field and temperature and, in general, is position dependent.

If the AMR cycle is a reversible process, no entropy is generated in the regenerator, and therefore the same amount of entropy flows in and out. In addition, if the regenerator is assumed to behave as a cascade system of an infinite number of magnetic refrigerators the following relation is true throughout the regenerator length [12]:

$$\dot{S}(x) = \frac{\dot{Q}(x)}{T(x)} = const \tag{2.12}$$

where $\dot{S}$ and $\dot{Q}$ are the entropy and heat flow rate and T is the absolute temperature, all at the same axial location x. Furthermore, the boundary conditions at the hot and cold end are:

$$\dot{Q}_c = \dot{m}_f C_P \Delta T_{ad_c} \tag{2.13}$$

$$\dot{Q}_h = \dot{m}_f C_P \Delta T_{ad_h} \tag{2.14}$$

Thus, substituting (2.13) and (2.14) into (2.12) we obtain

$$\frac{\Delta T_{ad_c}}{T_c} = \frac{\Delta T_{ad_h}}{T_h} \tag{2.15}$$

Lastly, if we consider the temperature of the hot end the reference temperature, the above expression suggests that the magnetocaloric effect must scale with temperature according to the following relation:

$$\Delta T_{ad}^{ideal}(T) = T \frac{\Delta T_{ref}}{T_{ref}} \tag{2.16}$$

where ΔT_{ad}^{ideal} is the ideal MCE at temperature T, ΔT_{ref} is the MCE at the hot end of the AMR, and T_{ref} is the temperature of the AMR at the hot end in the low magnetic field. Equation (2.16) states the ideal magnetocaloric effect should be a linearly increasing function of temperature. If correct, this expression implies that if the magnetocaloric effect at the cold end of the AMR exceeds that at the hot end, the second law of thermodynamics will be defied [3]. This constraint has led researchers to search for magnetic refrigerants that match this linear expression for MCE.

It has been argued that even though comparing an AMR to a cascade of refrigerators helps in understanding the AMR cycle, the analogy does not strictly apply [12]. More specifically, the interactions among the infinitesimal AMR layers are complex, nonlinear and marginally understood. As a consequence the validity of Equation (2.16) is questionable, and it can only be used as a guideline.

Because the adiabatic temperature change is temperature dependant, the MCE is a function of position in a regenerator. Consequently in order to predict the adiabatic temperature change at a specific location x, it is necessary to know the temperature at this location. For passive regenerators the temperature profile is nearly linear, with a small deviation at the ends [12]. The same cannot be assumed for AMRs, especially if a high utilization factor is used. As will be discussed in Chapter 4 and 5, experiments have shown that the temperature profile within the AMR can be very close to linear or highly non-linear depending on the operating conditions.

Current multi-material AMR data also shows that the temperature profile can significantly deviate from linear depending on operating heat rejection temperature, underlying the complexity of the interaction of the temperature profile with the local MCE. Such interdependency suggests another possible issue with multi-material regenerators: initial condition sensitivity. Assuming that an AMR starts operating with a uniform temperature of $T = T_H$, it will eventually reach a pseudo steady state temperature distribution. At the beginning of the process, cooling is almost entirely performed by the hot end layer, which is already within its MCE operating temperature range (assuming that the materials have significantly different Curie temperatures). As a temperature gradient starts to develop, the other layers begin contributing to the overall refrigeration process, until a steady state temperature profile is established. The larger the final temperature span, the further away the cold end is from its MCE operating range at the beginning of the process. Thus, it is possible that when starting from a temperature profile $T(x) = T_H$, there is not enough cooling power to drive the AMR to the expected operating regime. It could then be necessary to pre-cool the cold end to "prime" the regenerator. In this case the AMR could have two or more operating regimes depending on the initial conditions.

Governing equations for an AMR system have been developed throughout the years with the objective of analytically or numerically describe its thermo-magnetic state at a specific time and for a given set of boundary conditions. They consist of a system of two equations, one for the fluid and the other for the solid matrix. These equations are derived from the energy balance expressions for each phase. Since they are coupled, they must be solved simultaneously.

The energy balance for a heat transfer fluid flowing through a regenerator can be summarized by the following [13]:

$$\rho_f C_p A_f \frac{\partial T_f}{\partial t} = -\dot{m}_f C_p \frac{\partial T_f}{\partial x} + \frac{\partial}{\partial x}\left(k_f A_f \frac{\partial T_f}{\partial x} \right) + hP_w \left(T_s - T_f \right) + \left| \frac{\partial p}{\partial x} \frac{\dot{m}}{\rho_f} \right| \qquad (2.17)$$

where ρ_f is the density, A_f is the area of fluid flow, k_f is the thermal conductivity, h is the convection heat transfer coefficient, P_w is the wetted perimeter, or cross-sectional contact area between the fluid and the regenerator matrix, and p is the fluid pressure. All parameters with the subscript f refer to the fluid. The viscous losses are a function of the pressure drop $\frac{\partial p}{\partial x}$, which strongly depends on the operating frequency and system pressure. Pressure drop sets a major limitation on AMR efficiency, thus, much work is focused on its minimization through the choice of heat transfer fluid, regenerator matrix microscale structure, and AMR aspect ratio.

Similarly the energy balance for the solid matrix can be expressed as it follows [13]:

$$\rho_S A_S \left(\frac{\partial u_S}{\partial t} - B \frac{\partial m}{\partial t} \right) = \frac{\partial}{\partial x}\left(k_S A_S \frac{\partial T_S}{\partial x} \right) + hP_W \left(T_f - T_S \right) \qquad (2.18)$$

where the magnetic work term has been grouped on the left side of the expression with the internal energy term. Both the fluid and matrix expressions assume uniform properties in the radial direction and adiabatic cylindrical walls. In Equation (2.18) the dissipation terms are not present, however there is an additional magnetic work term. The Equation (2.17) can be expressed as:

$$k \frac{\partial T_f}{\partial \dot{t}} = -\Phi \frac{\partial T_f}{\partial \dot{x}} + \frac{\partial}{\partial \dot{x}}\left(\frac{\varphi}{Pe_f} \frac{\partial T_s}{\partial \dot{x}} \right) + NTU\Phi \left(T_s - T_f \right) \qquad (2.19)$$

where the following non-dimensional parameters have been introduced:

$$\Phi = \frac{\dot{m}_f c_p \tau}{M_s c_B} \qquad (2.20)$$

$$NTU = \frac{hA_w}{\dot{m}_f c_p} \tag{2.21}$$

$$k = \frac{M_f c_p}{M_s c_B} \tag{2.22}$$

$$Pe_f = \frac{\dot{m} c_f L}{k_{eff} A_f} \tag{2.23}$$

$$t^* = \frac{t}{\tau}; \quad x^* = \frac{x}{L} \tag{2.24}$$

where A_w is the wetted area, M_f the mass of the gas within the regenerator, L length of the regenerator, and k_{eff} is the conductivity of the regenerator and fluid, taking into account dispersion effects.

Chapter 3
Apparatus Overview

3.1 Design Challenges

AMRR design types can be grouped into either reciprocating, rotary, or pulsed field. Each solution has its advantages and disadvantages over the others. Some of the difficulties associated with the design and construction of an AMRR include [3]:

a. Large magnetic forces

b. Operating frequency

c. Sealing

d. Regenerator design

e. Alternating field

f. Magnetic material volume

The AMRTA is a reciprocating device. This design has been chosen for its simplicity, accessibility, and reliability. However it implies large inertial forces, limiting both the operating frequency, and the mechanical efficiency. A rotary device is a more likely candidate for commercial applications, since it allows for high operating frequencies, low mechanical forces, and compact magnets. Nevertheless, a number of technical issues, such as sealing, need to be addressed to make this approach practical.

3.2 The AMRTA

The Active Magnetic Regenerator Test Apparatus has been designed with a specific objective: flexibility for testing and collecting data using a large variety of AMR beds in a broad range of working conditions. Therefore, the AMRTA is strictly an experimental apparatus and would not be a feasible approach for a commercial system. Instead the AMRTA is capable of producing a broad range of scenarios, which, combined with a sound, instrumented data acquisition system, is progressively disclosing complex magnetic and thermodynamic interactions. The following sections of this chapter describe the AMRTA's design, technical specifications, instrumentation, and upgrade history.

3.2.1 Apparatus Design

The apparatus consists of two subsystems, entirely independent from each other: the Field Generator, a 2 Tesla superconducting magnet, and the AMR sub-system.

Field Generator

The field generator consists of an 84 cm x 54 cm high cylindrical chamber designed around NbTi superconductor solenoid conduction-cooled by a single two-stage Gifford-McMahon cryocooler with 1 W of cooling power at 4.2 K. The design operating current is 362 Amps for a 5 T field. Conventional (copper) current leads optimized for minimum heat leak with a current of 250 Amps connect the room-temperature feedthroughs to the warm end of High Temperature Superconducting leads (HTSC). The electrical connections to the magnet are completed using two HTSC leads rated at 500 Amps purchased from American Superconductor. The magnet is thermally linked to the second stage of the cryocooler via flexible connectors which are manufactured using flexible 0.4 mm thick OFHC copper foil. The cryostat is a 304 SS vacuum chamber known as the cold box. Insulating blankets made with multi-layers of aluminized mylar surround the magnet inside the copper radiation shield as well as outside the shield [3].

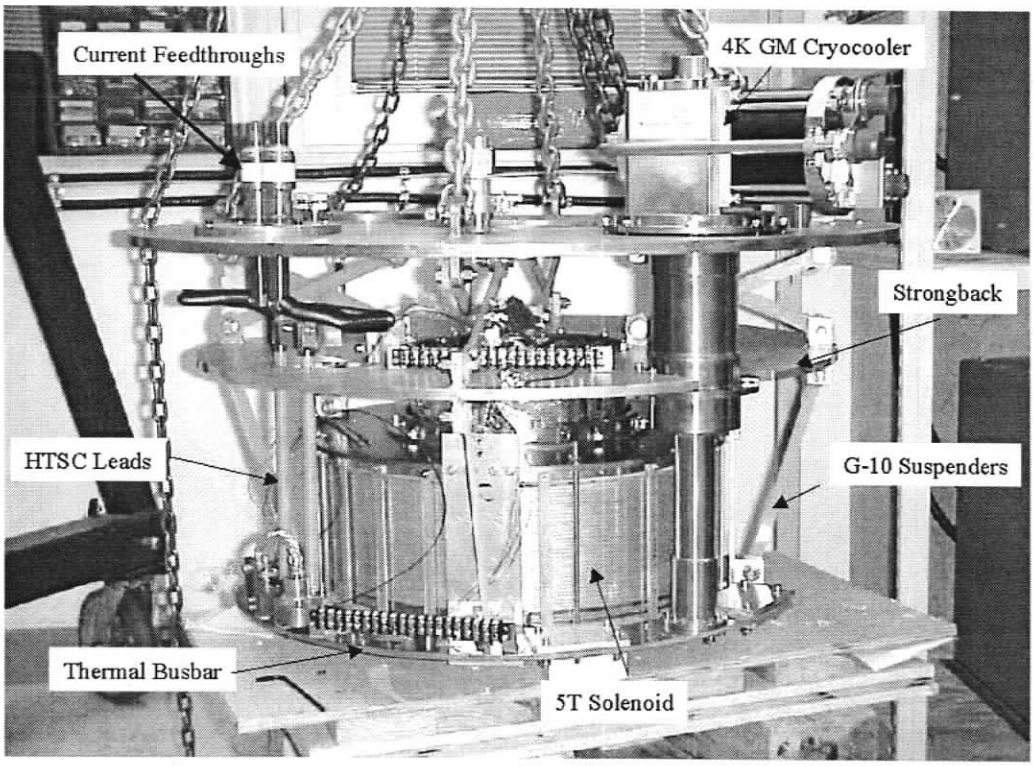

Figure 3-1. Magnet internal assembly (coldbox not shown) [3].

Even though the magnet is rated for a 5 T field, its operating current is limited due to overheating by joule effect between the copper leads and the HTSC leads. The temperature rise at the joint eventually causes the HTSC leads to quench (turn from superconducting into conducting) and the power supply to shutdown. Therefore the magnet has been operated only at 145 A and 2 T. Recently the thermal contact with the cryocooler first stage, which is a 30 K heat sink, has been improved and therefore is believed that the coil can be operated at higher current. However it has not yet been tested at a higher field because of time constraints.

The magnet generates a field where the magnitude decreases quickly from its maximum value at $z = 0$ and $r = 0$, where z is the vertical axis of symmetry and r the radial distance from z. For instance, for the coordinates $z = 25$ cm and $r = 0$, the field intensity is less than 20% of its peak. Figure 3-2 illustrates the normalized field profile along the z axis. Because of the coil geometry the field features cylindrical symmetry. The cylinder carrying the regenerators reciprocates with a stroke of 50 cm, therefore in the low field condition the regenerator senses 5% of the full field.

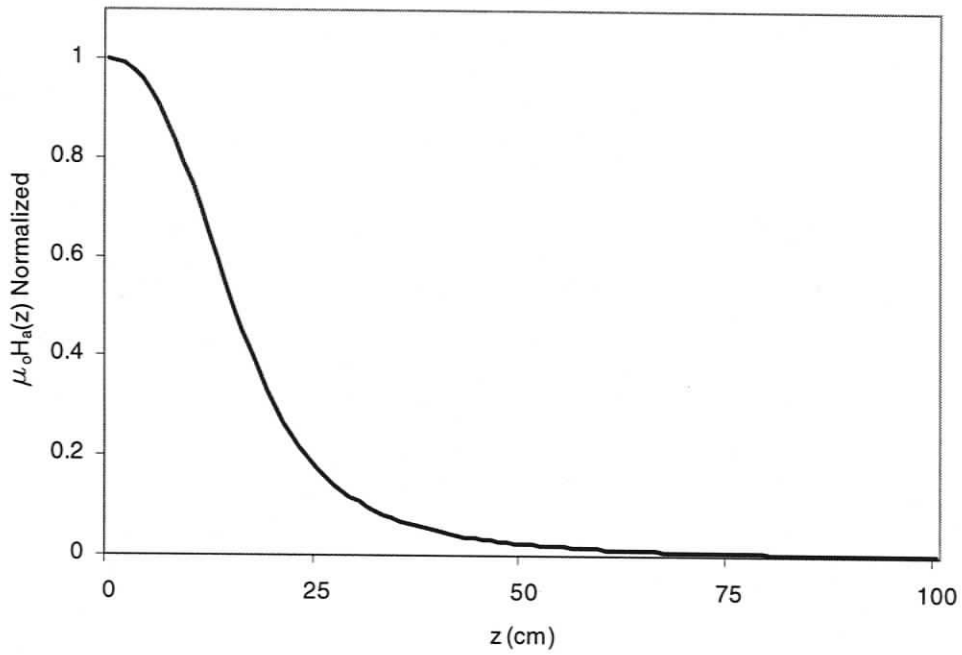

Figure 3-2. $\mu_0 H_a(z)$ normalized distribution along Z axis.

The apparatus is currently being upgraded with a new superconducting magnet manufactured by Cryomagnetics. The new field generator will allow the apparatus to operate at 5 T. It consists of a 61 cm x 61 cm high cylindrical aluminum chamber with a

21.1 cm bore. The NbTi spool is installed on the bottom of the aluminum/composite cryostat and the magnetic center is 16.5 cm from the base of the chamber. Conduction cooling is achieved utilizing a CryoMech Model PT 405 cryocooler which consists of a two stage pulse tube cold head and a water cooled compressor. The second stage is rated at 0.5 W at 4.2 K. The design operating current is 56 Amps for a 5 T field. Table 3-1 illustrates the technical specifications. It is designed to match the field distribution of its predecessor.

Table 3-1. New field generator specifications.

Hmax/H(0,0)	1.43
Current at 5T	56A
Sensitivity	884.6 gauss/A
I/Ic (B(0,0)=5T, 4.2K)	0.5
Inductance	105 H
Superconductor	Nb-Ti

AMR Sub-system

The AMR sub-system is a component designed to be independent of the magnet. The combination of the magnet and the AMR sub-systems comprises the AMR Test Apparatus (AMRTA). A cylinder carrying two AMR beds reciprocates in and out of the high field region. The cylinder carries two heat exchangers on either end that act as the hot heat sinks. Cooling fluid is delivered to the heat exchangers by flex hoses. Helium is used as the heat transfer fluid in the AMR with a maximum pressure of 10 atm. The gas oscillates with a nearly sinusoildal waveform through the cylinder by a gas displacer mechanically coupled to the cylinder drive shaft. Figure 3-3 illustrates phasing among field, transfer fluid flow, and cylinder linear velocity [3] for a 0.65 Hz operating frequency, 9.5 atm system pressure, and 2 T field intensity.

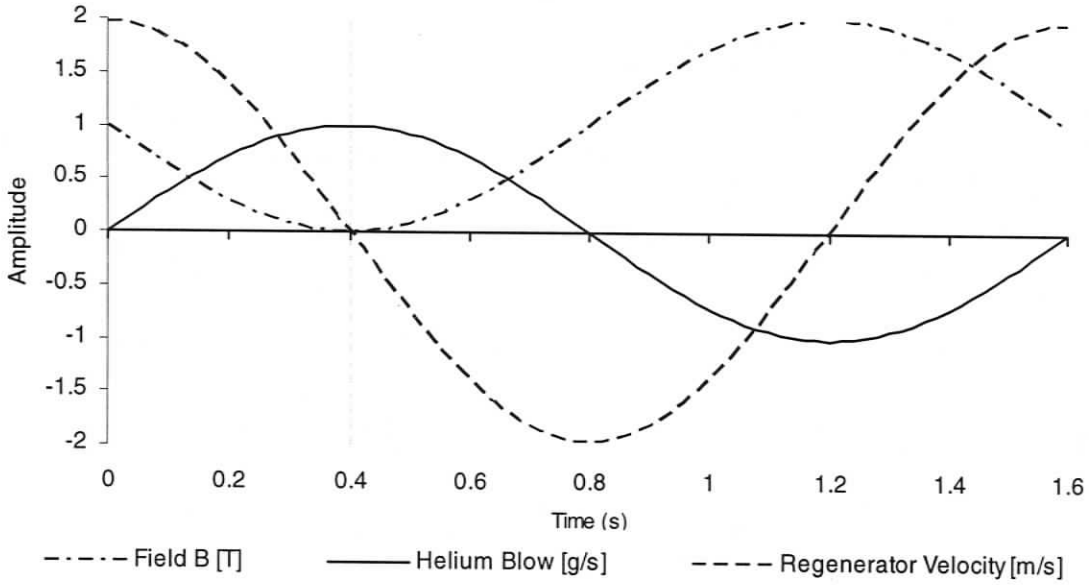

Figure 3-3. Phasing among field, transfer fluid flow, and regenerator linear velocity.

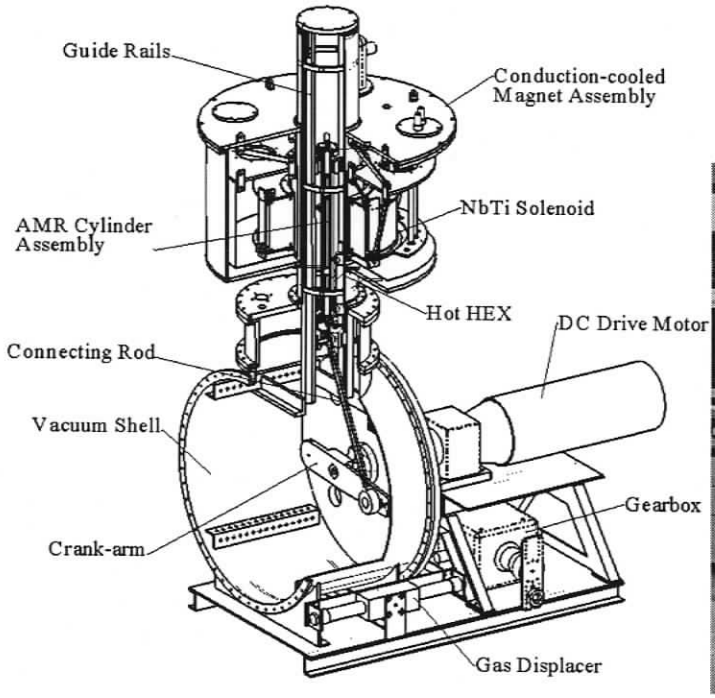

Figure 3-4. AMRTA layout.

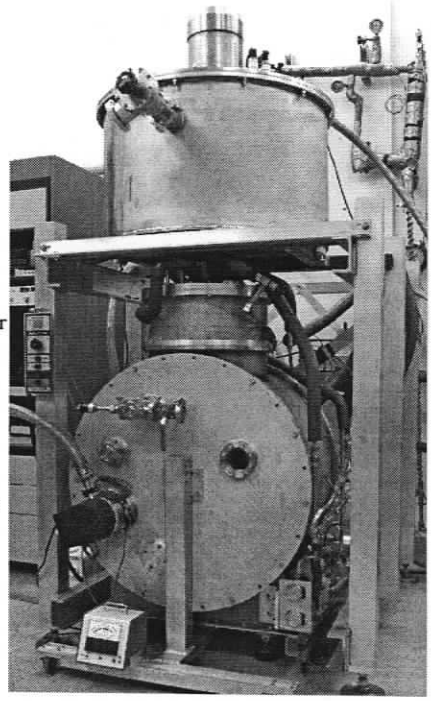

Figure 3-5. AMRTA assembly.

Figure 3-4 shows the conceptual layout with most of the key components. Figure 3-5 shows more of the assembly details including a stand needed to support the superconducting magnet in position above the AMR system. The vacuum housing

consists of a stainless steel shell, which operates as crank housing and cylinder bore (vacuum tube) structural support. The vacuum tube is capped and sealed with an aluminum ring containing o-rings and a separate blank flange. The housing is mounted on a wheeled aluminum base plate also used to mount the drive system. To minimize the convective heat leak during low temperature testing, the shell is evacuated to a vacuum of 10^{-5} torr (~10^{-8} atm) or better [3]. Flexhoses attach to feedthroughs on the vacuum vessel and to fittings on the cylinder. A DC motor drives the entire apparatus with operating frequencies between 0.2 and 1.2 Hz. Two electrical heaters in between the AMR beds act as a heat load. A schematic of the apparatus is shown in Figure 3-6.

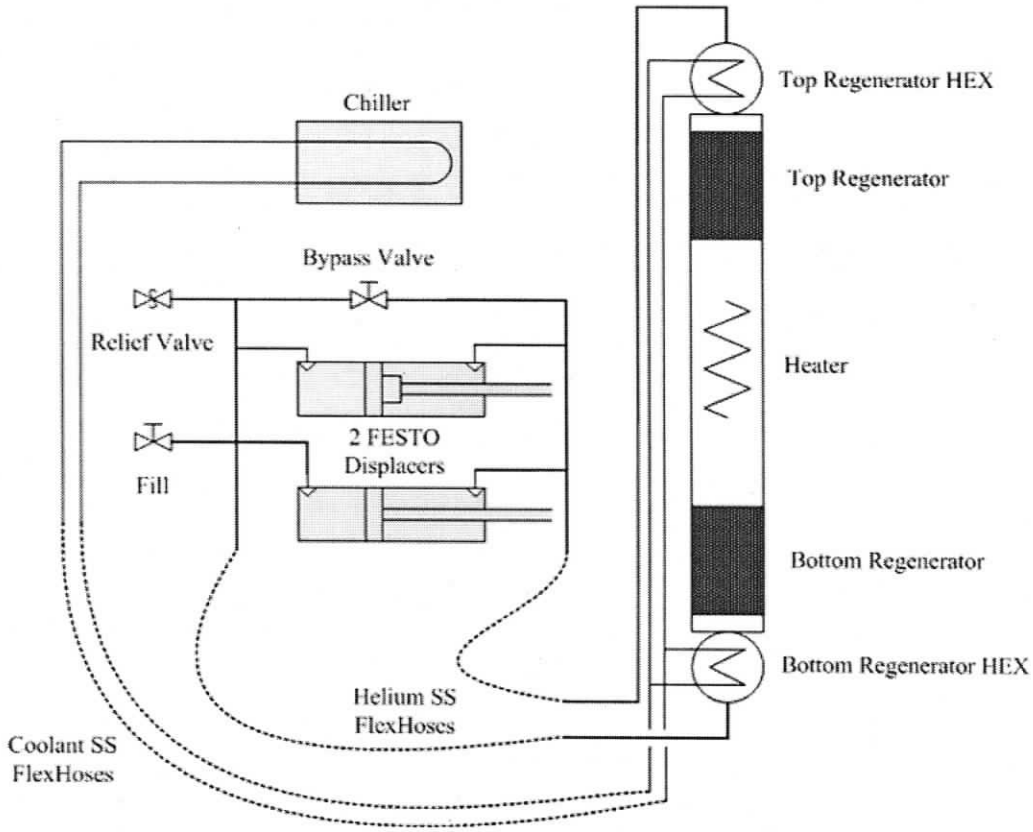

Figure 3-6. Schematic of the gas transfer and cooling fluid system for the AMR Test Apparatus.

The fluid transfer system encompasses the components that contain and control the movement of fluid through the regenerators. Each end of the cylinder carries a shell and tube heat exchanger rated for cryogenic service. On the tube side, helium gas rejects heat to a cooling fluid. A series of tubes connect the heat exchangers to flex hoses at the base of the cylinder and these hoses connect to feedthroughs on the top of the vacuum shell and then to the external coolant source.

The heat transfer fluid is forced to oscillate through the regenerator beds by using two reciprocating, hermetically-sealed, rodless cylinders manufactured by Festo. A diagram of the displacer is shown in Figure 3-7. The displacer is forced to reciprocate about its center position by coupling to the drive motor through a gearbox. Since it is mechanically coupled, the phasing between the blow waveform and the regenerator position is fixed; however, it can be adjusted by changing the angular position of the displacer crank-arm. The stroke length of the gas displacer can also be set by varying the throw length on the crank. Finally, another degree of freedom is the gas pressure. The displacer is rated to 8 atm nominal with a maximum of about 10 atm. In addition some of the coolant is diverted from the main stream through the cylinder and is used to cool the rail, and regulated through a valve. This setup allows for precooling before and cooling during an experiment. Rail and bearing temperature are read by Platinum Resistance Thermometers (PRT), so that heat leaks can be monitored and when necessary regulated through the cooling system.

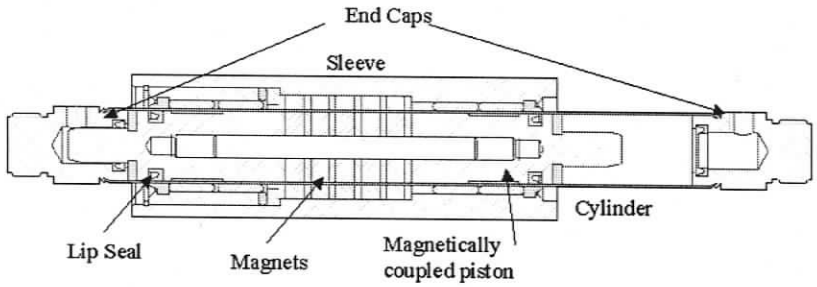

Figure 3-7. Internal cross-section of the Festo fluid displacer.

For room temperature experiments a Neslab ESC-150 recirculating chiller is used to control the heat rejection temperature. Its temperature range is +40 °C to -20 °C with +/- 1.0 °C temperature variance at steady state operation. The chiller cooling capacity is 4 kW at +20 °C and 1.5 kW at -10 °C. Currently a water-glycol (50%-50%) mixture is used as the coolant fluid.

The cylinder assembly is the heart of the apparatus. This component carries the regenerators and is oscillated in and out of the high field region of the magnet. Unlike other reciprocating AMRs, the hot heat exchangers are carried on the cylinder in order to minimize the dead volume between the heat sink and the AMR beds. Heat loads are simulated with an electric heater controlled by a voltage source. The cylinder is non-metallic in order to limit thermal conduction and eddy-current heat generation. Further it

is strong enough to withstand the magnetic forces on the regenerators, and gas tight to contain helium at pressures up to 10 atm. A 1-¼ inch (31.8 mm) inner diameter G-10 tube with 1/8 inch (3.2 mm) thick wall makes up the cylinder housing. A wire harness connects to a feedthrough on the vacuum chamber and transmits PRT signals, heater current, and sensor excitation to the cylinder. Stainless steel flex hoses attach the cylinder lines to feedthroughs on the vacuum shell. Figure 3-8 depicts the complete cylinder assembly while Figure 3-9 shows the internal arrangement. The cylinder rides on as many as six bearings on rails inside the vacuum bore. Commercial self-aligning contact bearings made of a Teflon impregnated material called Frelon are used [3].

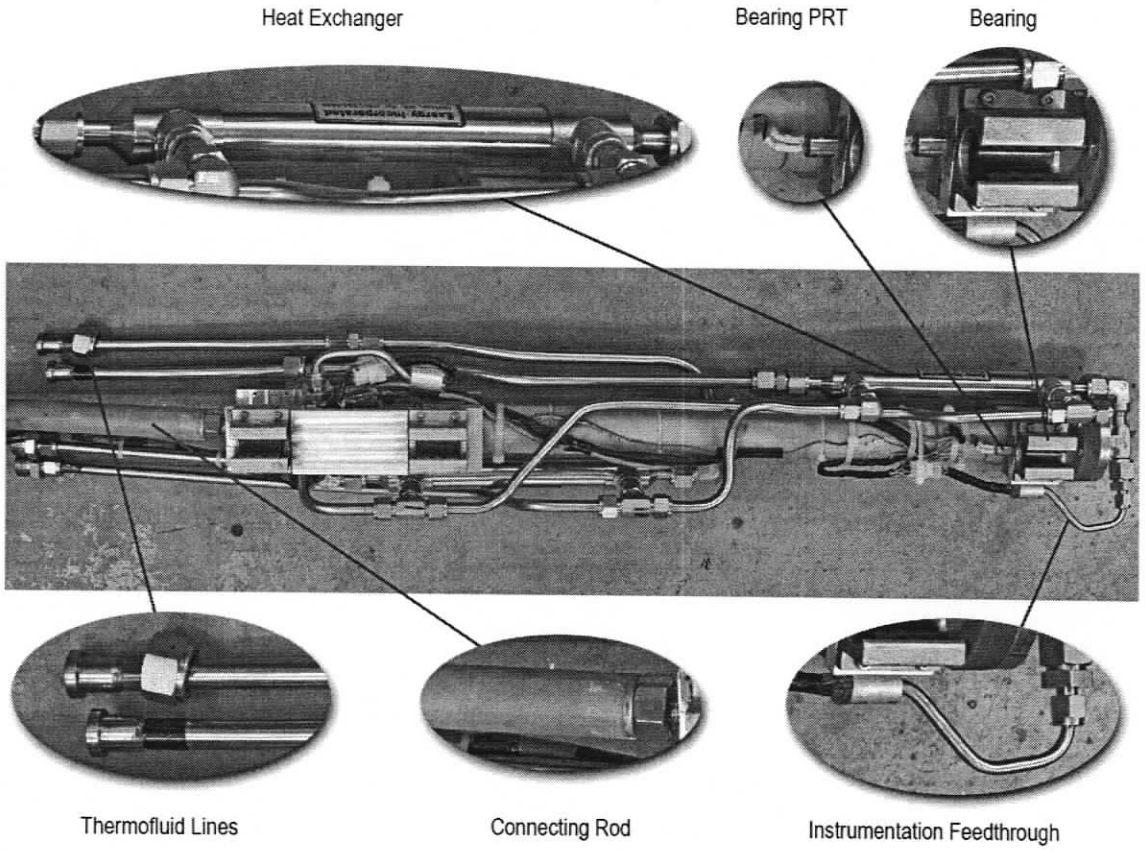

Figure 3-8. Cylinder assembly.

The nominal stroke of the cylinder is 0.5 m (total movement of cylinder) based upon the field shape produced by the magnet subsystem and the need to ensure that the low field is as small as possible. From the maximum field position the cylinder moves up 0.25 m and down 0.25 m in order to move each bed from the high field region to a low field region. The cylinder cross section depicted in Figure 3-9 shows the phenolic insert

in the central portion of the cylinder, which has the purpose of reducing void space between the regenerators.

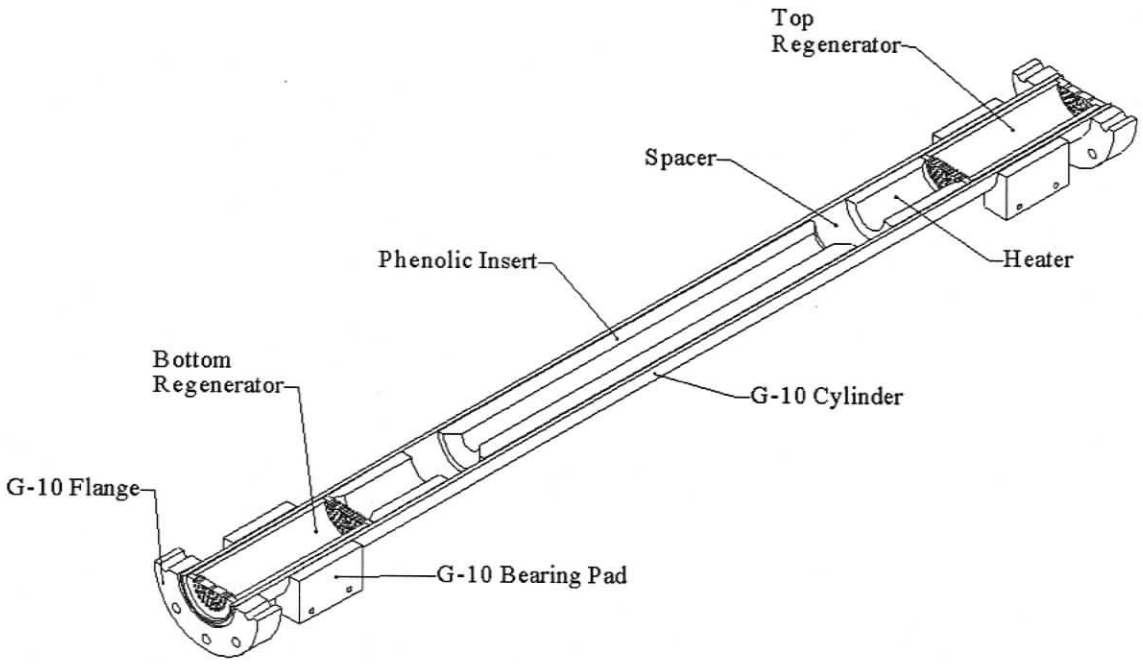

Figure 3-9. Cylinder internal layout.

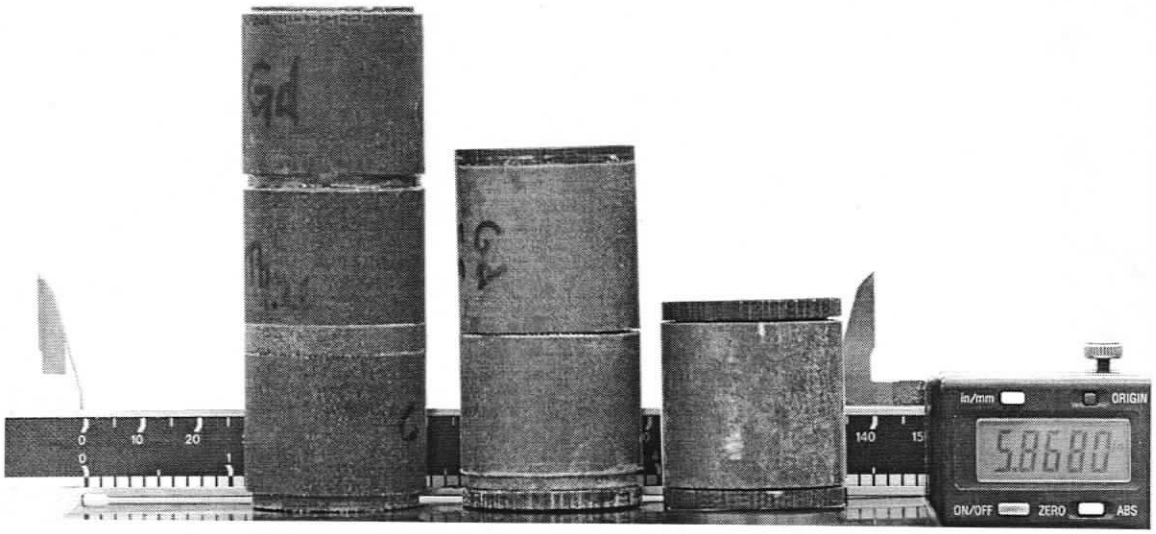

Figure 3-10. Single, two, and three puck regenerators.

The regenerator is a modular unit composed of one or more AMR pucks (Figure 3-10). Each puck has an outer phenolic shell, a structural support, and it is filled with a magnetic porous matrix, which is the refrigerant. This allows for testing with a

combination of pucks, using different refrigerants. The shell is made of a phenolic tube with perforated caps on either end. The ends are designed so that the individual pucks are stackable in a male-female fashion, so that it is possible to build up a linear array. The refrigerant matrix is epoxy impregnated inside the phenolic shell to produce a monolithic particle bed. The epoxy is used to hold the particles together, which otherwise may be dislodged by the magnetic forces. If the epoxy impregnation process is performed correctly, the pressure drop through the monolithic bed should deviate little from that for a particle bed without impregnation. Particles are irregularly shaped, but are sifted through meshes to reduce the distribution in particle size as much as possible. The characteristic equivalent diameter for the particles being used is on the order of 560 microns. This dimension is based on an equivalent sphere diameter given by the ratio of particle volume to surface area. Figure 3-10 illustrates single, two, and three puck regenerators with flux shims. For the alloys and particles currently tested, each puck typically contains between 40 and 45 g of refrigerant with a porosity of approximately 55%.

Table 3-2. AMRTA specifications.

Variable	***Apparatus Range***
Frequency (Hz)	0.2-1.2
Flux Density (T)	0-5
Pressure (atm)	0-10
Heat sink (K)	263-313
Coolant	50% water 50% glycol
Coolant working pressure (atm)	0-10
Coolant flowrate (L/min)	0-6.5
He max flowrate (g/s)	2
Regenerator max size (cm)	2.5 dia x 8.8 long
Refrigeration Load (W)	0-50
Phasing resolution (deg)	5
Working phase (deg)	90
Stroke (cm)	50
Stroke adjustment (cm)	+/- 4.5

3.2.2 Instrumentation

The objective of the AMRTA instrumentation is to collect the information needed to characterize the performance of a given regenerator bed. More specifically, the temperature span, temperature profile, and cooling power need to be mapped over a range of operating conditions. Performance values are obtained as frequency, hot temperature sink, helium pressure, and heat load are varied. Table 3-3 lists the instrumented parameters and the corresponding transducers.

Table 3-3. Instrumented properties in the apparatus.

Parameter	*Transducer*
(1) Top Regenerator Hot Temperature [K]	PRT 100 Ω from Sensing Devices Inc
(2) Top Regenerator Cold Temperature [K]	PRT 100 Ω from Sensing Devices Inc
(3) Bottom Regenerator Cold Temperature [K]	PRT 100 Ω from Sensing Devices Inc
(4) Bottom Regenerator Hot Temperature [K]	PRT 100 Ω from Sensing Devices Inc
(5) Interface Regenerators Hot/Bottom [K]	PRT 100 Ω from Sensing Devices Inc
(6) Gearbox Frequency [Hz]	Incremental Optical Encoder from BEI
(7) Helium Pressure [atm]	PX 603 from Omega
(8) Rail Temperature [K]	PRT 100 Ω from Sensing Devices Inc
(9) Bearing Temperature [K]	PRT 100 Ω from Sensing Devices Inc
(10) Festo Displacer Temperature [K]	Type E thermocouple from Omega
(11) Coolant flowing in the Cylinder [K]	Type E thermocouple from Omega
(12) Coolant flowing out of the Cylinder [K]	Type E thermocouple from Omega
(13) Coolant Flow Rate [GPM]	Flowmeter FTB 4605 from Omega

The regenerator temperatures, gearbox frequency, and helium pressure are necessary to interpret the AMR performance. Frequency and helium pressure are required to estimate the flow rate and utilization, Φ. The other transducers monitor the working conditions of the apparatus to guarantee that experiments are conducted consistently, and to ensure that the device is working properly. Two PRTs collect the temperature at the rail and bearings providing an indication of heat leaks and heat generation; while two thermocouples measure the coolant temperature at the inlet and outlet of the cylinder. Furthermore, a thermocouple measures the gas displacer temperature, and a flowmeter and a pressure gauge are used to monitor the coolant. Cooling power is tested by applying a known load using an electric heater controlled by

a power supply. Additional information on the instrumentation set up can be found in Appendix A.

3.2.3 Upgrades

A number of upgrades were performed on the AMRTA, improving performance, flexibility, consistency, reliability, and data acquisition throughout the past two years.

The integration of the Neslab recirculating chiller in the system has been the most significant improvement. Previously city water in an open loop was used as the hot temperature sink. Temperature and flow rate fluctuations made it difficult to perform consistent tests. The chiller allows experiments to be repeated with great accuracy such that the the hot temperature sink can be set with a resolution of 0.2 K or better. Final steady state temperatures are in agreement within the accuracy of the measurement. The chiller also allows for the hot source to be varied between +40 °C and -20 °C. This permits mapping AMR performance over a broad range of heat rejection temperatures. Finally this device is also used to provide pre-cooling to the cylinder rails; this compensates for the heat generated by the bearing friction while operating the apparatus, thus minimizing heat leaks from the bearing pads into the regenerator. The chiller cooling line splits inside the apparatus into a rail cooling line and a cylinder heat exchanger line, and then rejoins before the chiller inlet. Two valves allow for independently regulating the flow into the cylinder and rail. During pre-cooling the cylinder valve is closed, the rail valve is open and the chiller temperature is set at a value below the hot sink test temperature. During the subsequent test the rail valve is closed, the cylinder valve is open and the chiller temperature is set at the hot sink temperature. A more effective implementation would be to use two chillers to independently control the heat sink and the rails. However the current set up gives satisfactory results, and an upgrade would add cost and complexity.

Early experiments showed that utilization values of the system were low, meaning that the fluid thermal mass flux was small relative to the thermal mass of the AMRs. Therefore a second Festo displacer was installed, doubling the flow rate and therefore the utilization. The introduction of a second displacer dramatically improved the performance of the AMRTA. Current data shows that higher flow rate, which could be obtained by either increasing the working pressure or the volume of gas displaced, could further improve the performance. The introduction of the additional displacer has caused

larger reciprocating forces in the system, thus further modifications of some components were required. A larger displacer connecting rod and support brackets were necessary. Also, a stiffening stainless steel angle was bolted onto the apparatus platform next to the gearbox to minimize its deflections during operation.

One of the key design features of the AMRTA is the ability to quickly change AMRs to test different sizes and materials. A number of small modifications were performed in order to streamline the procedure of replacing regenerators:

a. Vacuum shell front lid trolley - the lid is permanently mounted on a roll-away trolley for easy single-person operation.

b. On-lid mounted turbo pump - the vacuum system is permanently attached to the front lid and no longer requires disconnecting.

c. New regenerator wiring feedthrough with harness quick-connect - this new design, illustrated in Figure 3-8, is strong, reliable and easy to operate.

d. Chiller drain valve - a drain valve installed on the chiller return line, next to the chiller return inlet fitting, allows for a fast drain and easy coolant collection. Coolant is generally reused for the next set of experiments.

Thanks to these modifications, downtime for AMR replacement has been drastically reduced. Tests using different regenerators can now be performed within the same day.

The data acquisition system has been progressively upgraded with the purpose of collecting more system parameters, having more control of the experimental conditions, and displaying a more effective GUI:

a. Layer interface PRTs: with the interface temperature transducers it is possible to have some insight of the refrigeration contribution from each layer. In addition, they allow for depicting a coarse temperature distribution of the entire regenerator.

b. Inlet and outlet heat exchanger coolant temperature transducers: two E type thermocouples have been installed in order to ensure that experiments are started with the hot sink set at a desired temperature. In addition, their temperature readings, in combination with the hot temperature PRT reading, give some indication of the heat rejection by the AMR.

c. Displacer temperature transducer: a type-E thermocouple is installed to monitor displacer heating by friction. Forced air convection is used to keep these pneumatic cylinders cool.

d. Coolant flowmeter: monitoring coolant flow rate is needed to ensure consistent flow among experiments, to have a feedback on valve regulation and to check for obstructions.

e. Bearing temperature PRT: monitoring the bearing temperature allows some control over friction heating and heat leaks. Data from this transducer is also used as a boundary condition for heat leak numerical simulations.

f. Updated LabView VI: a new program now runs the virtual instruments and data logging. New channels have been added to accommodate for the additional transducers. Transfer functions have been removed from the program, being now defined within the NiDaq software as virtual channels. Custom peak-hold functions displays allow for more reliable and simplified readings of the maximum values sampled. Helium flow rate, utilization, and temperature span are real time evaluated, charted and logged.

The superconducting magnet has also received a number of upgrades:

a. Improved thermal contact of the HTSC leads: a design flaw in the in house built magnet is the poor location of the HTSC leads since these components are far from the cryocooler cold finger. A long thermal path leads to a high thermal resistance. The hot side of the HTSC leads needs to be thermally linked to the cryocooler first stage, so that the Joule heating of the copper leads does not transfer into the superconducting leads. Therefore, the thermal path to the cryocooler has a great impact on the maximum operating current. A ½ inch (12.7 mm) copper plate with large cross sectional area has been installed between the coldfinger and HTSC leads to short the thermal circuit. The plate was rigidly mounted to the cryocooler first stage and flexibly attached to the hot end of the HTSC leads. Indium foil was used to minimize the interface thermal resistance. Previously the HTSC leads were instead connected to the strongback (see Figure 3-1).

b. Flexible first stage connection: originally the cryocooler first stage was directly bolted onto the strongback. This is ideal to maximize thermal contact, however

it adds mechanical stress to the coldfinger due to differential thermal expansion. Thus, a copper flexible connection has been implemented instead.

In conclusion the hardware upgrades allowed for an increase in the operating envelope, faster set up time and, most importantly, greater control over the operating conditions. Indeed the AMRTA has given proof of great experimental repeatability.

Chapter 4
Experimental Results

This chapter presents the experimental results obtained during the past two years. Single material and multi-material AMRs have been tested under a variety of conditions. The objective was to determine the temperature span sensitivity as a function of hot heat sink temperature, operating frequency, utilization, and applied load. In addition layered AMR performance was compared to single material regenerators with the objective of verifying if the multi-material performance could be superior and under which conditions. All experiments were conducted with same field distribution and intensity (2 T).

Although interesting data can be obtained during transient operating conditions, the primary interest is the performance at steady state. Figure 4-1 shows a typical plot of regenerator temperatures over time from start to end of an experiment. The data displayed specifically refers to a two layer AMR (Gd stacked on $Gd_{.74}Tb_{.26}$) with the hot temperature set at 304 K, a pressure of 9.5 atm, and frequency of 0.65 Hz. At the beginning of the test, the AMR has an approximately uniform temperature of 290 K. As the experiment proceeds, the temperature on the hot end of the regenerator approaches the hot heat sink temperature of 304 K while the temperature between the two layers and on the cold end decrease gradually to their steady-state values.

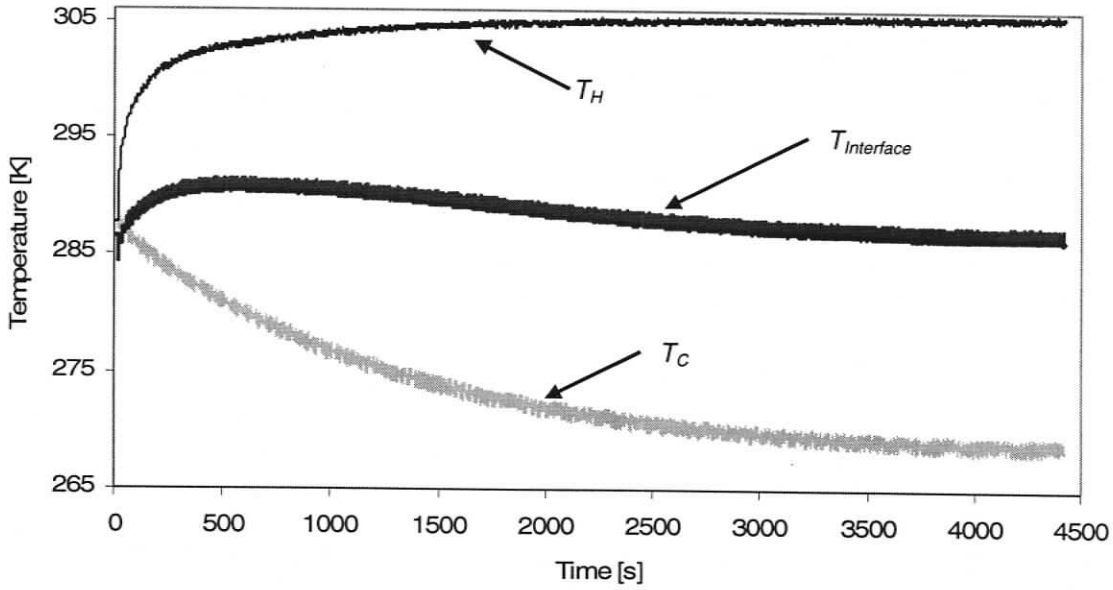

Figure 4-1. Temperature as function of time for a Gd-$Gd_{.74}Tb_{.26}$ two layer regenerator.

It might not be obvious from the plot that the AMR had reached steady state when the experiment was stopped. However, waiting longer to see the lines become flatter could greatly increase the experimentation time, adding a considerable amount of operating hours to the apparatus and requiring additional and more costly maintenance and downtime. Furthermore, operating for greater lengths of time results in larger thermal leaks into the regenerator. As a consequence the AMR might never reach a true steady-state, and the cold end would gradually rise after reaching a minimum. Therefore, it was decided to define steady-state when no increment in temperature span is recorded for a time span of 200 seconds. Numerous experimental tests showed that this criterion provided a reasonable indication of steady state temperature span.

4.1 Single Layer Regenerators

The first set of experiments focused on the characterization of single puck beds. In these experiments, regenerator geometry, bed porosity, and field intensity were all fixed with the specific values listed in Table 3-2. Single material beds are low aspect ratio beds, 25 mm long and 25 mm in diameter. A key objective of this thesis is to determine how these layers perform as part of a multilayered regenerator; therefore, these single layer experiments were used to quantify how each layer behaves individually before stacking them together. Only temperatures on the hot and cold ends of the puck were measured. As already described in the apparatus design section, the reciprocating cylinder carries two regenerators, symmetrically installed in the top and bottom ends, each of which are equally instrumented. In all tests the data collected from each regenerator differed by 0.3 K or less.

4.1.1 Methodology

The experimental strategy focused on quantifying the performance sensitivity as function of utilization, hot heat sink temperature, frequency, and heat load. The primary metric for "good" performance is increased temperature span, while a secondary metric is the sensitivity of span to cooling power. The following experiments were performed on Gd single puck regenerators:

1. Temperature span versus utilization, Φ, by adjustment of system pressure
2. Temperature span versus heat rejection temperature, T_H
3. Temperature span versus heat load, Q_c

$Gd_{.74}Tb_{.26}$ and $Gd_{.85}Er_{.15}$ pucks were tested only for heat rejection temperature sensitivity whereas the Gd pucks were characterized for all three variables. Table 4-1 summarizes the experiments performed on single layer regenerators.

Table 4-1. Single layer regenerator experiments.

AMR	*Fixed Parameters*	*Values*	*Independent Variables*	*Range*
Gd	Frequency [Hz]	0.65	Pressure [atm] Temperature [K]	3, 6, 9.5 303, 270
Gd	Pressure [atm] Frequency [Hz]	9.5 0.65	Temperature [K]	310.7, 306.6, 303, 297.1, 292, 284.6
Gd	Pressure [atm] Frequency [Hz]	9.5 0.65	Heat Load [W] Temperature [K]	0, 6 304, 294, 288
$Gd_{.85}Er_{.15}$	Pressure [atm] Frequency [Hz]	9.5 0.65	Temperature [K]	290.2, 281, 275.8, 273, 268, 262.2, 257
$Gd_{.74}Tb_{.26}$	Pressure [atm] Frequency [Hz]	9.5 0.65	Temperature [K]	300.8, 294.6, 290.5, 287.8, 281.5, 278.2, 272.5

Utilization, Φ

The first set of experiments measures no-load temperature span as a function of utilization. Utilization is one of the non-dimensional parameters governing AMR performance discussed in Chapter 2. By varying the pressure of the helium in the system the mass of fluid passing through the regenerator can be adjusted, which also alters the ratio of fluid thermal mass to regenerator thermal mass. Figure 4-2 illustrates the utilization and pressure relation for the case of a 45 g gadolinium AMR (single puck), at room temperature. Although the gas displacers are rated for up to 10 atm, the maximum mean pressure must not exceed 9.5 atm so as to accommodate the pressure drop across the regenerator.

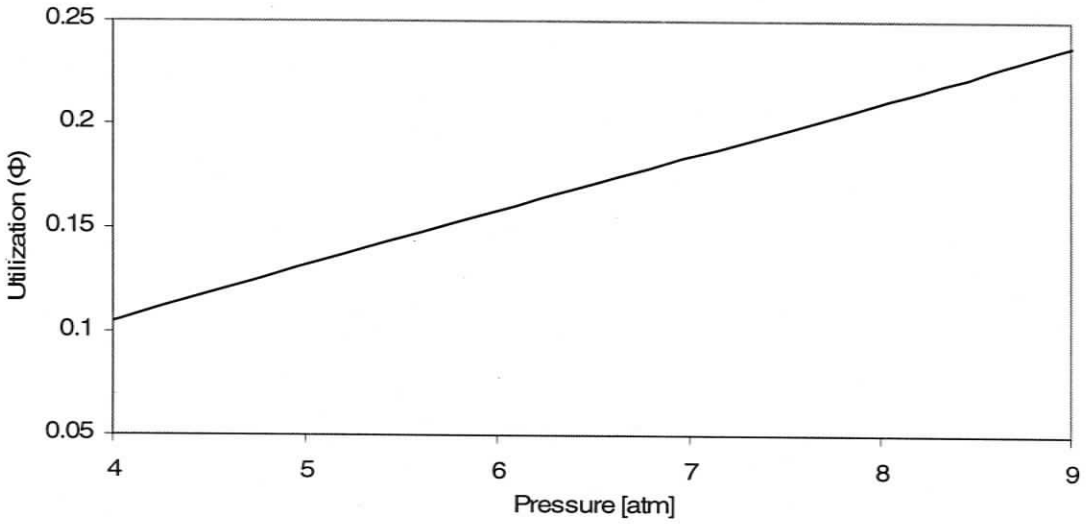

Figure 4-2. Pressure and utilization relationship a, single puck AMR.

Figure 4-3 and Figure 4-4 illustrate the results obtained for selected pressures and heat rejection temperatures, T_H. Temperature span measurements were obtained for T_H = 303, 292, 270 K, and operating pressure of 9.5, 6, and 3 atm. The operating frequency was set at 0.65 Hz.

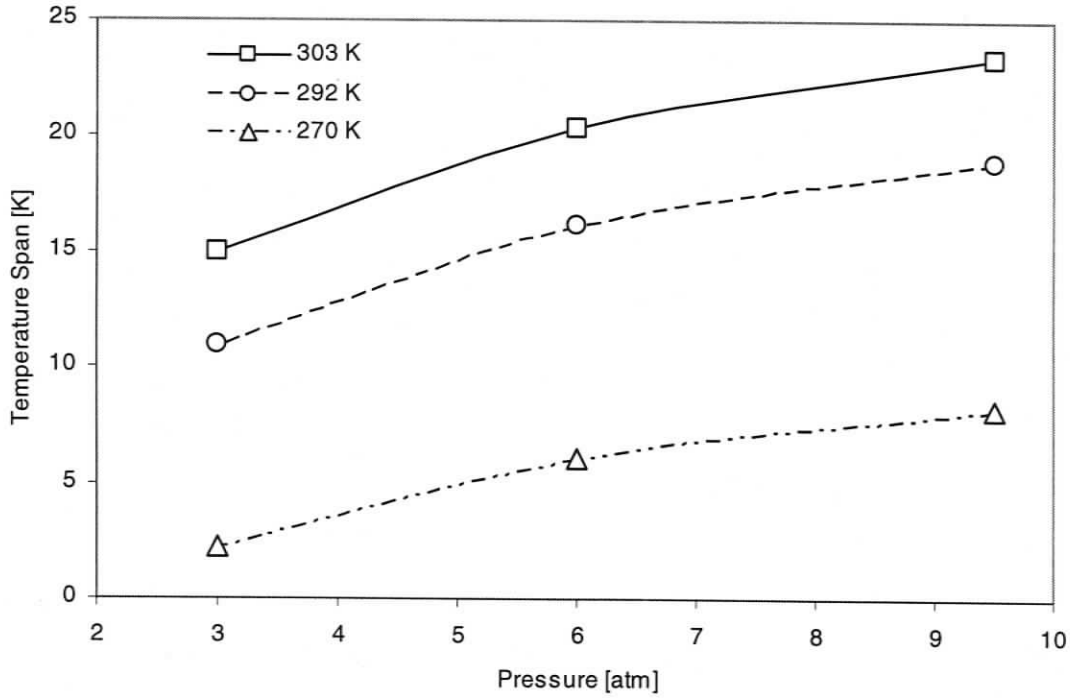

Figure 4-3. Gadolinium single puck regenerator temperature span versus pressure at various T_H.

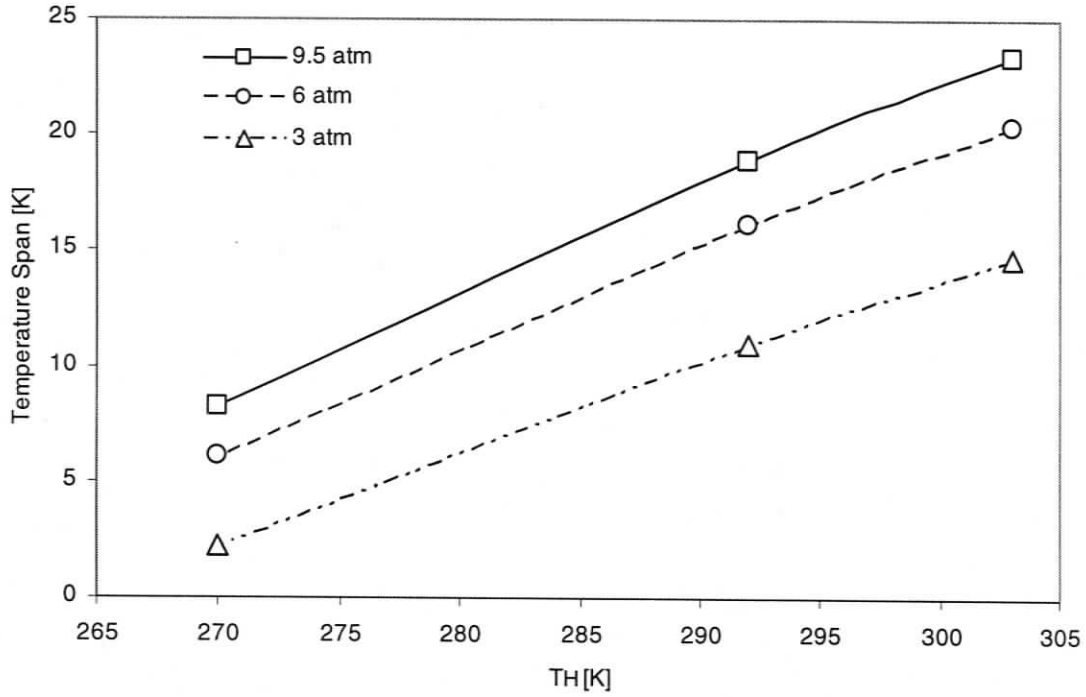

Figure 4-4. Gadolinium single puck regenerator temperature span as T_H is varied at 0.65 Hz and pressures of 3, 6, and 9.5 atm.

The plots clearly show that temperature span increases monotonically with pressure or utilization ($\frac{\Delta T_{span}}{\Delta \Phi} > 0$) over the range of values tested. Thus, a higher pressure may be desirable. It is expected that past a certain utilization the performance would eventually start declining ($\frac{\Delta T_{span}}{\Delta \Phi} < 0$) and some evidence of this can be seen in Figure 4-3. These results and the implications of utilization will be discussed further in Chapter 5.

Heat Rejection Temperature

Operating at maximum pressure, a set of experiments were performed in order to map the temperature span against T_H. Figure 4-5 illustrates the results. The plot shows the performance of Gd, $Gd_{.74}Tb_{.26}$ and $Gd_{.85}Er_{.15}$ single puck regenerators. The Gd AMR attained a maximum temperature span of 23.4 K, $Gd_{.74}Tb_{.26}$ 20.45 K, and $Gd_{.85}Er_{.15}$ 24.1 K. It can also be noted that, for Gd, the peak temperature span was obtained with the hot sink at 304 K, ~10 K above the phase transition temperature. Similarly, for the $Gd_{.74}Tb_{.26}$ and $Gd_{.85}Er_{.15}$ AMRs the peak temperature spans was obtained respectively at 290 K, ~12 K above its transition temperature, and at 280 K, ~15 K above its reported

transition temperature. In general, all three materials tend to behave in a similar manner, with maximum temperature spans being achieved when the materials are operating near their respective Curie points. An unexpected finding is that the $Gd_{.85}Er_{.15}$ composition produced a larger maximum span than the Gd.

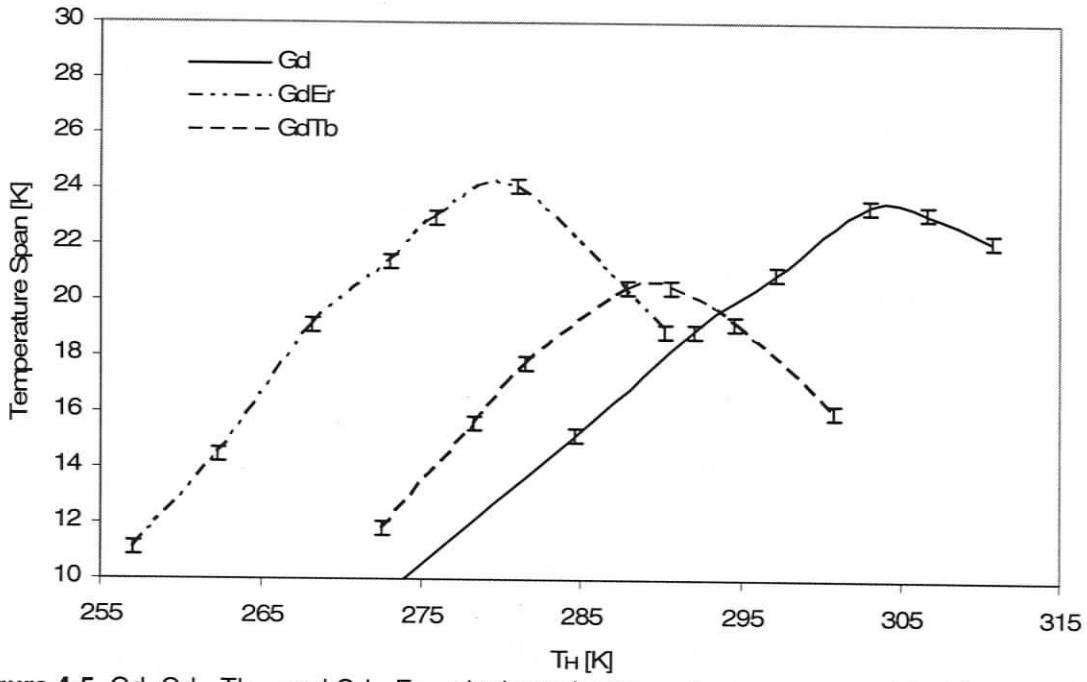

Figure 4-5. Gd, $Gd_{.74}Tb_{.26}$ and $Gd_{.85}Er_{.15}$ single puck temperature span versus T_H with no load at 0.65 Hz and 9.5 atm.

Heat Load

Using single puck Gd AMRs, a set of heat load tests were performed with T_H at 304 K, 294.4 K, and 288.4 K. Helium pressure was set at 9.5 atm and frequency at 0.8 Hz. Figure 4-6 illustrates the results of these tests compared to the no-load curves. For all three operating conditions the heat load sensitivity is close 1 K/W. Surprisingly, heat load sensitivity displayed no dependency on T_H in the tested temperature range (288-304 K). Other tests showed that in the 0-6 W range single puck regenerators displayed a linear variation of span as a function of cooling power with a deviation smaller than the sensor accuracy.

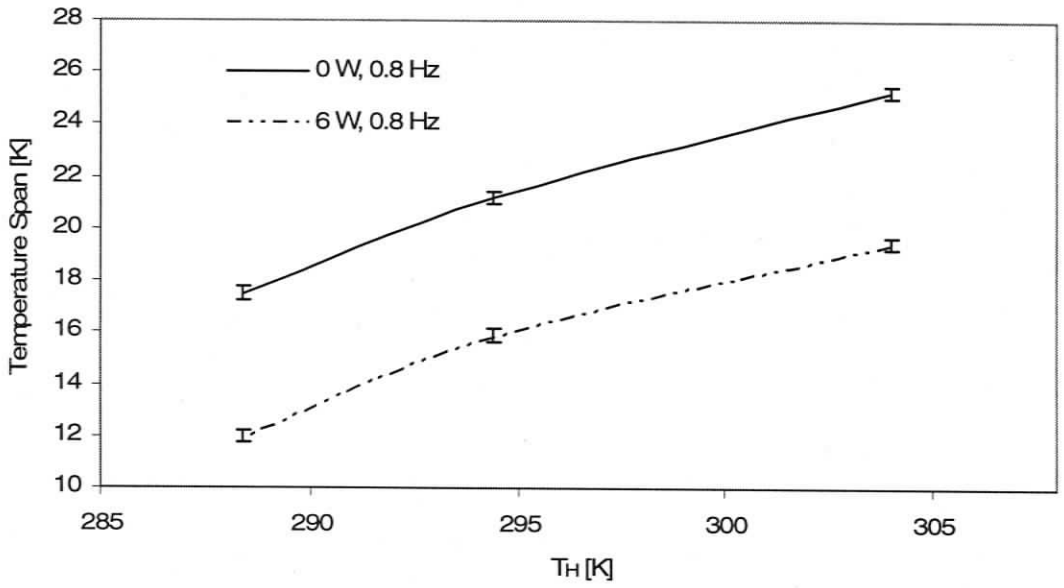

Figure 4-6. Gd single puck temperature span versus heat load at 0.8 Hz and 9.5 atm.

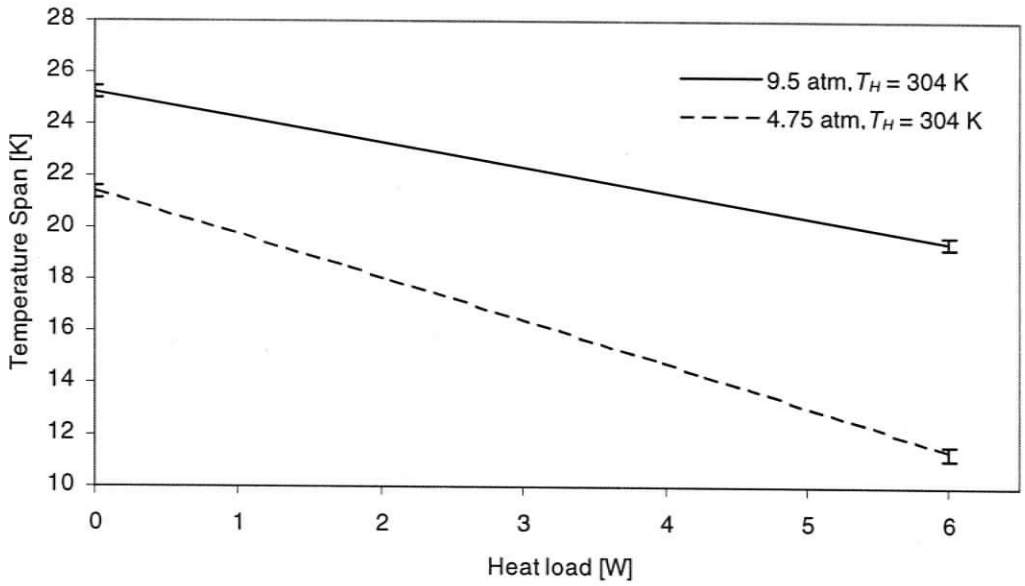

Figure 4-7. Gd single puck temperature span for 0 and 6 W at 0.8 Hz and 9.5 and 4.75 atm.

Figure 4-7 illustrates that cooling power is also affected by the helium pressure. At 4.5 atm heat load sensitivity increased to 1.7 K/W, about 40% larger than the 9.5 atm case.

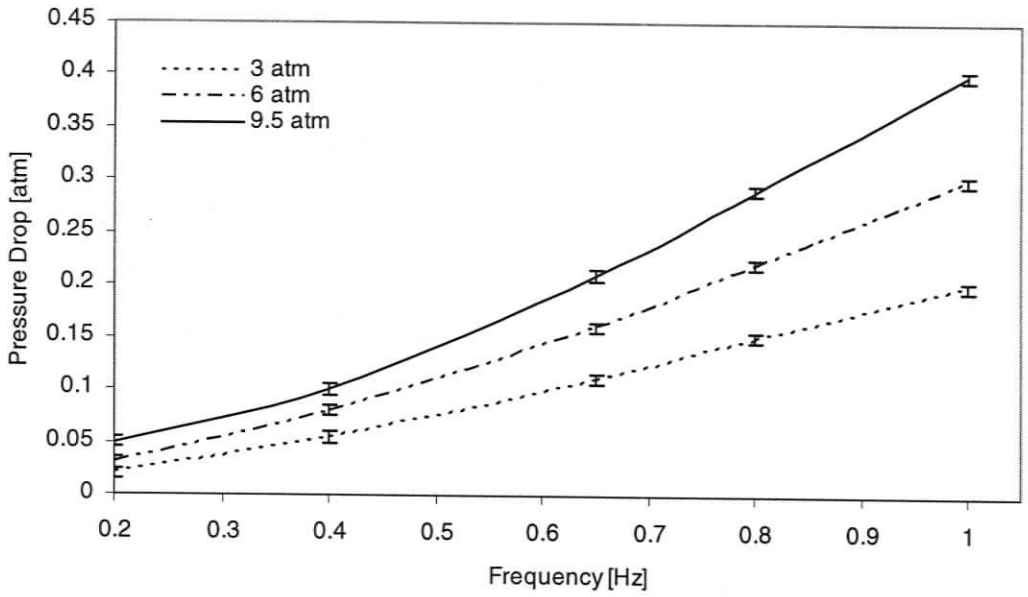

Figure 4-8. Pressure drop for a single puck AMR at room temperature.

All tests showed that AMR performance benefits from increasing heat transfer fluid pressure and operating frequency, however both parameters are strongly associated with the fluid pressure drop. Figure 4-8 shows that pressure drop increases exponentially with frequency and pressure penalizing the system efficiency.

4.2 Multi-Layered Regenerators

The AMRTA allows regenerators up to 8 cm in length to be tested. Currently individual pucks are 2.5 cm long, therefore a combination of up to 3 layers can be used. Multi-puck regenerators allow for the creation of multi-layer single material or multi-layer multi-material AMRs. For instance, it is possible to test a double gadolinium layer AMR, referred to as a Gd-Gd regenerator, or a Gd-$Gd_{.74}Tb_{.26}$ AMR, which is composed of one puck of gadolinium and another of $Gd_{.74}Tb_{.26}$. This design permits a direct comparison of the performance of single material regenerators to multi-material ones, to observe the contributions of each layer, and to compare the performance of each layer as part of a larger AMR. Layering of different materials is one way of increasing the temperature span and cooling power, but until recently has been unproven [10].

4.2.1 Multiple Layer Experimental Strategy and Results

Multi-layer AMR experiments are summarized as follows:

- Gd-Gd regenerator set:
  - 9.7 atm 0.65 Hz, T_H varying between 285.3 K and 310 K
  - 9.7 atm 0.8 Hz, thermal loading at 309.6 K and 303.5 K
- Gd-$Gd_{.74}Tb_{.26}$ regenerator set:
  - 9.7 atm 0.65 Hz, T_H varying between 285.5 K to 311 K
  - 8 atm 0.65 Hz, T_H varying between 286 K to 310 K
  - 5 atm 0.65 Hz, T_H varying between 385.5 K to 310.3 K
  - 9.7 atm 304 K, frequency mapping for 0.65, 0.8, and 1 Hz
  - 9.7 atm 0.8 Hz, thermal loading at 306
- Gd-$Gd_{.85}Er_{.15}$ regenerator set:
  - 9.7 atm 0.65 Hz, T_H varying between 285 K and 311 K
- Gd-$Gd_{.74}Tb_{.26}$-$Gd_{.85}Er_{.15}$ regenerator set:
  - 9.5 atm 0.65 Hz, T_H varying between 284.7K and 311 K
  - 6 atm 0.65 Hz, T_H varying between 285.3 K and 311.5 K
  - 3 atm 0.65 Hz, T_H varying between 385.5 K and 311.5 K
  - 9.7 atm 0.8 Hz, thermal loading at 301.5, 296, and 288 K

The two layer experiments are also summarized in the following table. In the "range" field each tested experiment is listed.

Table 4-2. Two layer regenerator experiments.

AMR	*Fixed Property*	*Values*	*Varying Proprerty*	*Range*
Gd-Gd	Pressure [atm] Frequency [Hz]	9.7 0.65	Temperature [K]	310, 306.2, 299.5, 292.4, 285.3
Gd-Gd	Temperature [K] Pressure [atm] Frequency [Hz]	303.5 9.7 0.8	Heat Load [W]	0, 2, 4, 6, 8, 10
Gd-Gd	Temperature [K] Pressure [atm] Frequency [Hz]	309.6 9.7 0.8	Heat Load [W]	0, 2, 4, 6, 8, 10
$Gd\text{-}Gd_{.74}Tb_{.26}$	Pressure [atm] Frequency [Hz]	9.7 0.65	Temperature [K]	311.3, 304.2, 302.5, 296.5, 290.5, 285.57
$Gd\text{-}Gd_{.74}Tb_{.26}$	Pressure [atm] Frequency [Hz]	8 0.65	Temperature [K]	310, 303, 299.5, 296, 286
$Gd\text{-}Gd_{.74}Tb_{.26}$	Pressure [atm] Frequency [Hz]	5 0.65	Temperature [K]	310.3, 302.7, 301, 298, 285.5
$Gd\text{-}Gd_{.74}Tb_{.26}$	Pressure [atm] Frequency [Hz]	9.7 0.65	Temperature [K]	311, 308, 306, 304, 289.6, 285.5
$Gd\text{-}Gd_{.74}Tb_{.26}$	Temperature [K] Pressure [atm]	304 9.7	Frequency [Hz]	0.65, 0.8, 1
$Gd\text{-}Gd_{.74}Tb_{.26}$	Temperature [K] Pressure [atm] Frequency [Hz]	298 9.7 0.8	Heat Load [W]	0, 2, 4, 6, 8, 10
$Gd\text{-}Gd_{.74}Tb_{.26}$	Temperature [K] Pressure [atm] Frequency [Hz]	306 9.7 0.8	Heat Load [W]	0, 4, 8
$Gd\text{-}Gd_{.85}Er_{.15}$	Pressure [atm] Frequency [Hz]	9.7 0.65	Temperature [K]	311, 304.4, 302, 298, 290, 285.5
$Gd\text{-}Gd_{.85}Er_{.15}$	Temperature [K] Pressure [atm] Frequency [Hz]	290, 298, 306 9.5 0.8	Heat Load [W]	0, 4, 8

Gd-Gd Tests

Two layer Gd-Gd AMRs were tested in order to determine their performance in terms of temperature span and cooling power. Figure 4-9 illustrates the regenerator temperature span (overall and individual pucks) as the hot temperature is varied from 285.3 K to 310 K. The maximum temperature span was found to be 36.6 K at T_H = 310 K. The performance results for T_H > 310 K are not plotted because they were generally unrepeatable, varying over a broad range of values. This is likely due to an underlying instability and low cooling power and is discussed further in Chapter 5. Figure 4-10 illustrates the hot end, interface, and cold end temperatures for the same tests. The dashed horizontal line represents the transition temperature for gadolinium. When both pucks are below T_{Curie} the hotter one develops the larger temperature span, however the bottom puck rapidly increases its performance when the top one is above T_{Curie}.

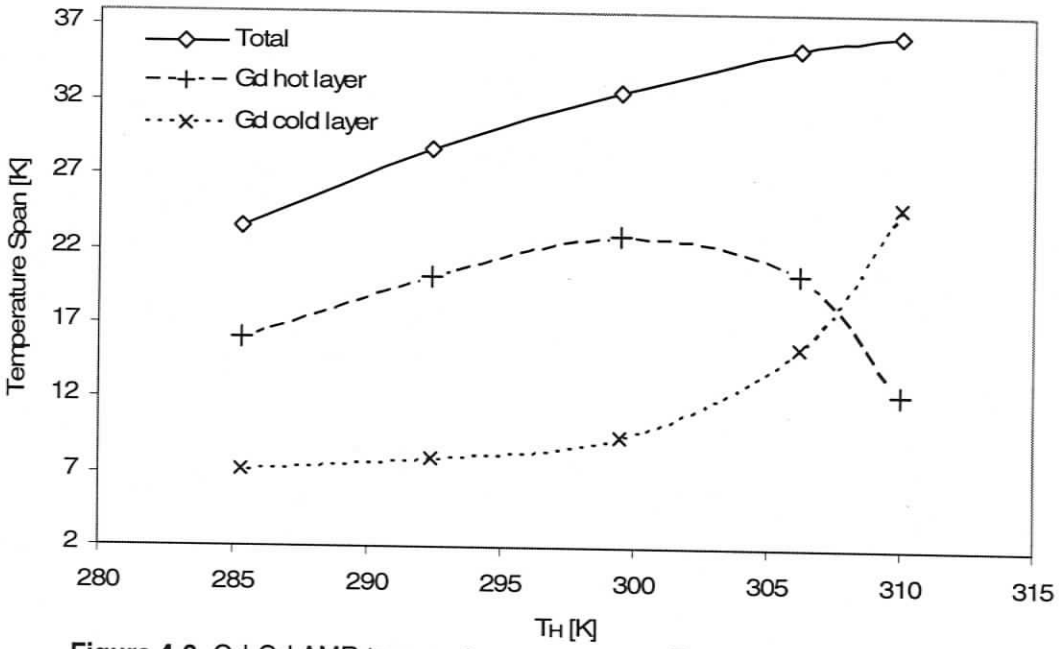

Figure 4-9. Gd-Gd AMR temperature span versus T_H at 9.5 atm and 0.65 Hz.

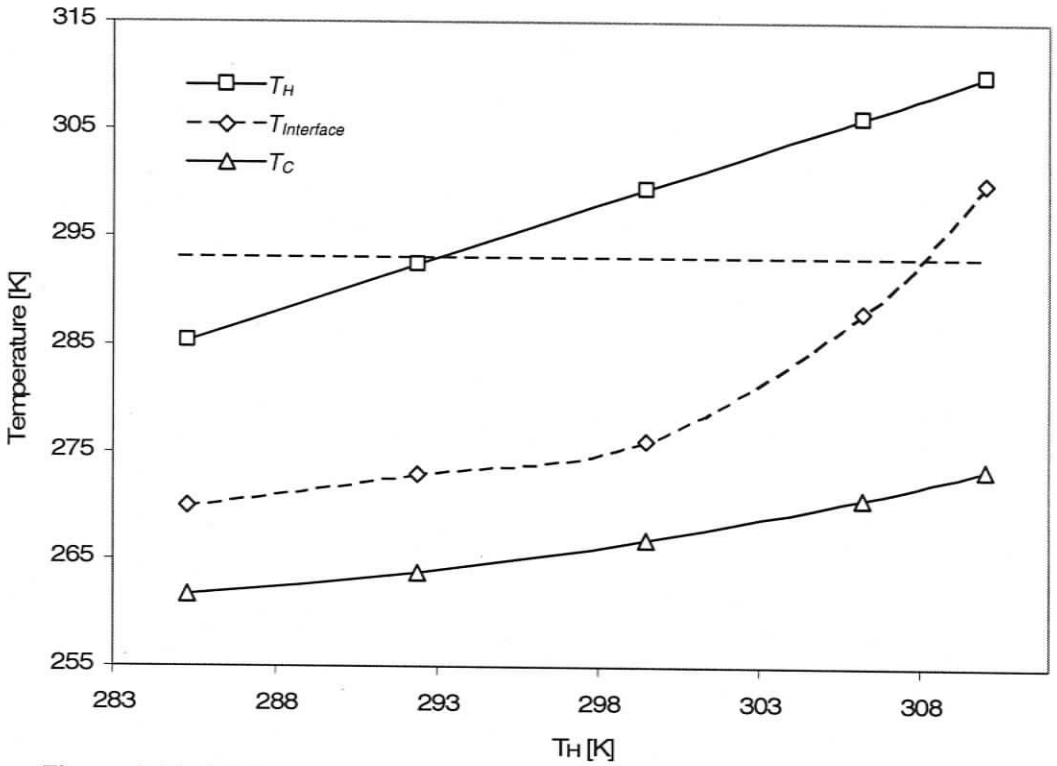

Figure 4-10. Gd-Gd AMR temperature distribution versus T_H at 9.5 atm and 0.65 Hz.

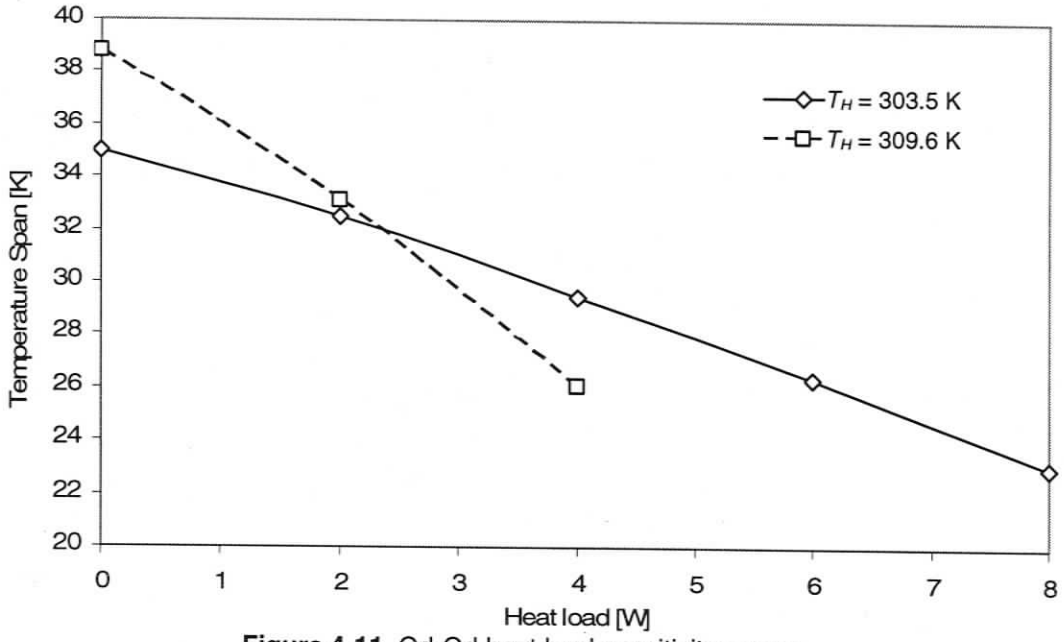

Figure 4-11. Gd-Gd heat load sensitivity curves.

Figure 4-11 illustrates the cooling power plots for T_H= 309.6 K and T_H= 303.5 K. The hotter case has a temperature span of 38.8 K at 0.8 Hz and with no load, however it drops rapidly even with small loads (~3.5 K/W). At 6 W the span becomes unstable and

thus, is not shown. Although the no-load temperature span is lower than the case at 310 K, at T_H = 303.5 the AMR is stable and much less sensitive to heat loading. The lowest heat load sensitivity was 1.5 K/W for T_H = 303.5 K.

Gd-$Gd_{.74}Tb_{.26}$ Tests

The decision to couple a Gd puck with a $Gd_{.74}Tb_{.26}$ puck was made because the $Gd_{.74}Tb_{.26}$ transition temperature is ~278 K, and appears to be a good match for the gadolinium layer operating near its Curie temperature. Figure 4-12 illustrates test results for temperature span as a function of T_H in the range of from 285.5 to 311 K. Individual layer contributions are also plotted. A maximum span of 39.9 K is achieved at T_H = 306 K. For T_H < 306 K the span across the individual layers tends to decrease as the hot heat sink temperature is decreased. For higher hot sink temperature the $Gd_{.74}Tb_{.26}$ layer temperature span increases while the Gd layer temperature span decreases.

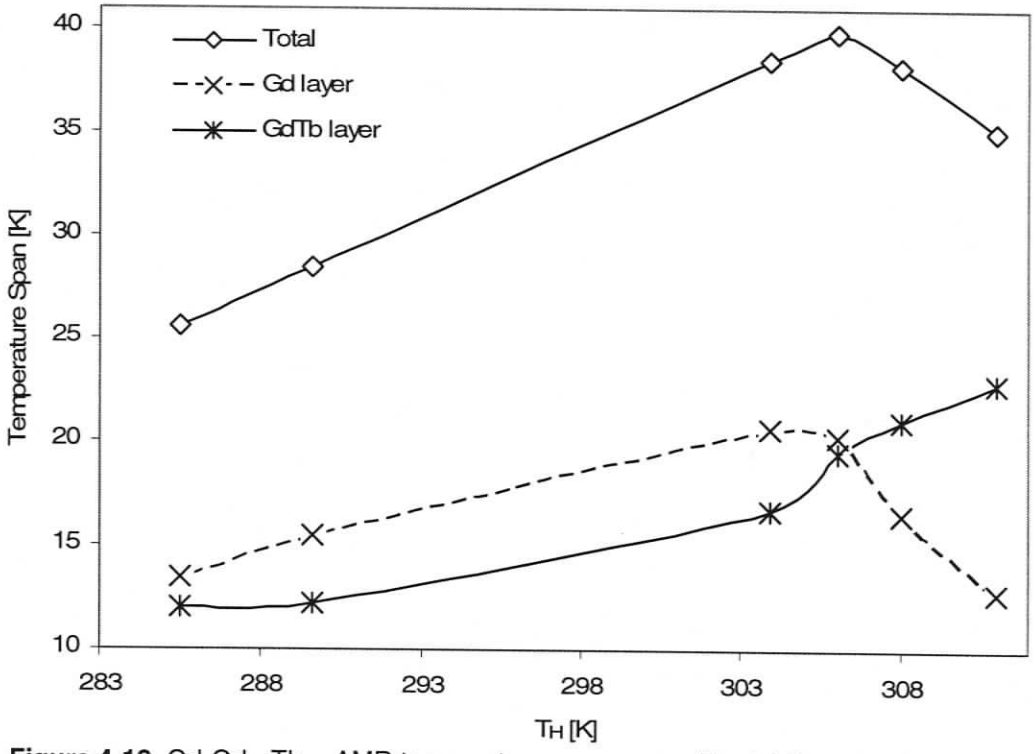

Figure 4-12. Gd-$Gd_{.74}Tb_{.26}$ AMR temperature span versus T_H at 9.5 atm and 0.65 Hz.

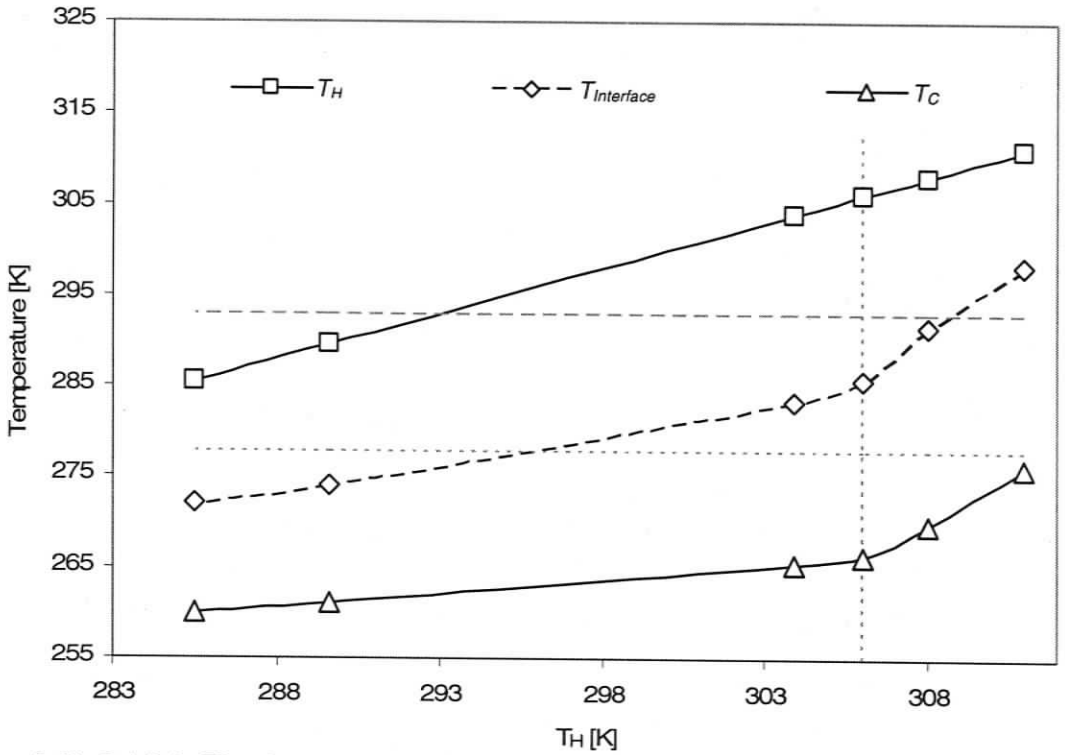

Figure 4-13. Gd-$Gd_{.74}Tb_{.26}$ hot, cold and interface T versus T_H at 9.5 atm and 0.65 Hz.

Figure 4-13 illustrates the regenerator temperature distribution for the maximum pressure case of 9.5 atm. Hot, cold, and interface temperatures are plotted for a range of heat rejection temperatures. The horizontal lines represent the Curie temperatures for each layer, and the vertical line highlights the T_H for which maximum temperature span is obtained (T_{Hmax}). T_{Hmax} seems also to mark a change in regenerator sensitivity to T_H. Interestingly, when operating with $T_H = T_{Hmax}$ both pucks operate with the hot-end well above their respective Curie temperature.

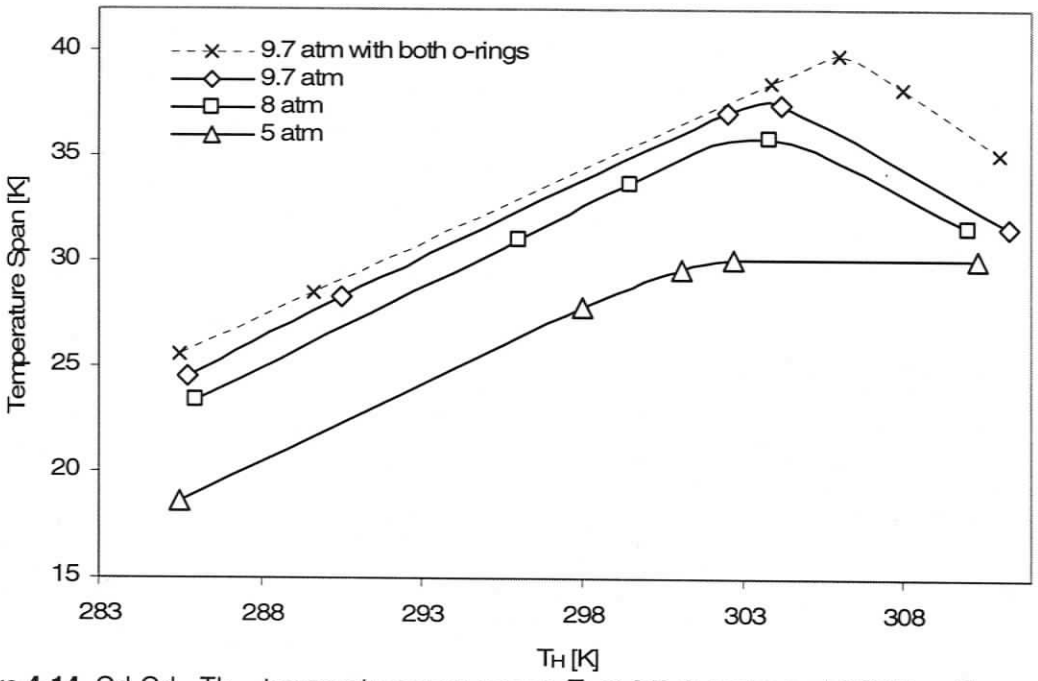

Figure 4-14. Gd-$Gd_{.74}Tb_{.26}$ temperature span versus T_H at 9.7, 8, 5 atm and 0.65 Hz with one o-ring missing.

Figure 4-14 illustrates the temperature span of Gd-$Gd_{.74}Tb_{.26}$ AMR as function of T_H, for 9.7, 8 and 5 atm. As with the single puck results, the AMR was found to perform better with higher pressure. After completing this set of experiments, it was discovered that an o-ring sealing the regenerator was missing. The purpose of the seal is to ensure that helium does not bypass the regenerator by flowing in the gap between the shell and the cylinder bore. The 9.7 atm temperature set was repeated, this time with the o-ring in place, resulting in a 6.5% peak temperature span increase, from 37.5 K to 40 K. Interestingly, the peak also shifted to higher T_H, from 304 K to 306 K. The larger temperature span and the T_{Hmax} shift are the result of an increase in cooling power. It is expected that the 8 and 5 atm performances were similarly affected, although not necessarily to the same degree. These tests were not repeated.

The sensitivity of temperature span to frequency is shown in Figure 4-15. The AMR displays an almost linear behavior with a slope of 9 K/Hz. The plot also shows that from 0.65 to 1 Hz pressure drop rise from 0.5 to 1 atm, while the temperature span is augmented by only 7%. Figure 4-16 displays the Gd-$Gd_{.74}Tb_{.26}$ cooling power sensitivity curve for a hot sink temperature of 306 K. The average heat load sensitivity was found to be approximately 1.5 K/W.

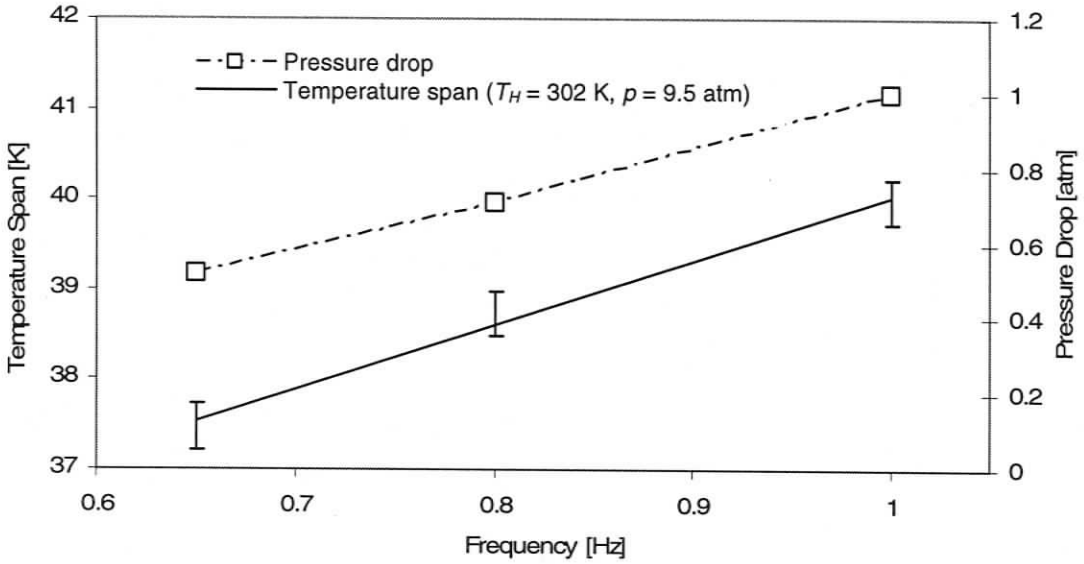

Figure 4-15. Gd-$Gd_{.74}Tb_{.26}$ frequency sensitivity test at 9.7 atm and T_H = 304 K for temperature span and pressure drop.

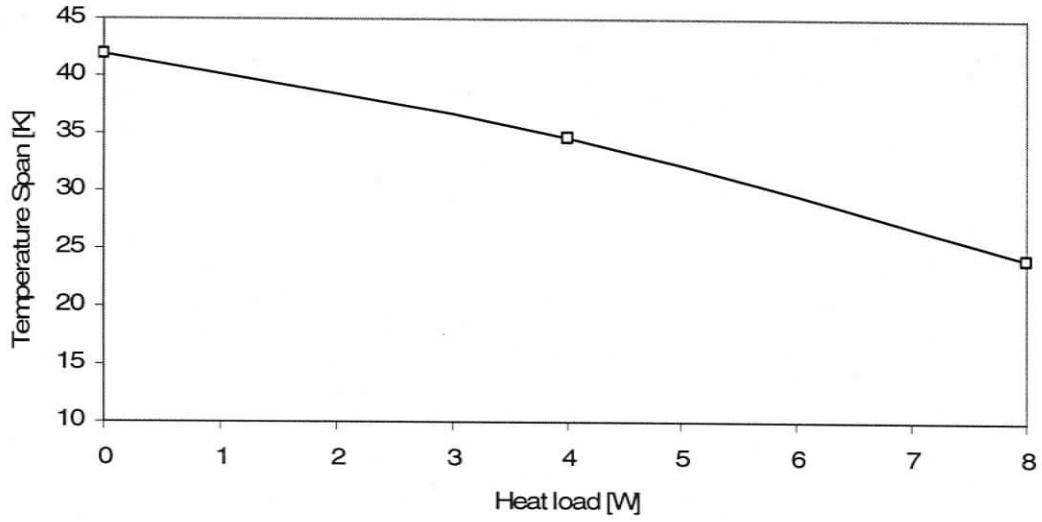

Figure 4-16. Gd-$Gd_{.74}Tb_{.26}$ heat load sensitivity at 9.7 atm, T_H = 306 K and 0.8 Hz.

Gd-$Gd_{.85}Er_{.15}$ Tests

Gd was also coupled with $Gd_{.85}Er_{.15}$. $Gd_{.85}Er_{.15}$ has a lower Curie temperature (265 K) than $Gd_{.74}Tb_{.26}$, and a smaller MCE, however, in the single puck experiments, it displayed a larger temperature span. Thus, good performance was expected by coupling this layer with a Gd layer. Figure 4-17 illustrates the temperature span of Gd-$Gd_{.85}Er_{.15}$ AMR and of the individual layers as function of T_H, for 9.5 atm and 0.65 Hz. A maximum span of 42.5 K was achieved at T_H = 302.5 K. Both layers maximized their span for T_H at approximately 303 K. The temperature span of the $Gd_{.85}Er_{.15}$ layer was found to be nearly constant between 283 K and 303 K.

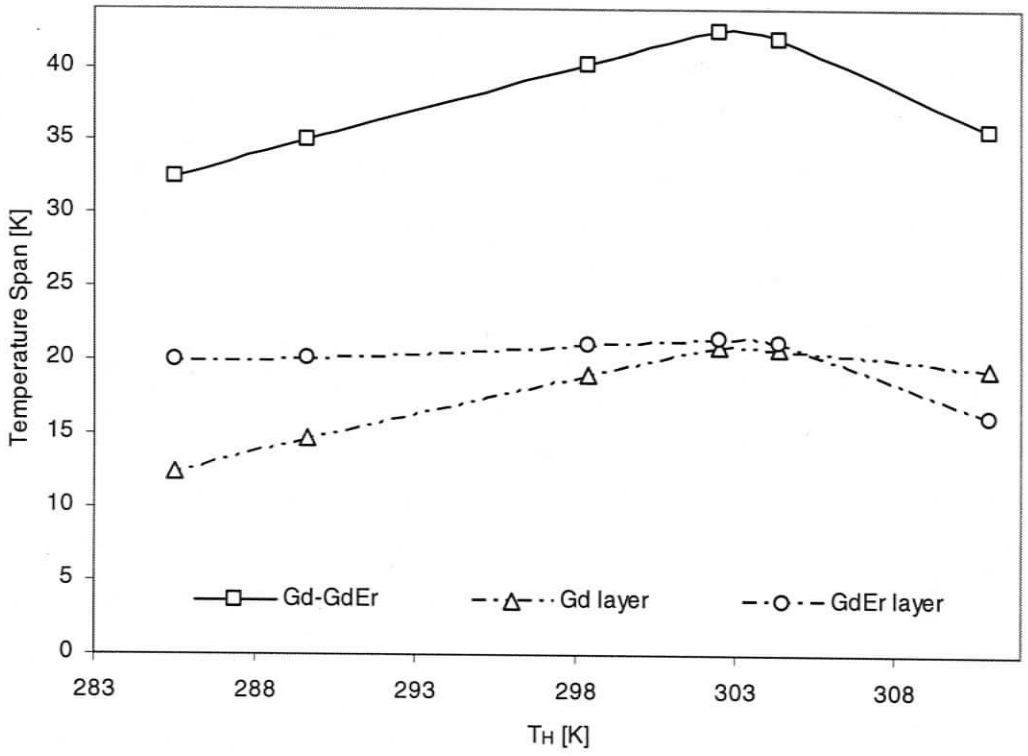

Figure 4-17. Gd-$Gd_{.85}Er_{.15}$ AMR temperature span versus T_H at 9.5 atm and 0.65 Hz.

Figure 4-18 shows the regenerator temperature distribution (T_H, $T_{interface}$, and T_C) as a function of T_H. As with the Gd- $Gd_{.74}Tb_{.26}$ AMR tests, when operating with $T_H = T_{Hmax}$ both pucks operated with their hot-end above their respective Curie temperature. However, in this case the Gd puck hot-end was found to be cooler while for the $Gd_{.85}Er_{.15}$ puck the hot end was considerably above its transition temperature (~21 K hotter). Figure 4-19 illustrates the regenerator heat sensitivity with loads of 0, 4 and 8 W. Heat rejection

temperatures were set at 306, 298 and 290 K. This plot shows how the load sensitivity, which ranged between a minimum of 1.6 K/W and a maximum of 2.7 K/W, varies with T_H. As expected the hottest heat rejection temperature displayed the most sensitivity while there was no significant difference between the other two cases.

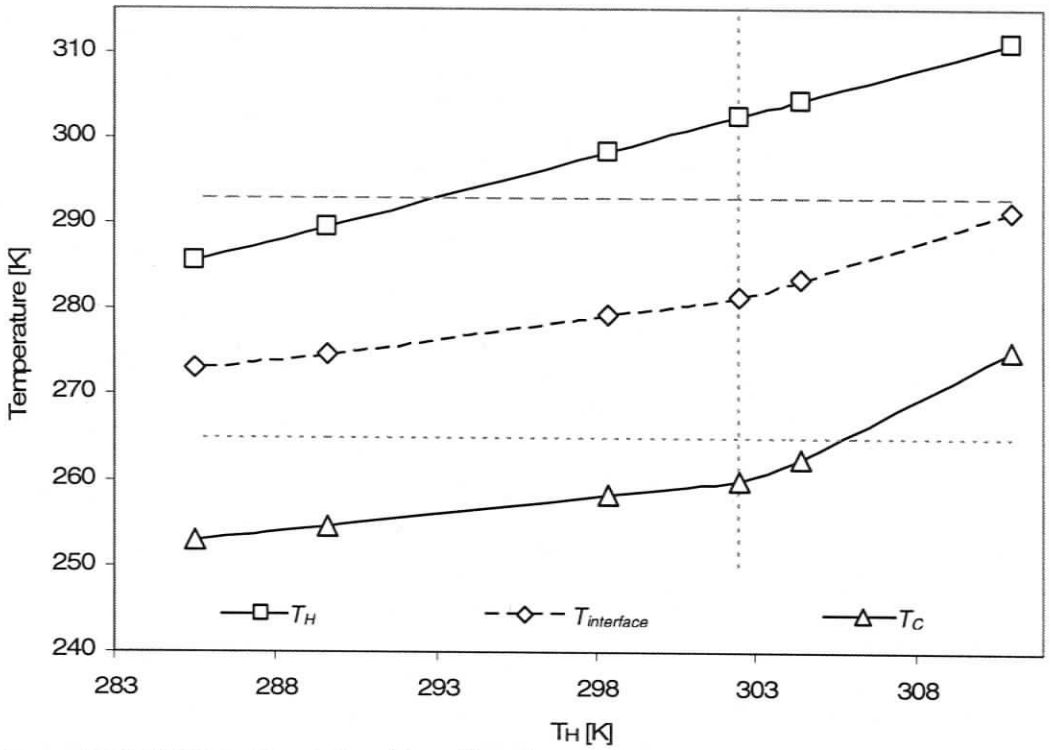

Figure 4-18. Gd-$Gd_{.85}Er_{.15}$ hot, cold and interface temperatures vs T_H at 9.5 atm and 0.65 Hz.

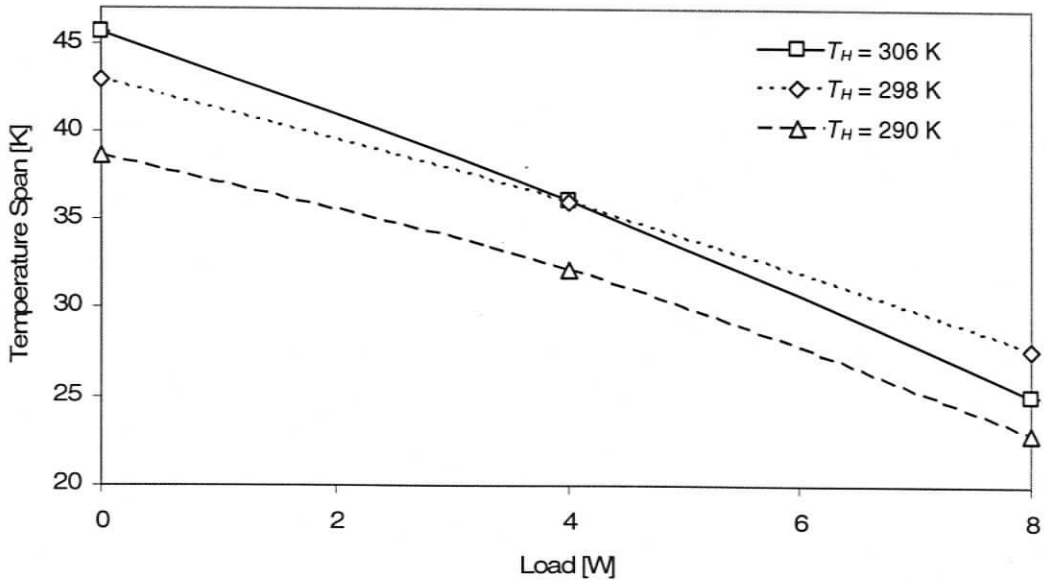

Figure 4-19. Gd-$Gd_{.85}Er_{.15}$ heat load sensitivity at 9.5 atm, T_H = 306, 298, 290 K and 0.8 Hz.

Three Layer Regenerator Tests

Three layer experiments were conducted using a Gd puck for the hot end, a $Gd_{.74}Tb_{.26}$ puck for the middle section, and a $Gd_{.85}Er_{.15}$ puck for the cold end. Previous tests using a two layer Gd-$Gd_{.74}Tb_{.26}$ AMR showed that, for T_H = 306, the cold side of the $Gd_{.74}Tb_{.26}$ puck reached 266 K (see Figure 4-12). Thus, the $Gd_{.85}Er_{.15}$ puck, with a 260 K transition temperature should be in its MCE operating range. Adding a material that has a Curie point near 260 K should increase the effective MCE, and, hopefully, the temperature span and cooling power when compared to a one-material, three layer AMR (Table 4-3 summarizes the experiments performed on three layer AMRs).

Table 4-3. Three layer regenerator experiments.

AMR	*Fixed Property*	*Values*	*Varying Property*	*Range*
Gd-$Gd_{.74}Tb_{.26}$-$Gd_{.85}Er_{.15}$	Pressure [atm] Frequency [Hz]	9.5 0.65	Temperature [K]	311, 305.4, 301.5, 297.5, 293.9, 284.7
Gd-$Gd_{.74}Tb_{.26}$-$Gd_{.85}Er_{.15}$	Pressure [atm] Frequency [Hz]	6 0.65	Temperature [K]	311.3, 307.3, 302.7, 298.7, 292.5, 285.3
Gd-$Gd_{.74}Tb_{.26}$-$Gd_{.85}Er_{.15}$	Pressure [atm] Frequency [Hz]	3 0.65	Temperature [K]	311, 305.8, 301.4, 298.4, 292, 286
Gd-$Gd_{.74}Tb_{.26}$-$Gd_{.85}Er_{.15}$	Temperature [K] Pressure [atm] Frequency [Hz]	301 9.5 0.8	Heat Load [W]	0, 2, 4, 6, 8, 10
Gd-$Gd_{.74}Tb_{.26}$-$Gd_{.85}Er_{.15}$	Temperature [K] Pressure [atm] Frequency [Hz]	296 9.5 0.8	Heat Load [W]	0, 2, 4, 6, 8, 10
Gd-$Gd_{.74}Tb_{.26}$-$Gd_{.85}Er_{.15}$	Temperature [K] Heat Load [W]	288 0; 4; 8	Heat Load [W]	0, 2, 4, 6, 8, 10

Figure 4-20 shows the results for the Gd-$Gd_{.74}Tb_{.26}$-$Gd_{.85}Er_{.15}$ AMR operating with no applied load, and operating pressure and frequency set at 3, 6, and 9.5 atm, and 0.65 Hz respectively. A maximum temperature span of 46.8 K is obtained for 9.5 atm and T_H = 301.5 K. The 3 and 6 atm tests achieved 25% and 55% lower peak temperature spans. For the 3 atm case, the cooling power was so small that some tests needed to be repeated several times in order to obtain useful data. Interestingly, the curve was found to be much steeper when operating at 9.5 atm than 3 and 6 atm. A single test with T_H = 302 K and the operating frequency set at 1 Hz reached the largest temperature span to date of 51 K.

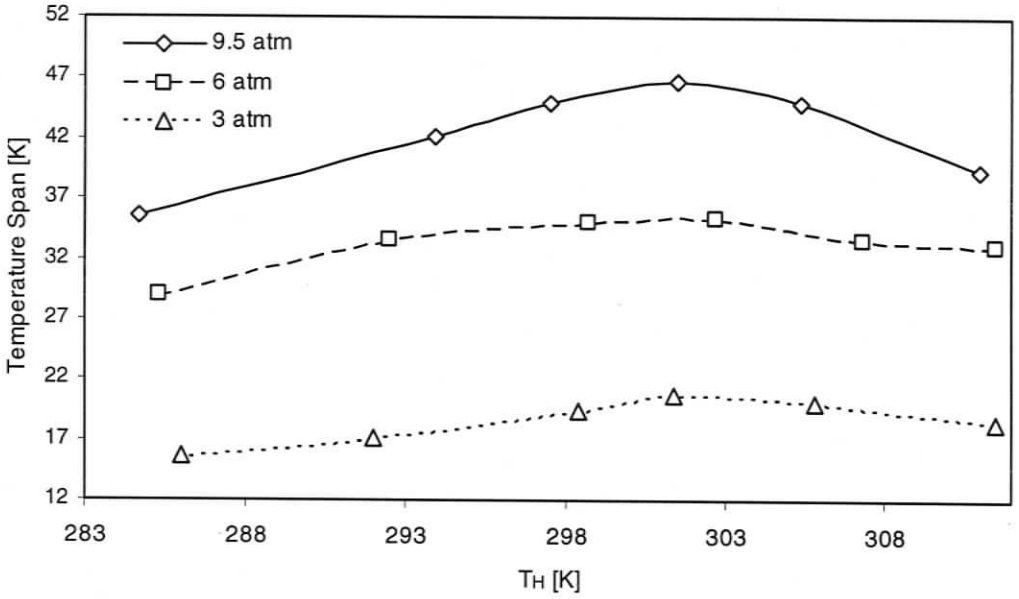

Figure 4-20. Gd-$Gd_{.74}Tb_{.26}$-$Gd_{.85}Er_{.15}$ temperature span versus T_H at 9.5, 6, 3 atm and 0.65 Hz.

Figure 4-21 illustrates the regenerator temperature distribution for the maximum pressure case of 9.5 atm. Hot, cold, and interface temperatures are plotted for a range of heat rejection temperatures. The horizontal lines represent the Curie temperatures for each layer, and the vertical line T_{Hmax}. As with to the two-layer tests, for $T_H < T_{Hmax}$ the coldest temperature achieved is relatively insensitive to T_H.

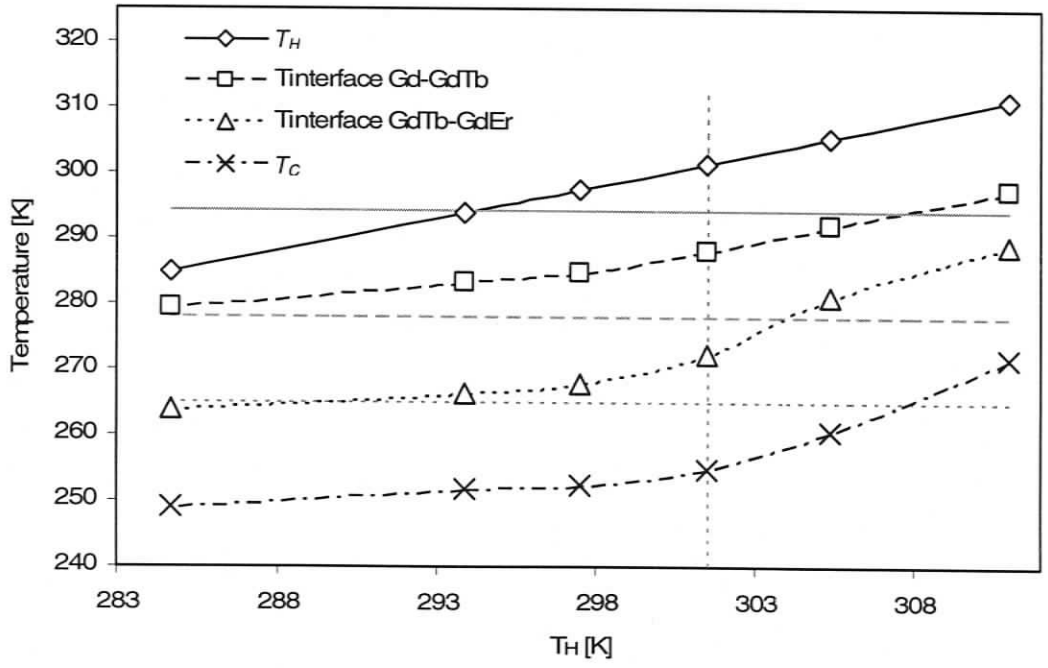

Figure 4-21. Gd-$Gd_{.74}Tb_{.26}$-$Gd_{.85}Er_{.15}$ hot, cold and interface temperatures versus T_H at 9.5 atm and 0.65 Hz.

Figure 4-22 summarizes the heat load tests performed at 9.5 atm. Each curve refers to specific heat rejection temperatures set at 301.5 K, 296 K, and 288 K. Tests with T_H > 301.5 K were not carried out because low cooling power and instability were expected in this temperature region. Results were found to be consistent with the two layer AMRs, with lower load sensitivity for T_H < 301.5 K. The minimum heat load sensitivity was found to be 1.5 K/W.

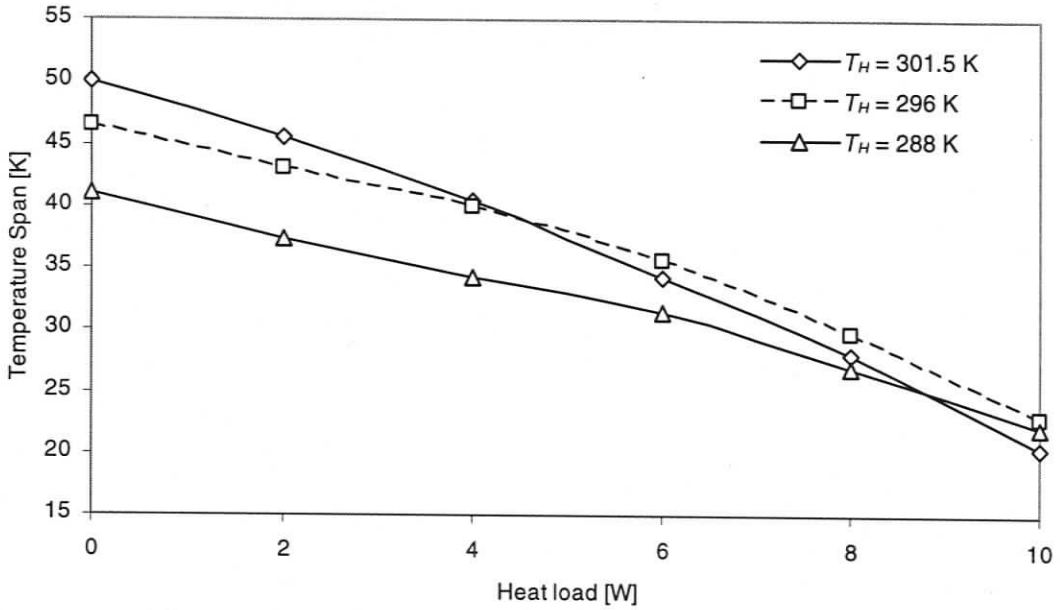

Figure 4-22. Gd-$Gd_{.74}Tb_{.26}$-$Gd_{.85}Er_{.15}$ heat load sensitivity curves.

Chapter 5
Discussion

This chapter discusses the experimental findings summarized in Chapter 4, highlighting novel results. The impact of T_H, utilization, operating frequency, and heat load are presented and compared. Furthermore, a qualitative analysis of multi-layer thermo-magnetic interaction is discussed. Finally, a heat leak analysis and an initial conditions study are presented.

5.1 Parameter Sensitivity Study

The aim of this section is to use the data collected in combination with AMR theory to analyze the behavior of the regenerators. In doing so, a path for performance improvement and future investigations is laid. Single puck regenerator results will be discussed first and multi-layer AMR discussion will follow. Figure 5-1 is a summary of all no-load results for a system pressure of 9.5 atm and operating frequency of 0.65 Hz. Single puck temperature spans are compared to two puck and three puck results.

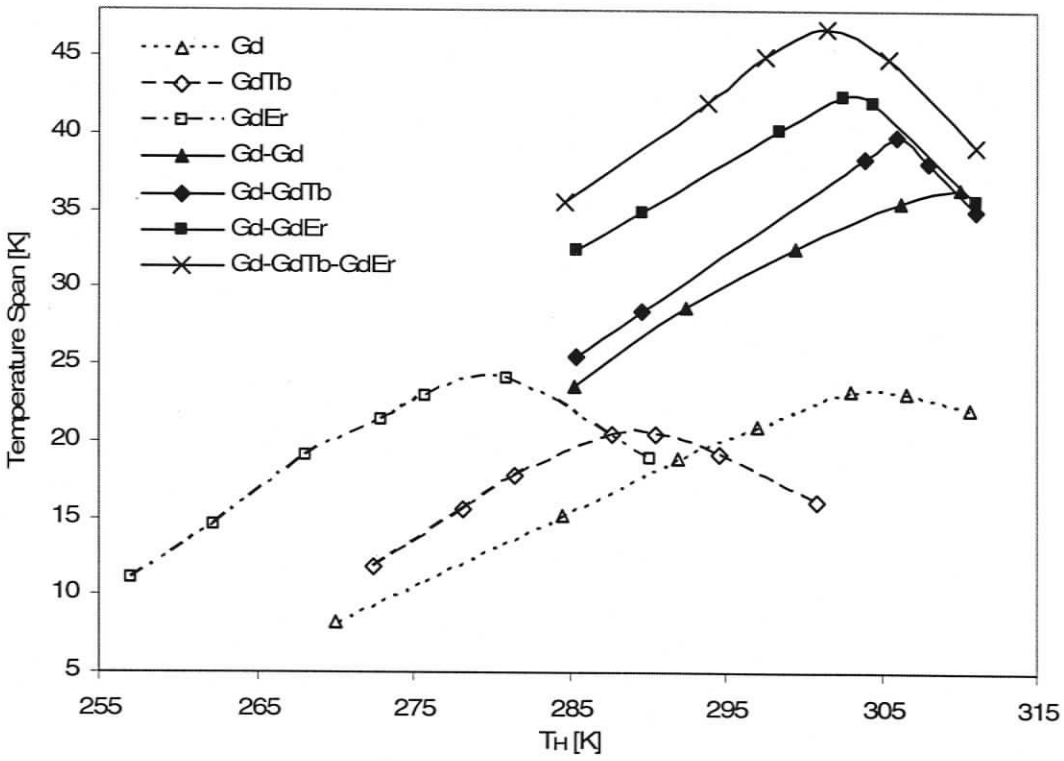

Figure 5-1. Summary of no-load 9.5 atm and 0.65 Hz results.

Single Puck Regenerators

Based on thermodynamic constraints, as discussed in Chapter 2, an AMR should not operate with a heat rejection temperature higher than its Curie temperature because a substantial reduction in temperature span and cooling power may result. This theory is based on entropy and energy balance arguments connected to specific heat and MCE variations near the transition temperature [15].

Figure 5-2 illustrates the ideal gadolinium MCE compared to the real gadolinium MCE. Equation (2.16) predicts that the ideal MCE should be a straight line with a positive slope identified by the ratio $\frac{\Delta T_{ref}}{T_{ref}}$. The length of each line matches the temperature span experimentally achieved by the AMR. Each line corresponds to the ideal distribution for a specific T_{ref}, where $T_{ref} = T_H$. For instance, the thick continuous line refers to $T_H = 303$ K with a temperature span of 23.9 K. The plot highlights that for $T_H > T_{Curie}$ the MCE has a negative slope, while the ideal MCE should be linear with a positive slope.

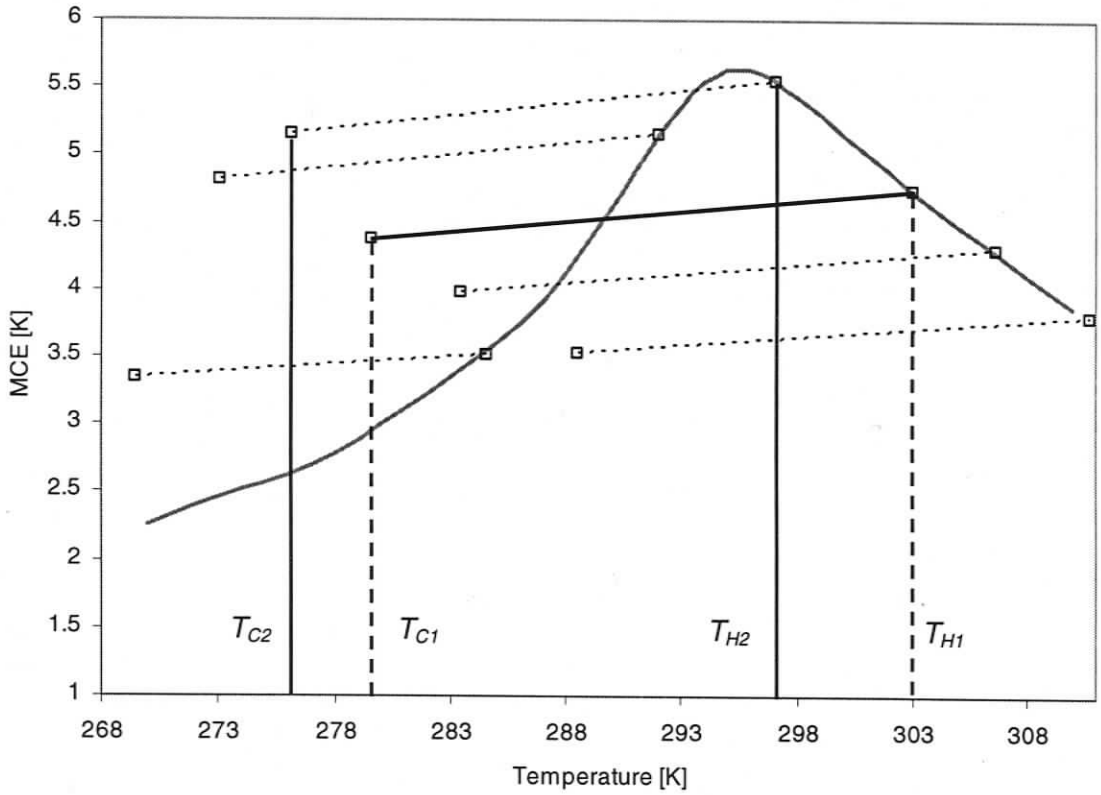

Figure 5-2. Ideal Gadolinium MCE compared to real MCE and single puck AMR data.

The question that arises is why are the maximum temperature spans occurring when T_H is greater than T_{Curie}? The experimental results suggest a progressive reduction in cooling power when T_H is increased past the Curie temperature. However, when no load is applied, the maximum temperature span is observed for a heat rejection temperature 10 to 15 K higher than the transition temperature. A plausible mechanism explaining this behavior is that the average MCE $(\overline{mce})$ is larger when operating around the Curie point (with $T_H > T_{Curie}$ and $T_C < T_{Curie}$). This may be observed from the following qualitative considerations. The average MCE can be calculated using:

$$(\overline{mce})\Big|_{\Delta T} = \frac{1}{T_H - T_c}\int_{T_c}^{T_H} (mce(T))\,dT \qquad (5.1)$$

but $T = T(x)$ and $dT = \left(\frac{dT(x)}{dx}\right)dx$

where at $x_1 = 0$, $T = T(x)$ and $x_2 = L$, $T = T(x)$.

Thus, substituting in (5.1):

$$(\overline{mce})\Big|_{L} = \frac{1}{x_2 - x_1}\int_{x_1}^{x_2} mce(T)\left(\frac{dT(x)}{dx}\right)dx \qquad (5.2)$$

If $dT/dx \simeq constant$ then $(\overline{mce})\Big|_{L} = (\overline{mce})\Big|_{\Delta T}$. Figure 5-2 qualitatively illustrates that when T_H = 303 K the $\overline{mce}$ is larger than when T_H = 297 K. Indeed, assuming the temperature profile nearly linear within the AMR, the integral in (5.1) is approximately equal to the area under the real MCE curve between 303 K and 280 K (T_{H1} - T_{C1}), when the heat rejection temperature is set at 303 K. Likewise, the same can be said for the area between 297 K and 276 K (T_{H2} - T_{C2}) when the heat rejection temperature is at 297 K.

The single material regenerator temperature spans showed similar trends when tested in the neighborhood of their respective Curie temperatures (Figure 5-1). The curves look

alike for all three cases, with each of the regenerator temperature spans being maximized when T_H is between 10 and 15 K above the respective T_{Curie}. However, based on the MCE magnitudes, $Gd_{.74}Tb_{.26}$ was expected to perform best, followed by Gd, while $Gd_{.85}Er_{.15}$ was anticipated to give the lowest temperature span. As can be seen in Figure 2-3 and Figure 2-4, Gd and $Gd_{.85}Er_{.15}$ peak zero-field specific heats are about 5% and 14% less than $Gd_{.74}Tb_{.26}$ peak respectively. Consequently, because the fluid pressures and mass fluxes were the same for all experiments, the utilizations would be different for the three materials, with $Gd_{.85}Er_{.15}$ having the largest and $Gd_{.74}Tb_{.26}$ the smallest. It is expected that Gd and $Gd_{.85}Er_{.15}$ would perform worse than $Gd_{.74}Tb_{.26}$ if the same utilization were used.

Heat Load Sensitivity

Figure 5-3 shows that heat load sensitivity for the majority of the AMRs that were tested. The sensitivity is calculated using 0 and 4 W heat load data. The plot shows that

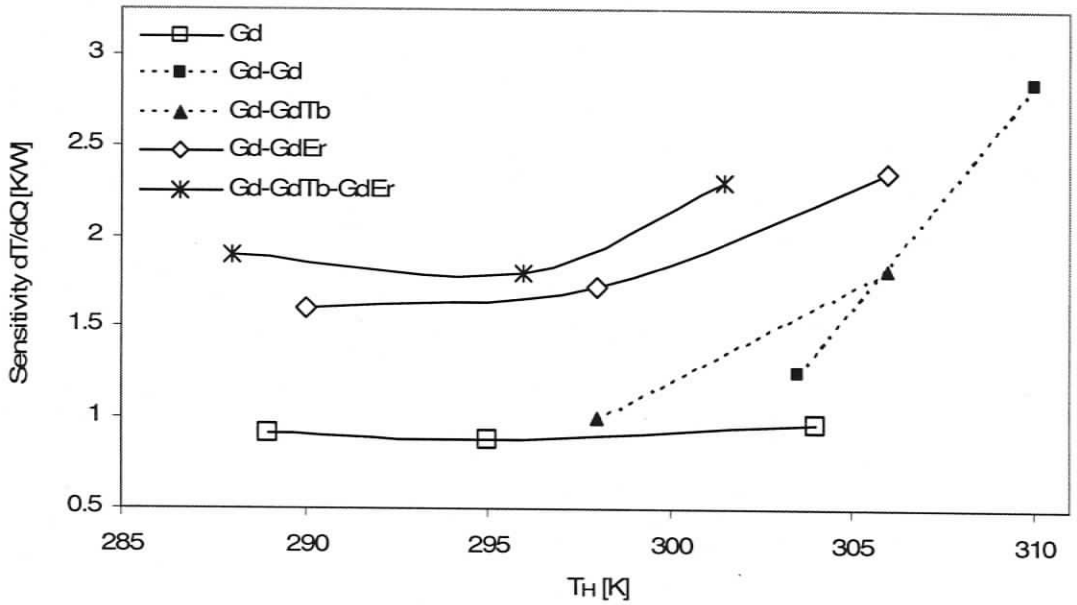

Figure 5-3. Heat load sensitivity as function of T_H for several AMRs tested.

for $T_H >> T_{Curie}$, the heat load sensitivity increases significantly. If T_H is sufficiently high, the regenerator temperature profile can be unstable even for small heat load perturbations, causing the temperature span to collapse. This was found to be the case for the Gd-Gd tests with T_H > 310 K. Based on the above arguments and the experimental data, single material AMRs should operate with $T_H = T_{Curie}$ or slightly higher. The amount by which T_{Curie} should be exceeded cannot be quantified with the

data. It can be said that the value varies with material, aspect ratio, utilization, frequency, field intensity, and cooling power.

Utilization

It has been shown that utilization is a parameter that has a large impact on AMR performance. Since utilization is directly proportional to pressure, experimental work done with the AMRTA often refers to pressure, rather than utilization, because pressure is the measured property. Figure 5-4 and Figure 5-5 illustrate the sensitivity of temperature span to pressure as T_H and operating pressure are varied for the Gd AMR. Sensitivity is the result of the ratio dT_{span}/dp, obtained by taking the derivative of the second order polynomial fits of the experimental data. As previously discussed in Section 2.3, cooling power is expected to increase with utilization up to a maximum (Φ_{max}), beyond which it starts to decline. Temperature span is believed to follow a similar trend. Both figures show positive sensitivity values ($dT_{span}/dp > 0$) for all cases, steadily decreasing with operating pressure. Experimentally, a Φ_{max} could not be found because it requires helium to be pressurized far beyond the gas displacer maximum rating of 10 atm, even when testing single 45 g puck regenerators. There are several alternative ways to experimentally prove the existence of Φ_{max}: reducing the regenerator mass, moving the operating point away from the Curie temperature, or lowering the magnetic field intensity. All solutions imply lessening the cooling power and temperature span.

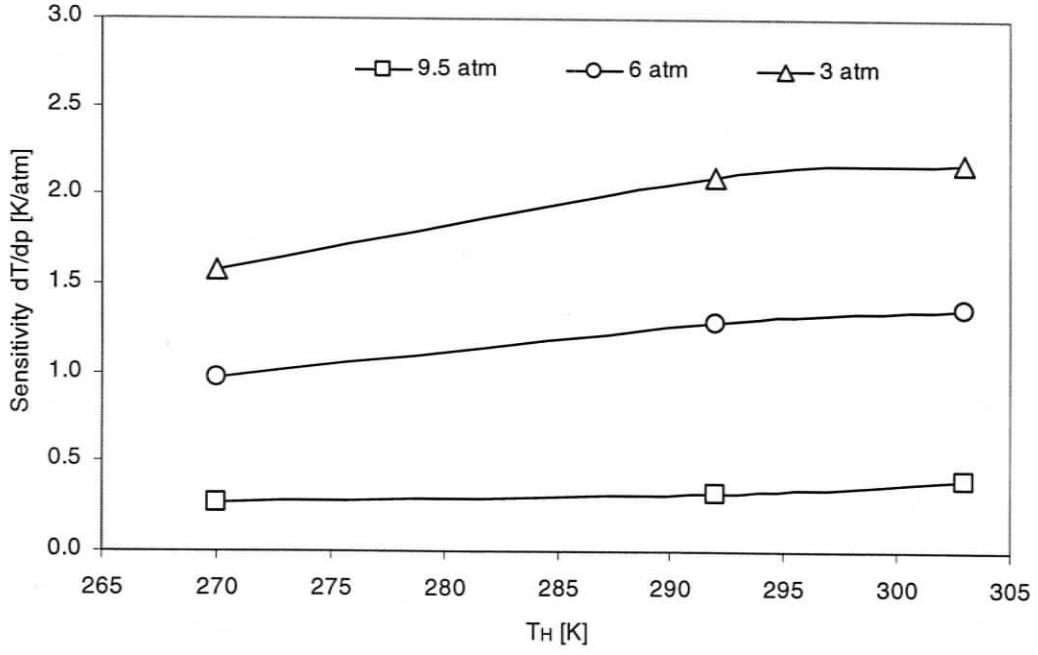

Figure 5-4. Gd AMR temperature span sensitivity to pressure as a function of T_H.

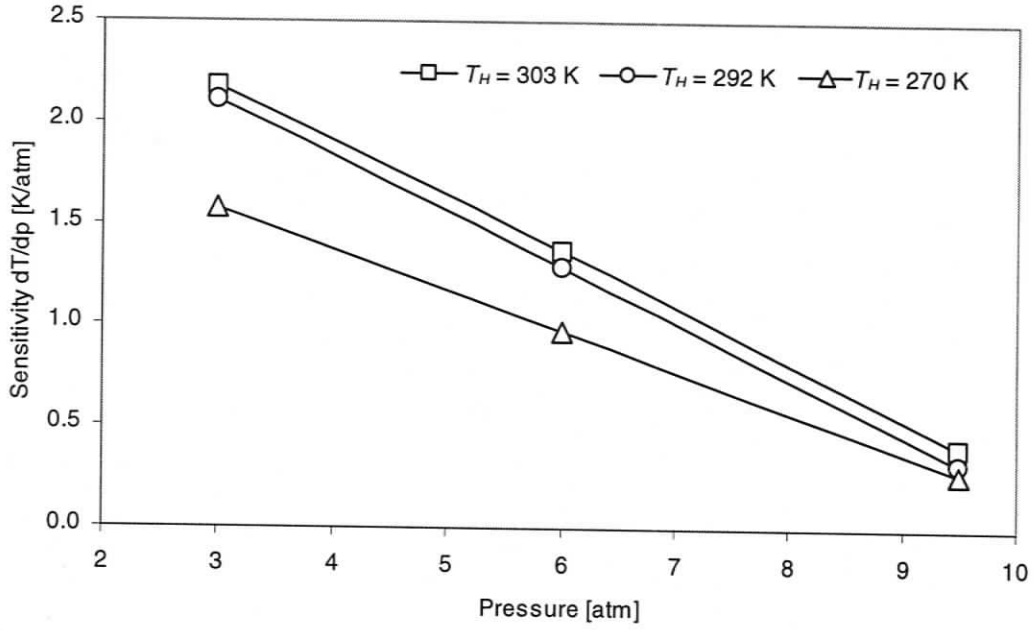

Figure 5-5. Gd AMR temperature span sensitivity to pressure as function of operating pressure.

Figure 5-5 shows that the regenerator dT_{span}/dp decreases almost linearly to ~ 0.5 K/atm when operating at 9.5 atm. This finding suggests that, with helium as the heat transfer fluid and employing the current regenerator structure, increasing the operating pressure past 10 atm may not be beneficial, because viscous losses could overcome temperature span increase benefits. In addition, if the sensitivity trend does not change for $p > 10$ atm, Φ_{max} may be reached with a relatively small increase in pressure. Future work should address cooling power sensitivity as a function of pressure.

Frequency

Operating frequency has a large impact on AMR performance. Current experiments have shown that faster cycling speeds increase cooling power in the tested operating regimes resulting in larger temperature spans with no heat load. A larger temperature span is a consequence of a higher cooling power overcoming parasitic heat loads such as thermal diffusion due to the AMR temperature gradient. As with utilization, regenerator performance is not expected to be a monotonic function of frequency. Heat transfer fluid pressure drop and parasitic loads due to eddy currents increase with operating frequency, eventually limiting the benefit of using higher cycling rates. Figure 4-8 illustrates that pressure drop is an exponential function of frequency. Attempting to maximize utilization and frequency would substantially increase the pressure drop for the particle bed structure being used, dramatically reducing the efficiency of the device.

Figure 5-6 illustrates the frequency sensitivity as function of heat rejection temperature using data from a number of experiments performed at 0.65 Hz and 0.8 Hz. Tests showed a positive sensitivity ($dT/df > 0$) with values ranging between 5 and 35 K/Hz. The Gd AMR displayed a sensitivity ranging between 2.5 and 13 K/Hz with the larger value being associated with the hottest heat rejection temperature. Cooling power sensitivity to frequency should also be addressed further in future work.

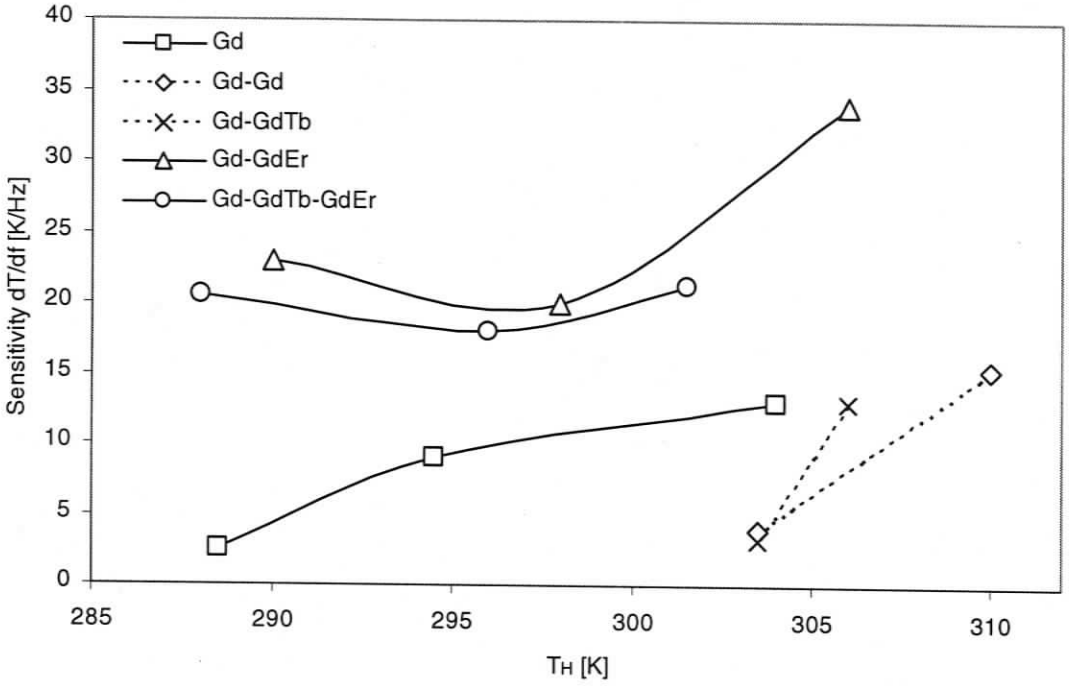

Figure 5-6. Temperature span sensitivity to frequency as function of T_H at 0.65 Hz.

The single puck AMR results can be summarized as follows:

a. Single puck AMR performance was characterized, where the characterization parameter was the temperature span. Single material AMRs produced temperature spans several times larger than their respective MCE.

b. The temperature span is highly sensitive to the heat rejection temperature and is maximized when T_H is 10 to 15 K above T_{Curie} for the no load case. T_{Hmax} was also found to vary with operational parameters change (utilization, frequency, and load).

c. Cooling power decreases and heat load sensitivity increases rapidly if $T_H >> T_{Curie}$. Experiments suggest that the best results in terms of temperature span,

heat load sensitivity and cooling power may be obtained if the heat rejection temperature is only few degrees hotter than T_{Curie}.

d. MCE alone is insufficient in predicting material performance: Gd, $Gd_{.74}Tb_{.26}$, and $Gd_{.85}Er_{.15}$ performed differently from what would be expected by only taking into account their respective MCE curves. Specific heat also plays a key role since it directly impacts the effective utilization.

e. Utilization has a large impact on performance. While current experimental data shows that Φ_{max} has not been reached yet, the sensitivity analysis results suggest that the AMRTA may be operating close to it.

f. Frequency has great impact on cooling power, and, indirectly, on temperature span. As with utilization, viscous losses are a major limitation to increasing operating frequency.

g. Future work should address frequency optimization and AMR geometry and matrix microstructure to reduce viscous losses.

Two Puck Regenerators

The Gd-Gd regenerator can be interpreted as a single high profile regenerator or as a cascade of two Gd regenerators (two pucks), where the heat rejection temperature for the cooler one is the interface temperature. Figure 5-1 shows that, compared to single puck regenerators, much larger temperature spans could be obtained with two pucks. Indeed, the Gd-Gd AMR attained 1.5 times the single puck Gd temperature span. However, heat load sensitivity also increased as can be seen in Figure 5-3. Furthermore, the cooling power increased because of the larger temperature span. It seems plausible that the larger temperature span is not just a result of the increased mass of the regenerator, but also of its aspect ratio. Because of the larger temperature spans the extreme regions of the regenerator operate with reduced cooling capacity being further away from T_{Curie}. Thus, a larger heat load sensitivity is observed in comparison to the Gd AMR. Although not investigated here, the comparison between Gd and Gd-Gd AMRs suggests it may be beneficial to study AMRs with equivalent masses, but different aspect ratios. Longer AMRs are promising for large temperature spans because they offer low demagnetization effects [14] and low losses due to thermal diffusion (longer

thermal path). On the other hand, lower aspect ratio AMRs have lower pressure drop, and smaller cylindrical wall surface areas, which, combined with a smaller temperature span, favor lower heat leaks. In addition they may perform with lower load sensitivity.

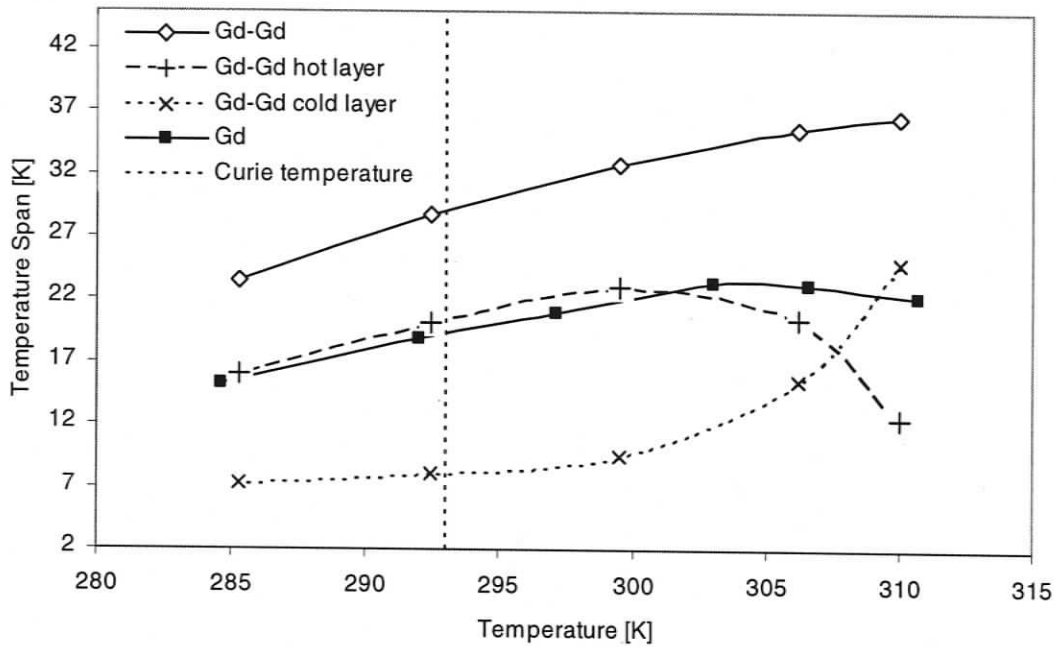

Figure 5-7. Gd-Gd and Gd temperature span vs T_H.

Figure 5-7 compares the no-load temperature spans of the Gd and Gd-Gd AMRs. For the latter case, measurements of the interface temperature allow the spans of the individual pucks to be plotted. T_{Hmax} was found to be even higher for Gd-Gd, a least 20 K above T_{Curie}; however, the load sensitivity is higher (Figure 5-3 shows the results for T_H = 309 K). For T_H > 310 K the temperature span is unstable. Furthermore, the hot layer temperature span decreases more rapidly for heat rejection temperatures higher than 300 K. Even if the overall trend of the hot layer is similar to the single puck AMR, the performance is substantially different.

Figure 5-8 shows temperature span sensitivity to pressure for the Gd, Gd-Gd, and Gd-$Gd_{.74}Tb_{.26}$-$Gd_{.85}Er_{.15}$ AMRs. Compared to the Gd AMR, multiple puck regenerators display a larger sensitivity at low pressure, but converge to similar values (~0.5 K/atm) when operating around 9.5 atm. In addition, temperature span sensitivity to operating frequency was found to be in the same order of magnitude for both Gd and Gd-Gd as can be seen in Figure 5-6.

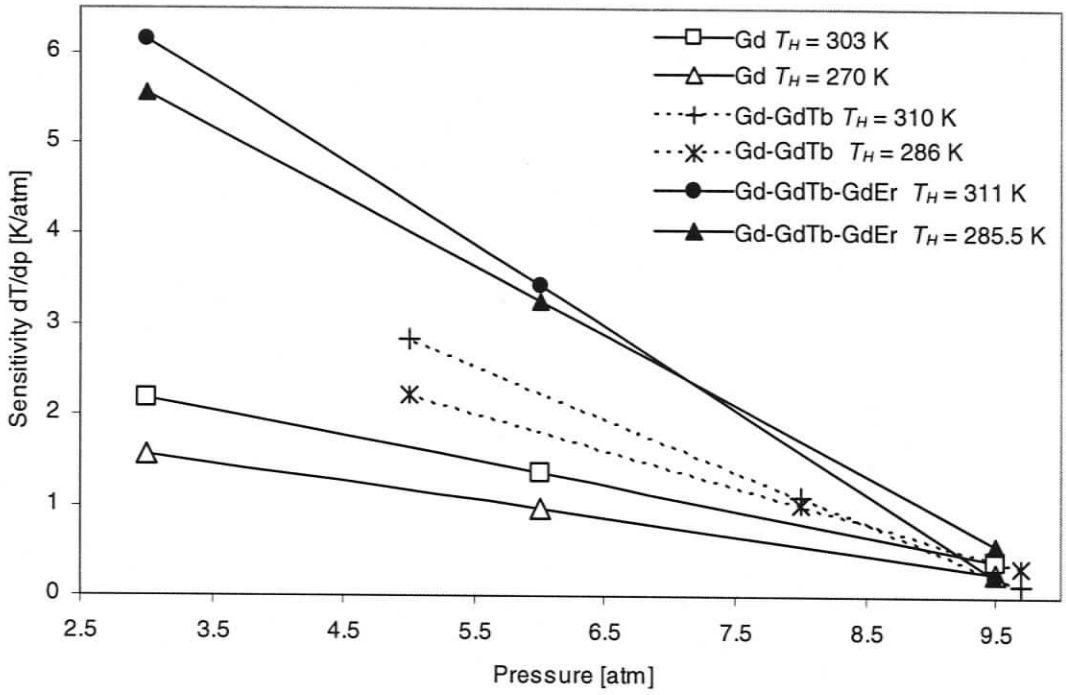

Figure 5-8. Temperature span sensitivity to pressure as a function of operating pressure for the Gd, Gd-Gd, and Gd-$Gd_{.74}Tb_{.26}$-$Gd_{.85}Er_{.15}$ AMRs.

Replacing the colder Gd puck with a $Gd_{.74}Tb_{.26}$ puck should increase cooling power since the $Gd_{.74}Tb_{.26}$ Curie temperature is in the neighborhood of 278 K. Figure 5-9 displays the no load tests for Gd, Gd-Gd, and $Gd_{.74}Tb_{.26}$ for a range of heat rejection temperatures. As already reported in the previous chapter, Gd-$Gd_{.74}Tb_{.26}$ performed better than Gd-Gd. The improvement is substantial given that, for single puck tests, $Gd_{.74}Tb_{.26}$ performed significantly worse than Gd, (Figure 4-5). In addition T_{Hmax} was obtained for a heat rejection temperature at least 4 K colder. This may be due to the lower T_{Curie} of the $Gd_{.74}Tb_{.26}$ layer, causing the average MCE to maximize for a lower T_H. Figure 5-9 shows that the warm layer, the Gd puck, deviates from the single Gd performance even more than for the Gd-Gd case, with a sharp drop past T_H > 306 K. The $Gd_{.74}Tb_{.26}$ puck also operated quite differently, as Figure 5-10 shows, with a decreased span for T_H < 285 K. However, it displayed a surprisingly high temperature span for values of T_H larger than 290 K.

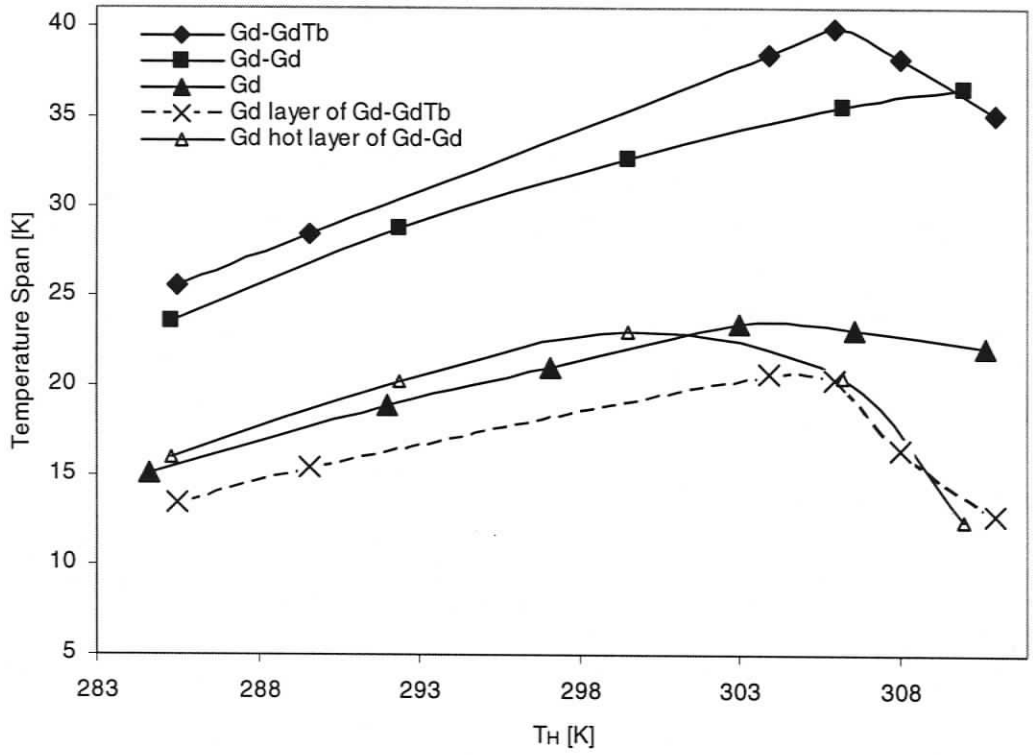

Figure 5-9. Gd-Gd, $Gd_{.74}Tb_{.26}$, and Gd temperature span vs T_H.

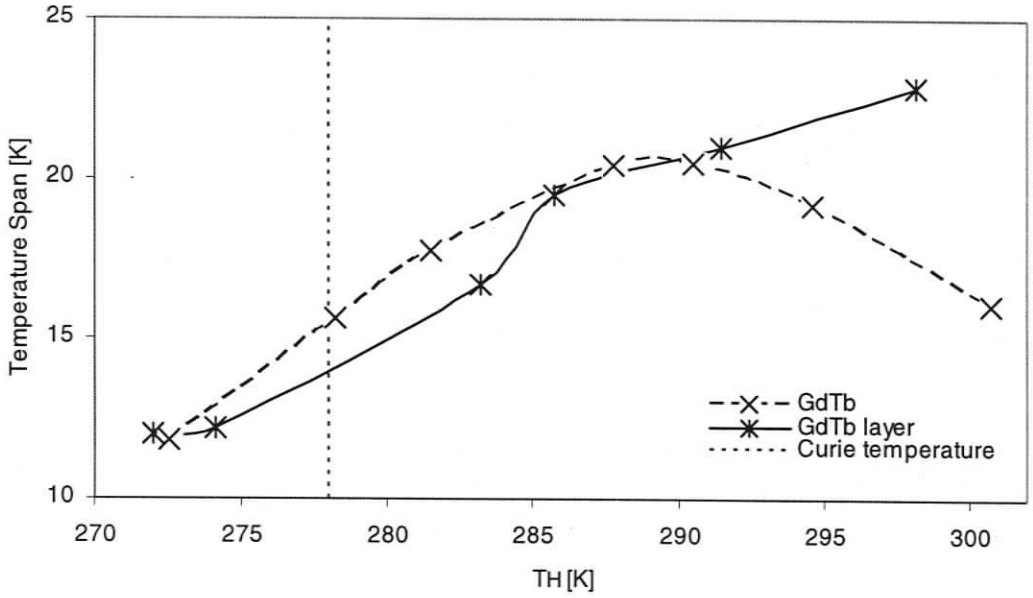

Figure 5-10. $Gd_{.74}Tb_{.26}$ AMR and $Gd_{.74}Tb_{.26}$ temperature span bottom layer versus T_H and $T_{interface}$ respectively.

In terms of temperature span sensitivity to heat load, the Gd-$Gd_{.74}Tb_{.26}$ AMR performed best among all the multi-material regenerators as shown in Figure 5-3. The regenerator also displayed a similar sensitivity to frequency compared to the Gd and Gd-Gd AMRs (Figure 5-6).

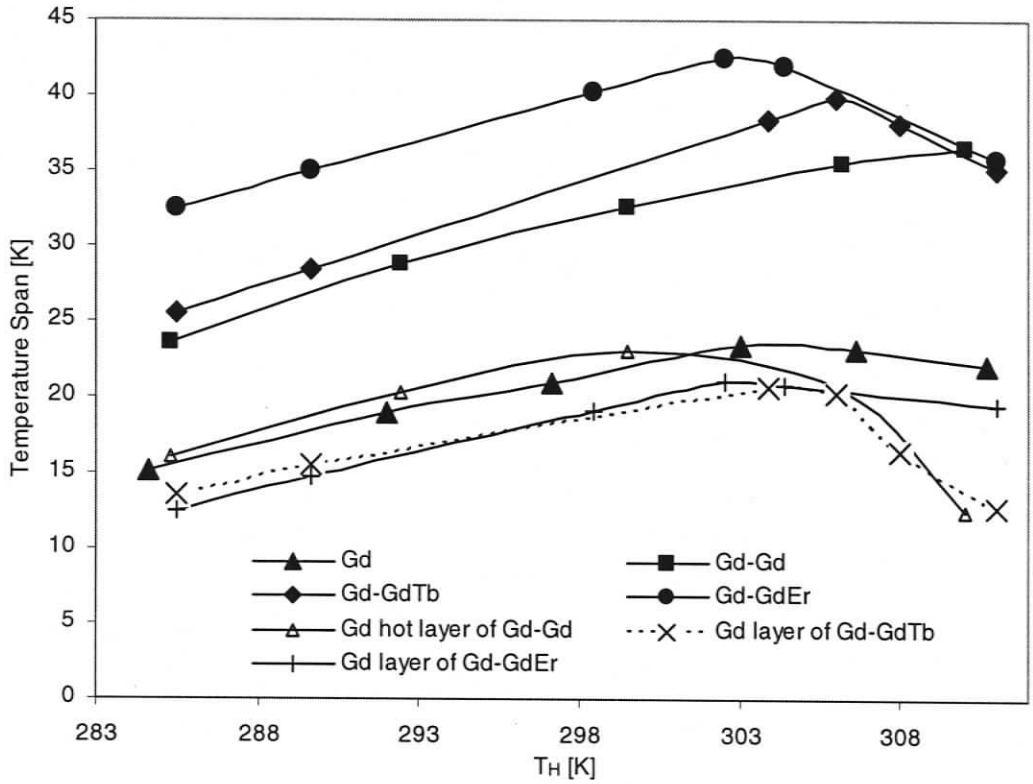

Figure 5-11. Gd-Gd, $Gd_{.74}Tb_{.26}$, Gd-$Gd_{.85}Er_{.15}$, and Gd temperature spans vs T_H.

The $Gd_{.85}Er_{.15}$ AMR displayed a surprisingly large temperature span when no load was applied, and so, combining it with a layer of gadolinium was expected to produce good results. Indeed, as is shown in Figure 5-11, this setup produced the largest temperature span among the two-layer regenerator configurations. The $Gd_{.85}Er_{.15}$ Curie temperature is estimated to be approximately 260 K and T_{Hmax} was found to be lower for the Gd-$Gd_{.85}Er_{.15}$ AMR (302.5 K) as compared to either the Gd-Gd or Gd-$Gd_{.74}Tb_{.26}$ AMRs. The temperature span pattern of the Gd layer is remarkably similar to that of the Gd AMR. However, it is approximately 14 % lower throughout the 285-310 K heat rejection range (Figure 5-11). Figure 5-12 illustrates the difference in performance between the $Gd_{.85}Er_{.15}$ AMR, and the $Gd_{.85}Er_{.15}$ bottom layer. When coupled with the Gd puck, the $Gd_{.85}Er_{.15}$ showed a reduced span for all heat rejection temperatures. This could be caused by the thermodynamic discontinuity at the interface between the two pucks as

will be discussed in the following section. The trend lines suggest that, when $T_{interface}$ is approaching the Curie temperature, the layer temperature span does not decrease as quickly as it does when operating as a single puck. Observations of the layered results seem to support the concept that multi-layering can be beneficial.

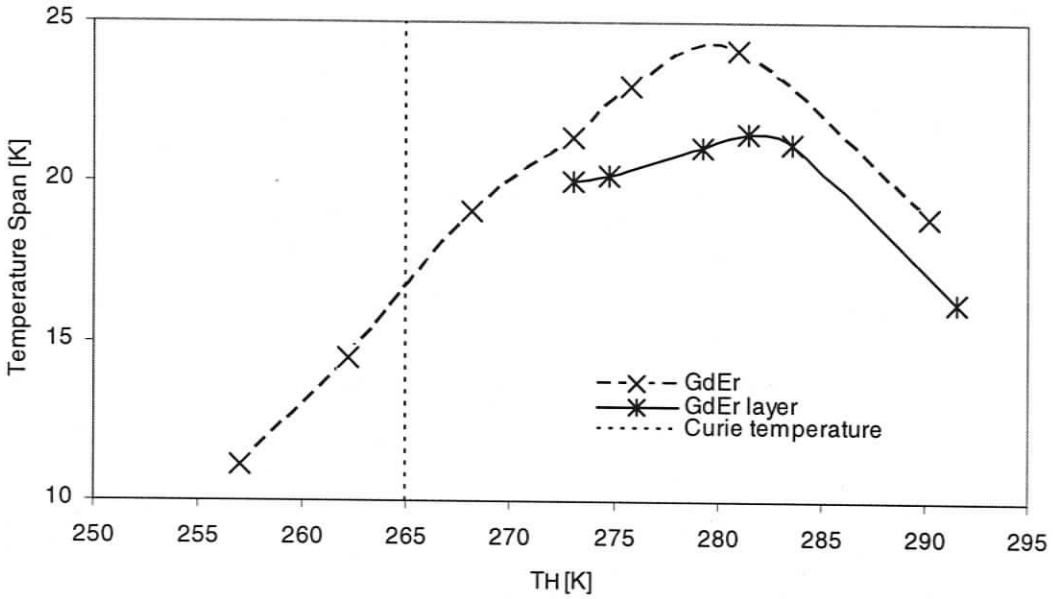

Figure 5-12. $Gd_{.85}Er_{.15}$ AMR, and $Gd_{.85}Er_{.15}$ cold layer temperature span vs T_H and $T_{interface}$ respectively.

Temperature span to heat load sensitivity was the largest for the two puck AMRs (Figure 5-3) for the range of heat rejection temperature tested. This may be a consequence of a large difference between Gd and $Gd_{.85}Er_{.15}$ Curie temperatures. The regenerator temperature span also displayed a large sensitivity to frequency (Figure 5-6), when compared to all other AMRs.

Synthesis of the heat load data leads to the following conjecture. A multi-material AMR may display lower sensitivity to moderate loading as compared to a single material AMR with a similar configuration (i.e. same regenerator mass, aspect ratio, and operating parameters). This behavior arises because, in contrast to a single material AMR, increasing temperature span when T_H is fixed does not necessarily mean a decrease in MCE as T_C decreases.

The following points summarize what was learned from the two layer AMR experiments:

a. Two puck regenerators create larger temperature spans than single puck AMRs.

b. For single material AMRs, sensitivity to heat load increases with temperature span. Larger temperature spans imply that the AMR is operating further away from T_{Curie}.

c. AMR mass and aspect ratio have a large impact on performance and efficiency. Further work is required in order to study the effects of varying AMR aspect ratio with fixed mass and particle geometry.

d. When compared to a single puck AMR, the maximum no-load temperature span is obtained at higher heat rejection temperature. However heat load sensitivity increases significantly when $T_H >> T_{Curie}$.

e. Material layering was implemented to overcome the issue of small cooling power contribution from the colder sections of the AMR. Larger temperature spans were obtained with the use of appropriate alloys and operating conditions.

f. Multi-material AMRs may have a greater cooling capacity than single material AMRs, over a limited range of temperature spans. If heat loads or other parameters drive the temperature of a material away from its Curie point, the AMR performance is expected to decrease.

Three Puck Regenerator

Figure 5-13 compares the no-load temperature spans obtained by the Gd, Gd-Gd, Gd-$Gd_{.74}Tb_{.26}$, and Gd-$Gd_{.85}Er_{.15}$, AMRs to those obtained using a three layer AMR composed of Gd-$Gd_{.74}Tb_{.26}$-$Gd_{.85}Er_{.15}$. Figure 5-14 shows the temperature spans of the pucks when used both as individual AMRs and as part of the three layer regenerator. The temperature spans are reduced for all of the pucks in the three layer configuration, and the maximum temperature span for each layer is obtained at a much cooler temperatures (i.e. all curves show a shift towards the left of the graph). The puck most affected in terms of temperature span is Gd, while the one with greatest temperature shift is $Gd_{.74}Tb_{.26}$. Finally, the small gain in temperature span obtained by the three layer regenerator compared to the Gd-$Gd_{.85}Er_{.15}$ AMR suggests that further improvements are possible by optimizing the layer geometries and materials used.

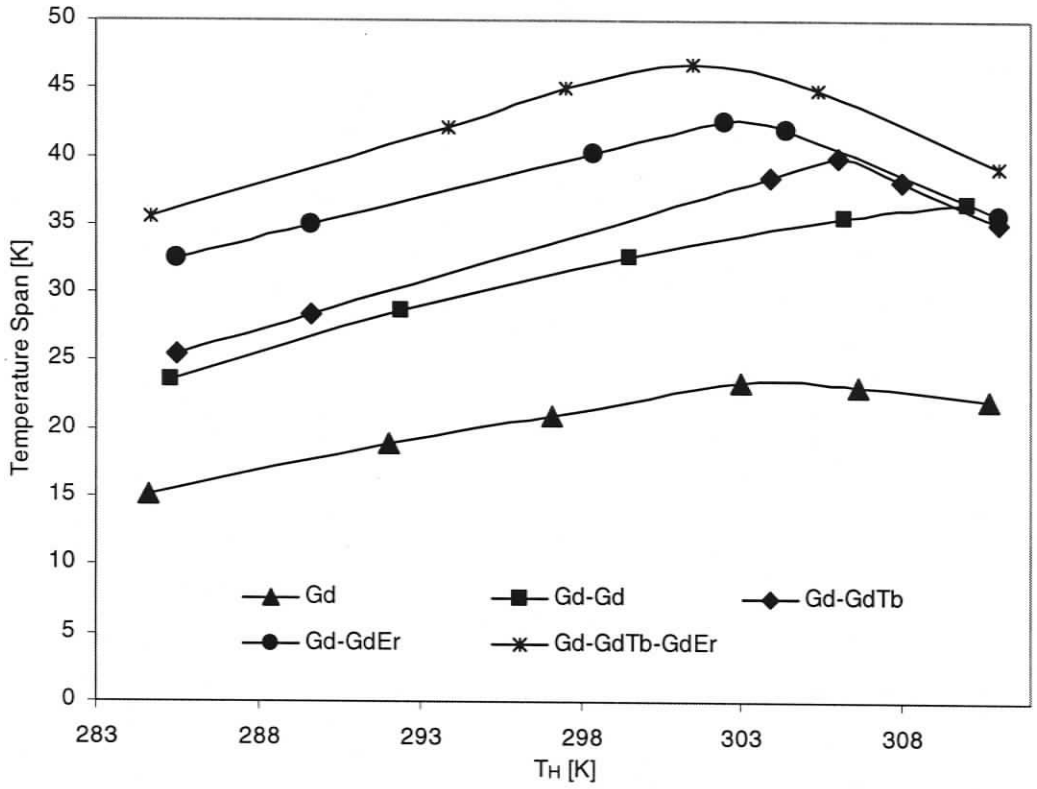

Figure 5-13. Gd, Gd-Gd, Gd-$Gd_{.74}Tb_{.26}$, Gd-$Gd_{.85}Er_{.15}$, and Gd-$Gd_{.74}Tb_{.26}$-$Gd_{.85}Er_{.15}$ AMR temperature span results.

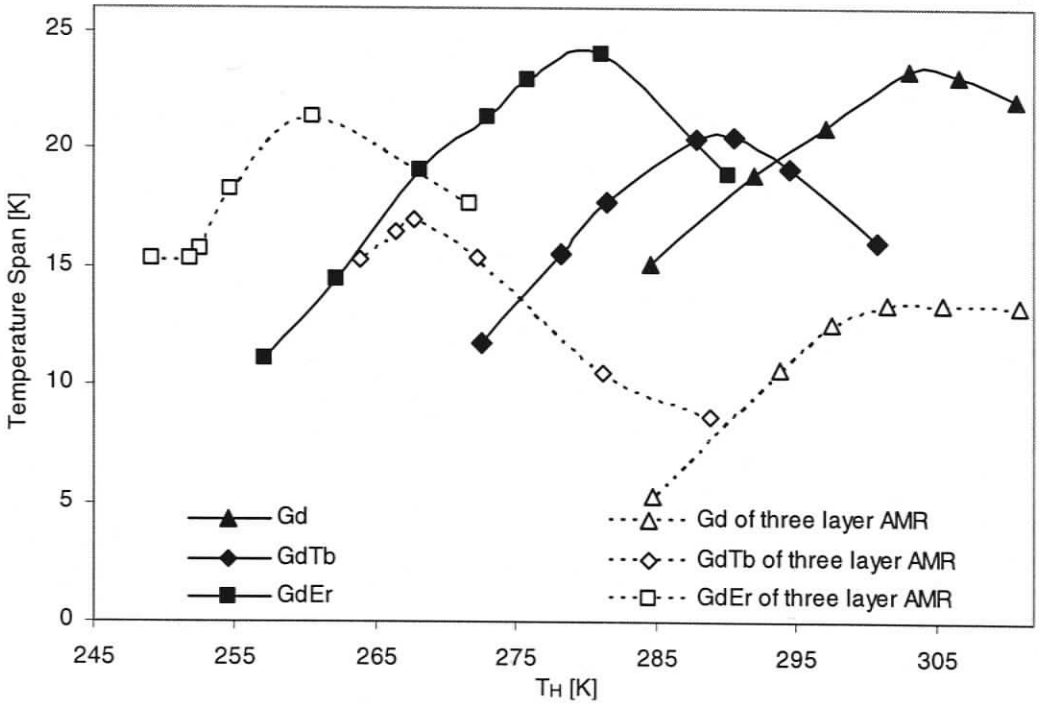

Figure 5-14. Temperature spans of the pucks when used as individual AMRs and as part of the three layer regenerator.

The three layer AMR displayed large sensitivities to all of the operating parameters. Both the frequency and the heat load sensitivity were found to be similar to the Gd-$Gd_{.85}Er_{.15}$ regenerator. Figure 5-15 shows that the heat load curves of Gd-$Gd_{.85}Er_{.15}$ and Gd-$Gd_{.74}Tb_{.26}$-$Gd_{.85}Er_{.15}$ are similar up to an applied load of 8 W.

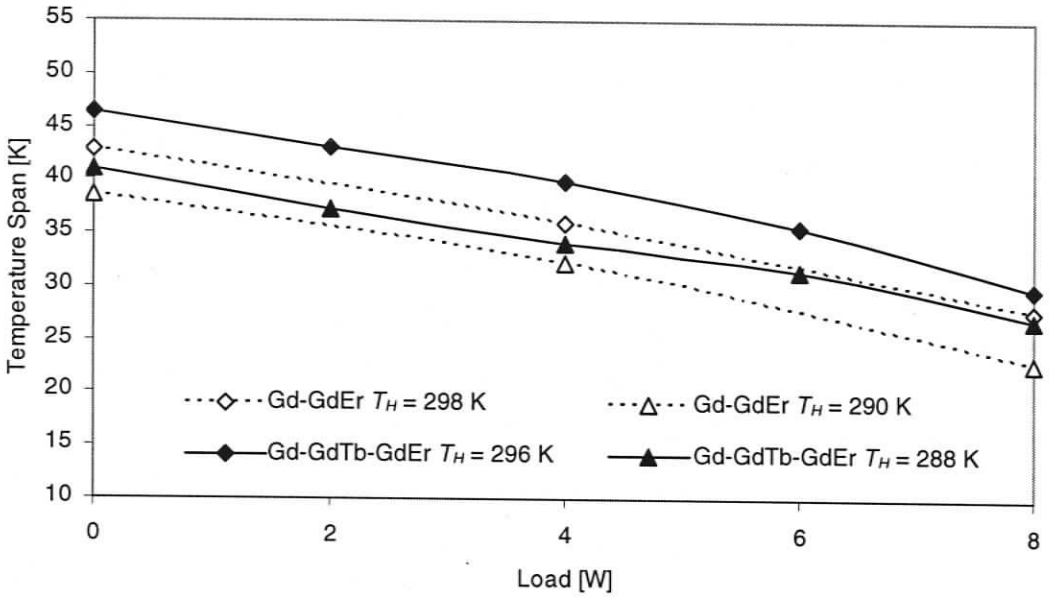

Figure 5-15. Temperature spans of Gd-$Gd_{.85}Er_{.15}$ and Gd- $Gd_{.74}Tb_{.26}$-$Gd_{.85}Er_{.15}$ as a function of applied load.

5.2 Predicting Layered AMR Performance

Once the single layer experiments were completed and no load temperature spans characterized, multi-material multi-layer AMRs were created using the single pucks. Some of the objectives of these tests were to characterize layered AMR performance and how layers interact. In addition an interesting question is whether single puck data can be used to predict performance when single pucks are combined into a multi-puck, layered AMR. In the previous section it was suggested that the thermodynamic discontinuities between the layers may cause performance losses. Magnetic interactions also affect how an AMR operates, perhaps enhancing magnetization and, therefore, performance [14].

Comparing the experimental results to a simple additive prediction based on the individual layer data is discussed in this section. Predicted temperature spans for multi-material AMRs are calculated as follows. Each of the curves represented in Figure 4-5 is fit by a polynomial. Then, given a specific T_H, the Gd polynomial is used to calculate

the temperature span of the top layer. Subtracting the temperature span from T_H the interface temperature is obtained. Finally, the interface temperature is used for the cold layer polynomial to predict its temperature span. The overall temperature span results from the sum of the contribution of each layer.

Figure 5-16 compares experimental data of the two layer Gd-Gd regenerator to the predicted performance based on Gd AMR data. The lines with markers show experimental results for the temperature span of the AMR and its individual layers, while the remaining lines represent the predicted behavior. In general, the calculated trend is in good agreement for T_H values below 298 K, diverging for higher values of T_H. For

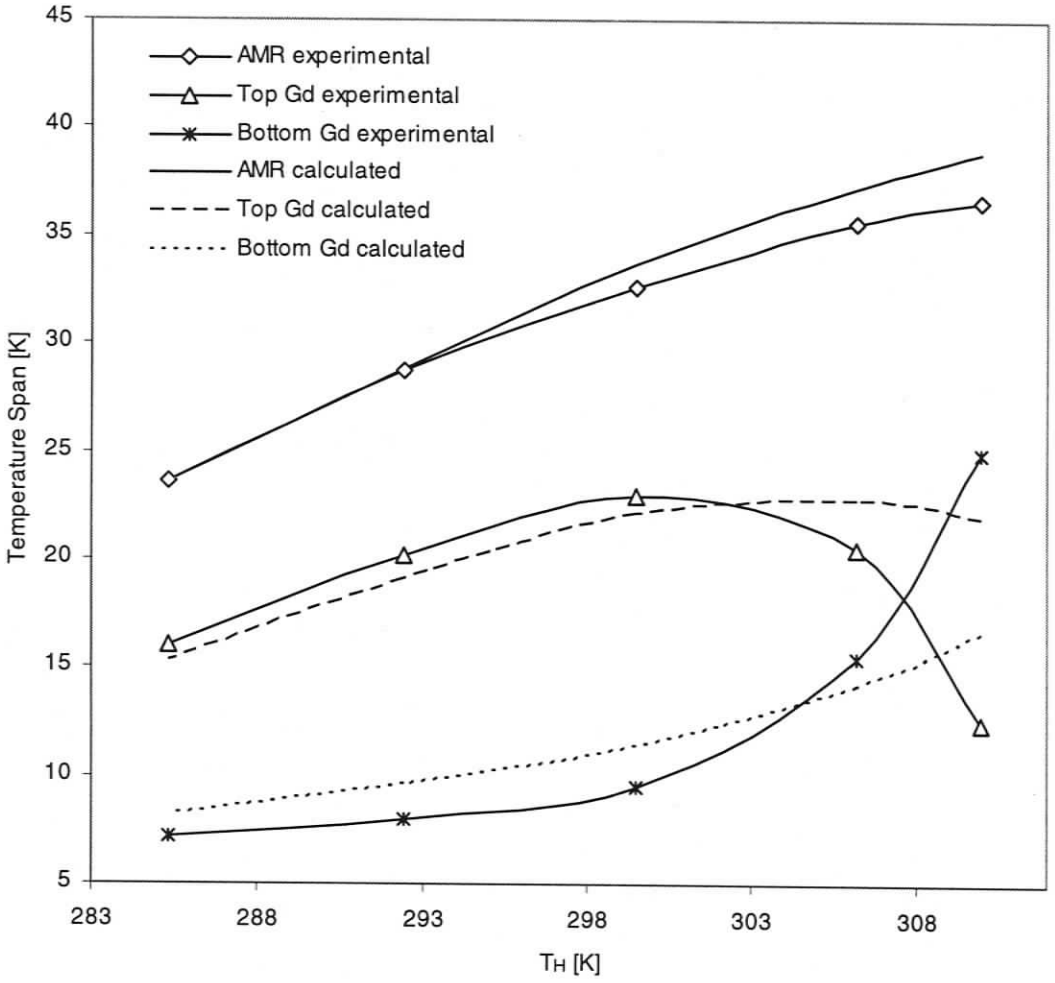

Figure 5-16. Gd-Gd layered AMR temperature span vs T_H compared to predicted from single puck data.

T_H > 300 K the hot layer temperature span decreases at a much faster rate than that which is predicted. In fact, a value of only 12.5 K at 310 K is found experimentally compared to the calculated 22 K. Conversely, the cold layer span increases at a faster rate, with a value of 25 K at 310 K compared to the calculated 17.5 K. Two factors could be the cause of such behavior: the thermo-magnetic interactions between the two layers, and a different amount of heat leak loading. In this case, gadolinium is used for both layers and there is no discontinuity in the material properties at the interface between the pucks.

Figure 5-17 illustrates the individual layer temperature spans versus the layer relative heat rejection temperature, T_{Hrel}. In other words the hot layer curve is plotted against the absolute heat rejection temperature, T_H, while the cold layer is plotted against its heat rejection temperature, the interface temperature. The figure illustrates that the top and the bottom regenerators do not behave identically when operating with the same T_{Hrel}. The colder layer under-performs when the heat rejection temperature is below the Curie temperature, and vice versa for $T_{Hrel} > T_{Curie}$. Alternatively the hot layer over-performs for $T_{Hrel} < T_{Curie}$, while its temperature span drops off more quickly than expected at higher temperatures.

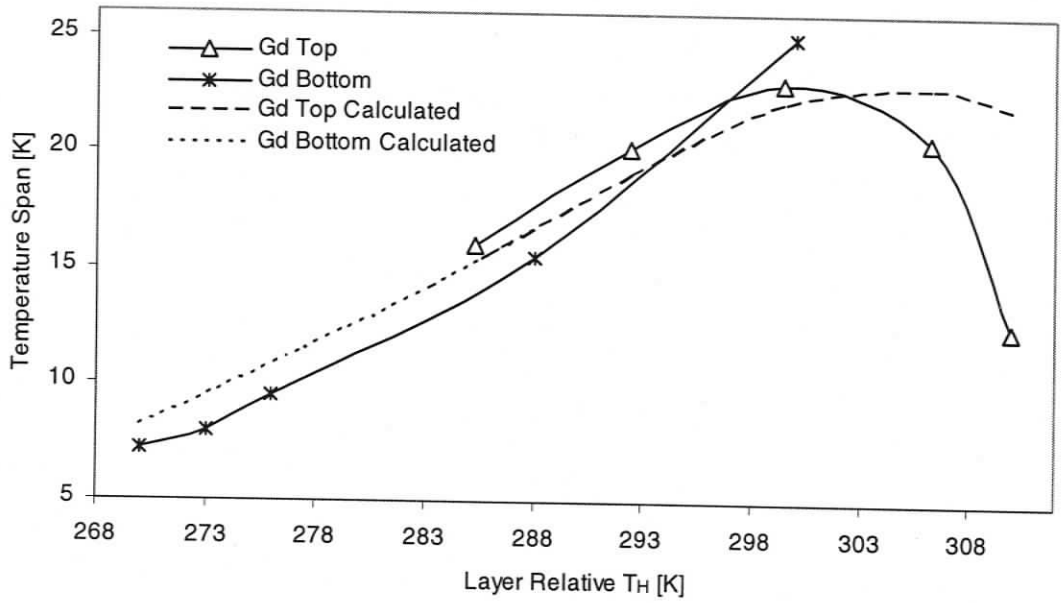

Figure 5-17. Layer temperature span vs T_{Hrel} for the Gd-Gd layered AMR.

Figure 5-18 compares experimental data for a two layer Gd-$Gd_{.74}Tb_{.26}$ regenerator to the predicted performance. The operating parameters are the same as the previous case. The prediction is in good agreement for T_H < 304 K, although the slope is higher

for the calculated case. For T_H > 305 K, the hot layer temperature span decreases at a much faster rate than the predicted case, with a value of only 12.8 K at 310 K compared to the calculated 22 K. Conversely, the cold layer increases at a faster rate, with a value of 23 K at 310 K compared to the calculated 20.5 K. Overall, the predicted $Gd_{.74}Tb_{.26}$ layer performance is in a good agreement with the experimental data, while the Gd layer performance was overestimated with an offset of over 2 K in the almost linear region (T_H < 304 K) and was found to diverge even more quickly for higher temperatures. Interestingly, both Gd-Gd and Gd-$Gd_{.74}Tb_{.26}$ showed similar behavior when operating with a high heat rejection temperature. In both cases the hot layer remarkably underperformed, while the colder one greatly over-performed. It can be concluded that individual pucks perform differently in multi-layer regenerators when compared to when they are operating independently.

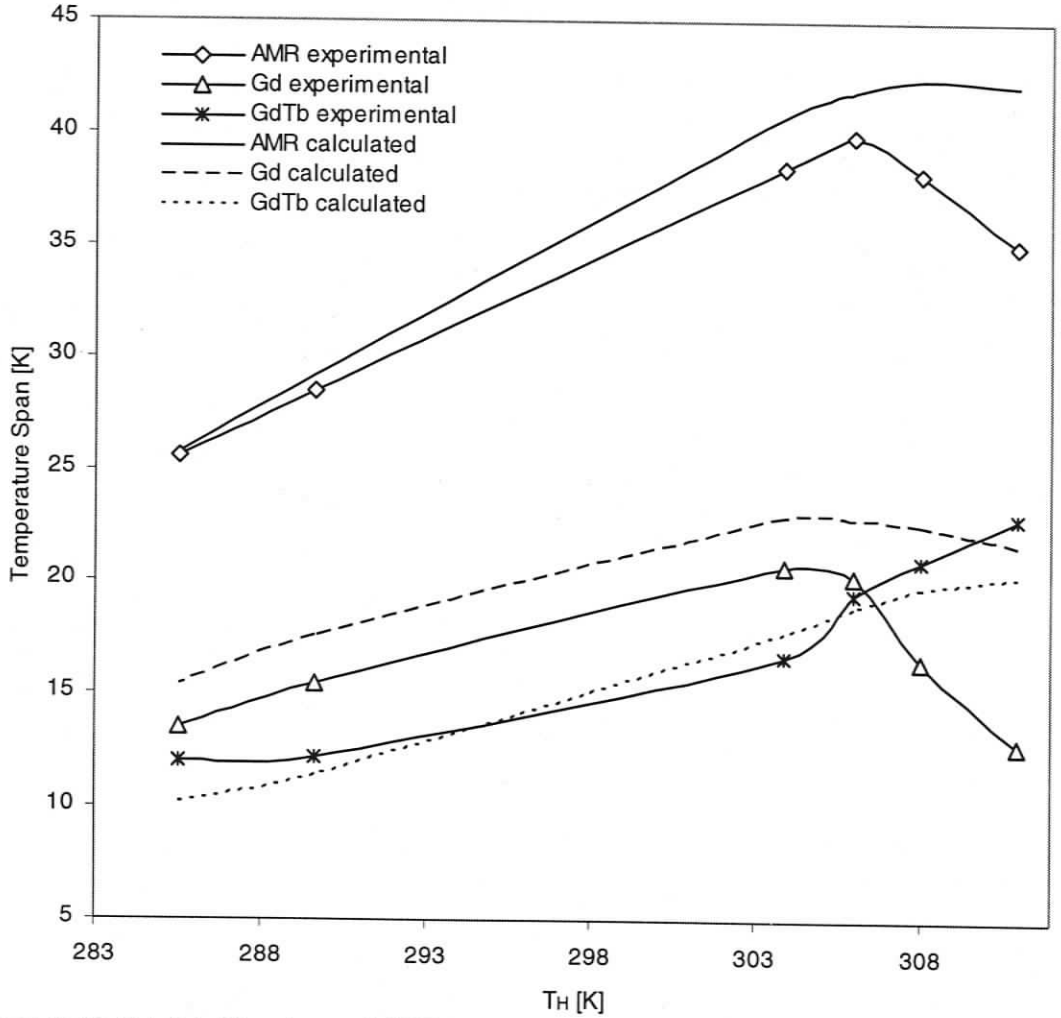

Figure 5-18. Gd-$Gd_{.74}Tb_{.26}$ layered AMR temperature span data compared to that predicted from single puck data.

Figure 5-19 compares the experimental data for a two layer Gd-$Gd_{.85}Er_{.15}$ regenerator to the predicted performance. For this case, the prediction is in good agreement with the experimental data in terms of the individual layer contributions; however, the absolute temperature span is considerably overestimated.

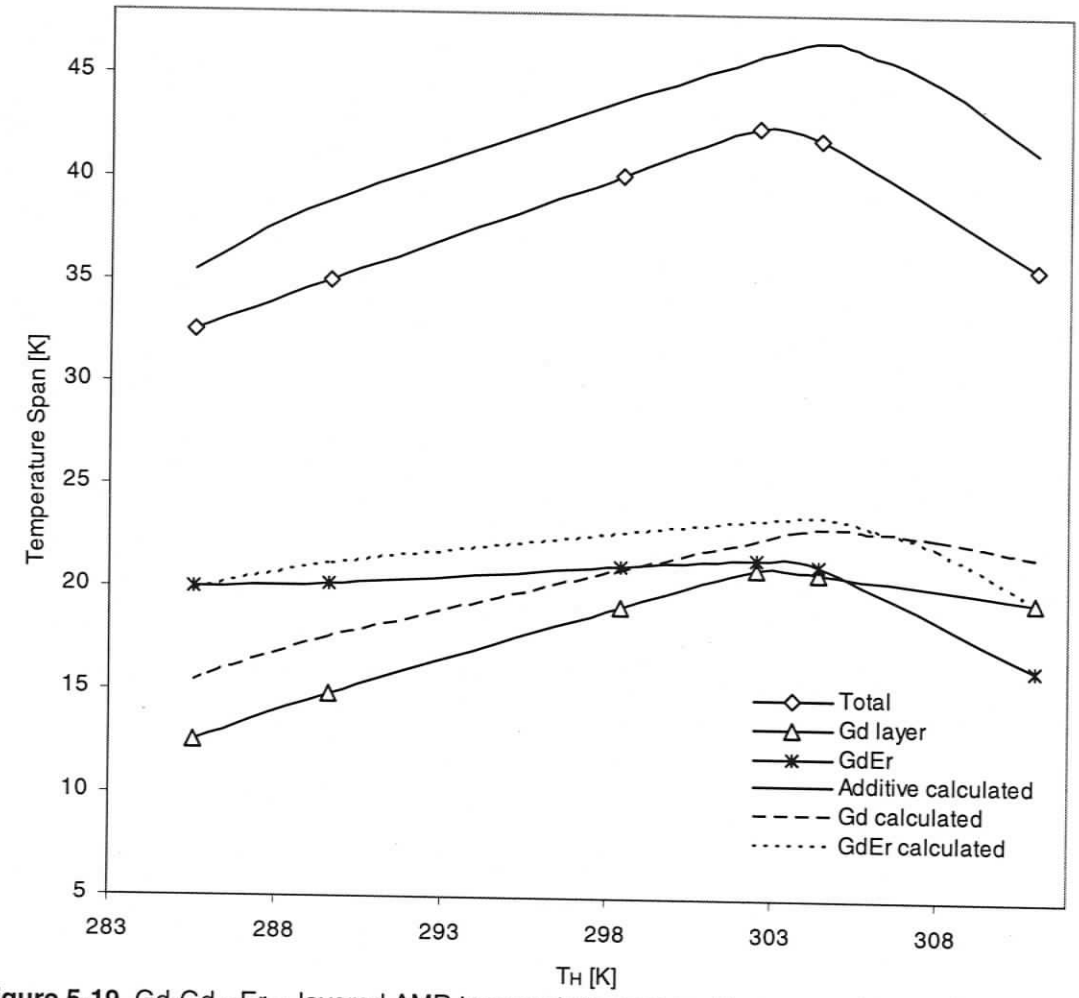

Figure 5-19. Gd-$Gd_{.85}Er_{.15}$ layered AMR temperature span vs T_H compared to predicted from single puck data.

Specific Heat Discontinuity Considerations

As discussed previously, the thermodynamic properties of the materials being tested vary substantially near their Curie temperature. The following qualitative analysis illustrates the specific heat discontinuity at the interface between two different materials. Figure 5-20 shows the temperature and specific heat profile for Gd-$Gd_{.74}Tb_{.26}$ with T_H = 304 K. The x axis is the nondimensionalized position along the regenerator, where the hot-end is at x = 0, the cold-end at x = 1, and the interface between the two pucks at

x = 0.5. The dashed lines represent the demagnetized scenario, while the continuous ones the magnetized case. The demagnetized temperature profile is obtained from experimental T_H, T_{cold}, and $T_{interface}$ data, at 9.5 atm and 0.65 Hz and assuming a linear fit between temperatures. In addition, it is assumed that the regenerator and helium temperatures are coincident. Using the assumed temperature profile and material specific heat data (see Figure 2-3 and Figure 2-4), the temperature in the magnetized state, and the low and high field specific heat are shown. As can be seen, there is a strong variation in the bed specific heat, C_B throughout the AMR. When layering two alloys with Curie temperatures that are further apart (Gd-$Gd_{.85}Er_{.15}$ for instance), the discontinuity at the interface may even be more profound.

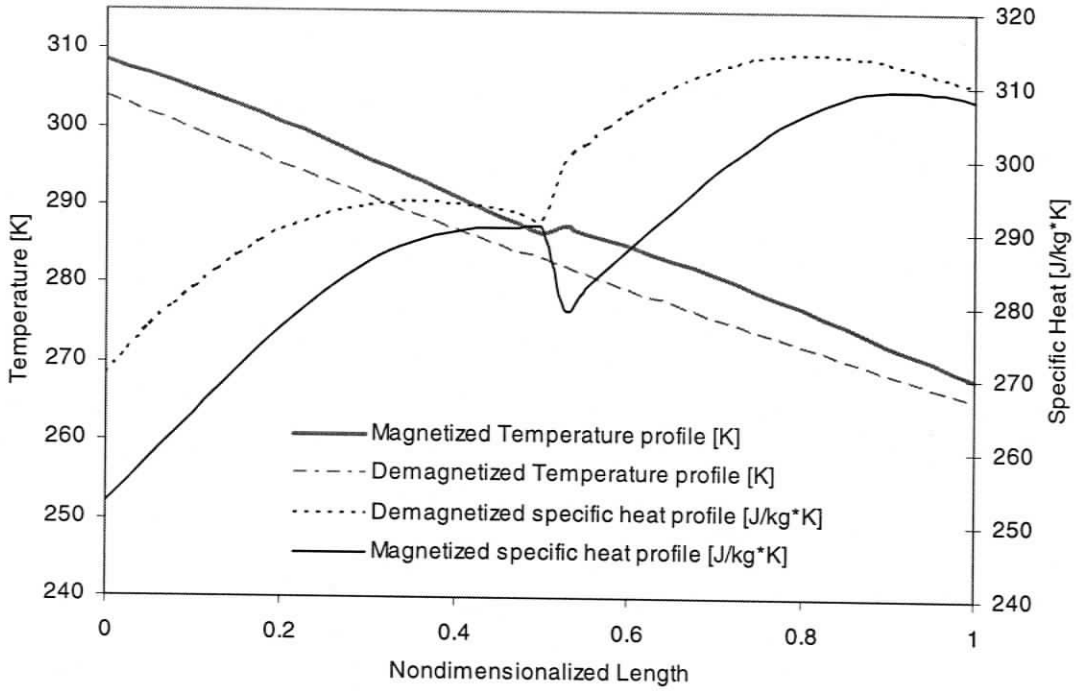

Figure 5-20. Temperature and specific heat profile for Gd-$Gd_{.74}Tb_{.26}$ with T_H = 304 K.

To summarize, using single puck AMR results to predict layered performance revealed the following:

a. The method highlights the interaction between layers and shows that at higher temperatures the layers influence each other even more strongly.

b. The method was somewhat accurate in reproducing the performance of the Gd-Gd and Gd-$Gd_{.74}TB_{.26}$ AMRs for heat rejection temperatures below T_{Curie} of the warmer layer. The inability to accurately estimate the real temperature

spans for high T_H conditions is likely a result of the low cooling power when operating in this region (this suggests that these operating regimes should be avoided in commercial refrigeration devices).

c. Even if the method substantially overestimated the Gd-$Gd_{.85}Er_{.15}$ temperature spans, it was qualitatively accurate in reproducing the overall trend.

5.3 Heat Leaks

As discussed earlier, at temperatures above the Curie point of a material, the temperature span developed by an AMR is very sensitive to heat load. Thus, monitoring, quantifying, and minimizing heat leaks are a continuous challenge when operating the AMRTA. If inconsistent and unreliable data has been collected, heat leaks are almost always the cause.

The main parasitic loads are caused by the friction of the cylinder bearings sliding on the tracks and by the eddy-currents generated in the moving metal parts. The bearings are mounted on G-10 pads epoxy bonded on the cylinder at the same position of the regenerators (Figure 3-9). Such design is optimal for the mechanical loading of the cylinder during operation, but creates a short thermal path. Early experiments showed that operating the apparatus continuously for several hours would lead to inconsistent results. Allowing one day between tests proved to fix the problem. Such observations, in conjunction with high temperatures measured on the rail lead to the conclusion that bearing heating was a cause of the inconsistency.

For early experiments the temperature of the bearing and rail assembly at the start of the test was at room temperature, approximately 292 K. It soon became clear that in order to be consistent over a range of heat rejection temperatures (as broad as 40 K), pre-cooling or pre-heating the bearing and rail was necessary. Indeed, this preconditioning process allowed for the difference in temperature between the regenerator hot end and bearing to be maintained at a "reasonably constant" value throughout the full range of the experiments. The amount of pre-heating or cooling required was determined so that when steady state was reached the bearing temperature would be the same as T_H. The major difficulty with this procedure is in obtaining the desired final bearing temperature consistently when the apparatus reaches steady state. Different experiments typically produce different dynamic loads on the bearing, and might require a different length of time to reach steady state. Thus it

becomes difficult to estimate the correct amount of bearing preconditioning, and, often, tests need to be repeated because the initial guess was incorrect. Because of these difficulties a better way of observing the bearing temperature and estimating the parasitic heat load needed to be devised. To help monitor and understand bearing losses, a PRT was added inside the aluminum bearing support (Figure 3-8). In addition, a finite element model was developed to estimate the parasitic load and quantitatively establish a tolerable deviation from the desired final bearing temperature.

5.3.1 Finite Element Analysis (FEA)

An 3-D finite element model (thermal analysis) of the top end of the cylinder was generated with the objective of simulating the temperature distribution and the heat flux across the regenerator and cylinder walls for a specific experimental scenario: a Gd-$Gd_{.74}Tb_{.26}$-$Gd_{.85}Er_{.15}$ regenerator operating at 9.5 atm, T_H = 301.5 K, and 0.8 Hz.

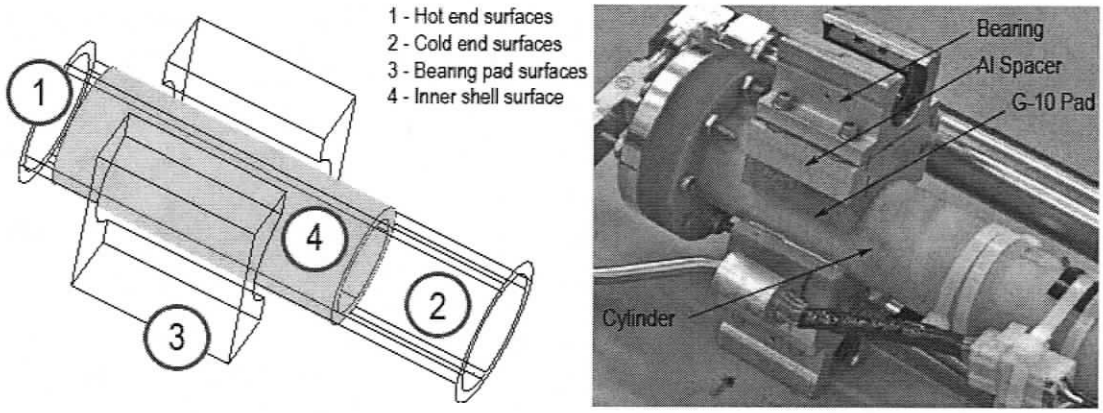

Figure 5-21. Cylinder top end picture and the 3-D model showing domains and boundary conditions.

Figure 5-21 illustrates the model, with the dark volume being the phenolic regenerator shell, and the transparent one the top end of the cylinder. The two volumes were set as two domains each with its own properties (G-10 for the cylinder, phenolic composite for the regenerator shell). G-10 thermal conductivity was set to be a function of temperature and was assumed to be isotropic. Contact thermal resistance between the shell and the cylinder was not taken into account. The numbered faces refer to the surface boundary conditions dictated by the experimental PRT data. *Surface 1* (hot end side) was set to 301.5 K, *surface 2* (cold end side) to 251.5 K, *surface 3* (bearing pad) to 300 K, and *surface 4* was given a temperature distribution along the *z* axis, obtained from the four

experimental temperatures given by the hot, cold and interface PRTs. The simulation was performed with different mesh resolutions to ensure that the results did not depend on the model discretization. For the conditions described above, the heat flux across the bearing pads was calculated to be 3.4 W. More simulations were performed assuming the same temperature distribution, but different bearing temperatures. The results are summarized in Table 5-1.

Table 5-1. Heat flux versus bearing temperature.

Bearing T (K)	*Heat flux (W)*
280.0	0.2
290.0	1.8
300.0	3.4
310.0	5.1
320.0	6.8

For the range of conditions simulated the parasitic heating due to bearing friction was found to be linearly proportional to the bearing temperature, with a proportionality constant of approximately 0.16 W/K. Also, only a very small heat flux was found for a bearing temperature of 280 K. Although the temperature span is expected to vary with the heat load, it is not taken into account in this simplified analysis. For instance if the bearing temperature is set to be at 280 K the regenerator develops a larger temperature span than if it was set at 300 K. Therefore heat leaks larger than 0.2 W are expected. Conversely with a bearing temperature of 320 K a smaller temperature span is developed, thus, a heat flux less than 6.8 W is expected. In conclusion a more accurate model is likely to show a smaller proportionality constant, or more likely a non linear relation. In addition, for a more comprehensive understanding, the model should be repeated for each type of experiment because both the domain and the boundary conditions can change dramatically from case to case. For these reasons the case with the largest expected heat leaks was modeled.

In order to estimate how the heat leak impacts the regenerator temperature span, it is necessary to know the temperature span to heat load sensitivity, which varies from experiment to experiment. For the above case, the sensitivity was experimentally found, in the range of interest, to be linear with a proportionality constant of approximately 1.8 K/W. Therefore, if the same experiment is performed twice, and the final steady state

bearing pad temperature in the second case is 10 K higher, it is expected to perform with a temperature span reduced by almost 3 K (10 K x 1.6 W/K = 1.6 W parasitic load. 1.6 W x 1.8 K/W = 2.9 K change in temperature span). Actual experiments with bearing final temperature deviating by 5 to 10 K resulted in a final temperature span departing 0.5 to 2 K from the expected value. It can be deduced that the experimental and numerical results are in good agreement. It is important to observe that the simulated experiment represented the worst case scenario compared to any of the other tests conducted so far. Thus, in general, smaller heat leaks and heat load sensitivity are expected with proportionality constant less than 0.16 W/K and 1.8 K/W respectively.

In conclusion, to ensure that heat leaks variation do not induce temperature span deviations larger than ±0.5 K, the final bearing pad temperature should not deviate by more than 2 K between experiments.

5.4 Initial conditions

The objective of this section is to determine if the final AMR steady state condition depends on the initial temperature distribution. If the steady state is insensitive to the initial conditions, then we can argue that the preconditioning currently carried out to offset heat leaks is not somehow facilitating the refrigeration process and therefore skewing the results.

Figure 5-22 illustrates the results of two experiments conducted on $Gd_{.85}Er_{.15}$ with T_H set at 290 K, helium pressure at 9.5 atm and operating frequency at 0.65 Hz. The two tests were conducted with different initial conditions:

Case one:

1. The chiller was set to 280 K (T_H).
2. The experiment was started and run for aprroximatively 750 seconds.
3. The chiller was set to 290 K.
4. The experiment was continued until steady state was reached.

Case two:

5. The rail was precooled to 282 K by setting the chiller temperature to 272 K.
6. The chiller was set to 290 K.
7. The experiment was carried out until steady state was reached.

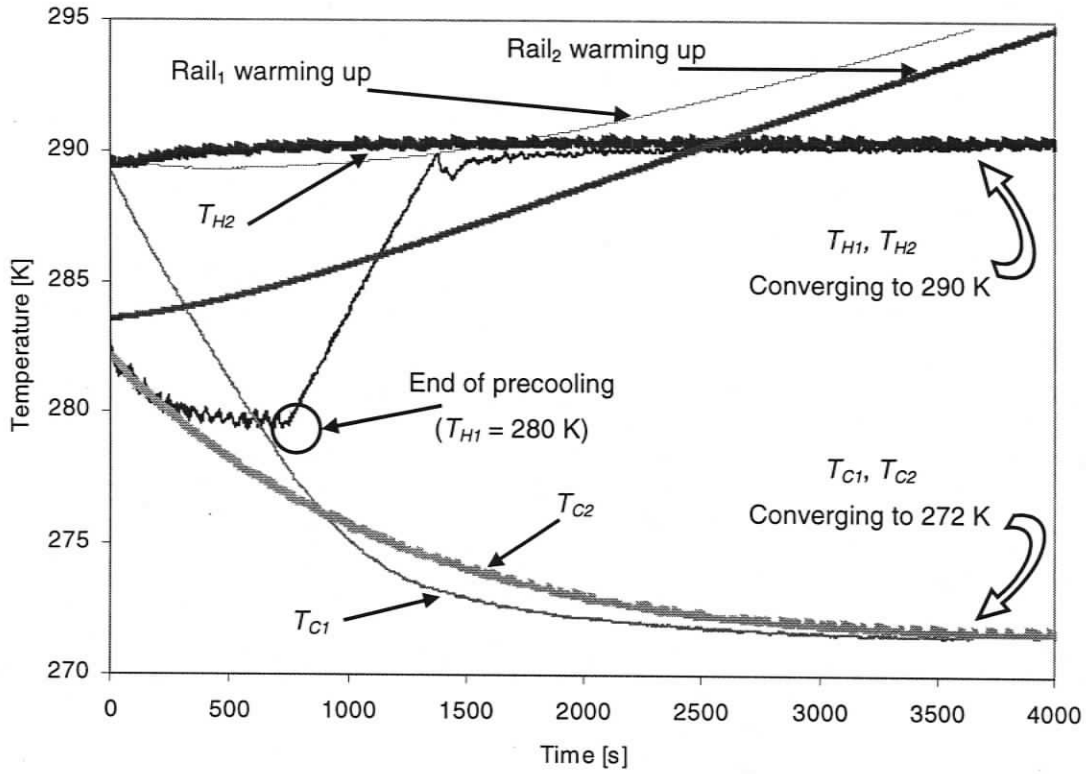

Figure 5-22. Regenerator and rail temperatures as a function of time for $Gd_{.85}Er_{.15}$ with T_H at 290 K, helium pressure at 9.5 atm, and frequency at 0.65 Hz with different initial conditions.

In Case 1 the first 750 seconds allowed the cold end of the regenerator to cool rapidly and the rail to maintain its temperature below 290 K. Changing the T_H to 290 K caused the regenerator to immediately gain 10 K temperature span on the hot side, while the cold-end gradually approached its steady state temperature of approximately 272 K. The rail temperature accelerated its warm up with a final temperature of 294 K.

Case 2 started with an 8 K temperature span caused by the rail precooling. The cold side reached steady state more gradually while the rail temperature climbed from 282 K steadily and more steeply than in the previous case. Overall case 2 took approximately 500 seconds longer than case 1 to reach steady state, and the final temperature of the rail was about the same (294 K). The final steady temperature span differed by only 0.1 K, a value within the measurement error.

Figure 5-23 shows a third case where T_H was held at 278 K for 1000 seconds and then changed to 290 K. The excessive hot-end precooling caused the cold end to reach a temperature below 272 K. The plot illustrates that the larger induced temperature span could not be sustained and the cold end warmed to the expected temperature of

272 K. However, because the process was taking a long time, the rail caused excessive thermal load, and as a result the final temperature span obtained was not as large as in the previous two cases.

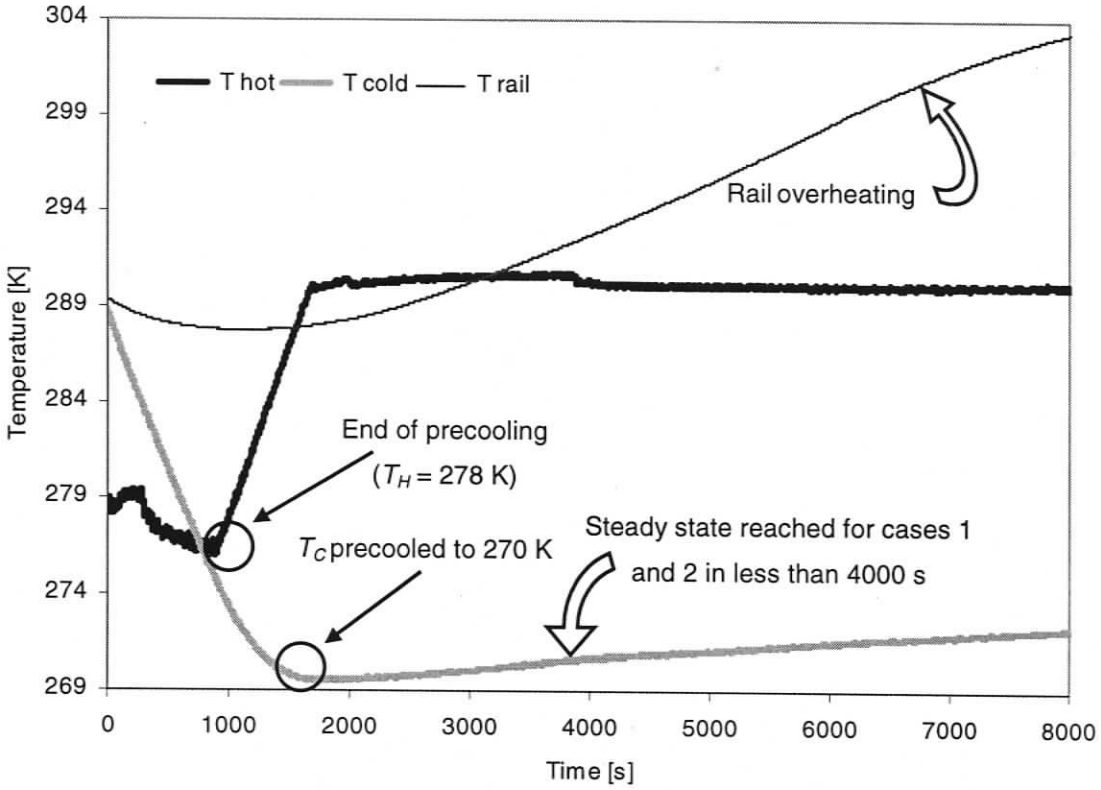

Figure 5-23. Regenerator and rail temperatures as a function of time for $Gd_{.85}Er_{.15}$ with hot end precooling at 278 K for 1000 seconds.

It can be concluded that the initial regenerator temperature distribution does not affect the final steady state for the range of AMRs and temperatures tested. On the other hand, the initial rail temperature, which is an indication of the system thermal loading, is an important parameter. This result is of great importance for several reasons. As long as the thermal loading is controlled, no particular care needs to be paid to the initial temperature distribution of the regenerator. In addition this property can be used to greatly reduce the time required to run an experiment. For instance Case 1 and 2 converged to the same result, however, Case 1 reached steady state faster. Also, at times, it is desirable to run a sequence of experiments in a short time. Based on these results, it is possible to start an experiment immediately after a previous one, as long as the rail has been thermally preconditioned to result in a steady-state temperature near T_H. Indeed, the temperature span persisting in the regenerator from the previous test is

not expected to affect the final result. Such a temperature span also allows for steady state to be attained in a shorter time than if the experiment was to start from a pseudo-homogeneous temperature distribution. Further work is required to demonstrate that steady state performance is not influenced by initial conditions for the case of multi-material AMRs.

Chapter 6
Conclusions

This thesis has advanced the understanding of AMR refrigeration through a series of experiments using the AMR Test Apparatus. A number of hardware modifications contributed to making the device more reliable, flexible, and accurate. A finite element analysis model was created to estimate the heat leaks into the system due to bearing heating. The results suggested that, in order to produce consistent experiments, the final bearing temperature should not deviate by more than 2 K from a reference temperature (T_H) from test to test. In addition, a study of initial conditions suggested that, for the AMRs tested, the temperature distribution inside the regenerator at the beginning of the experiments does not affect the final result, as long as T_H, operating parameters, and heat leaks are consistent. A broad range of experiments were performed with the objective of characterizing single and multi-layer AMRs, paving a roadmap for AMRR optimization. The following sections summarize the findings and recommendations for future work.

6.1 Single Material Bed

Single puck AMR performance was characterized, where the characterization parameter was the temperature span. Single puck AMRs successfully produced a temperature span several times larger than the material MCE. It was found that temperature span is highly sensitive to the heat rejection temperature and is maximized when T_H is 10 to 15 K above T_{Curie}. T_{Hmax} also changes when operational parameters change (i.e. utilization, frequency). Cooling power decreases and heat load sensitivity increases rapidly if $T_H >> T_{Curie}$. Experiments suggest that the best results in terms of temperature span, heat load sensitivity and cooling power may be obtained if the heat rejection temperature is only a few degrees hotter than T_{Curie}.

Utilization, which is a function of the pressure of the a gaseous heat transfer fluid, has a large impact on performance. Results suggest that higher values could be used to increase temperature span and reduce heat load sensitivity. However, viscous losses also increase with utilization. Furthermore frequency has a great impact on cooling

power, and, indirectly, on temperature span. Sensitivities were found to be between 2.5 and 13 K/Hz.

Single material tests also showed that MCE alone is insufficient in predicting a material's performance. Indeed Gd, $Gd_{.74}Tb_{.26}$, and $Gd_{.85}Er_{.15}$ performed differently from what would be expected by only taking their respective MCE curves into account.

6.2 Layered Material Bed

Two puck regenerators created larger temperature spans than single puck AMRs. However, for Gd-Gd heat load sensitivity was found to be higher than that for Gd. Indeed, the larger temperature span causes the colder region of the AMR to operate further away from T_{Curie}, causing the material to operate in a region where the MCE is a weaker function of temperature. In addition, mass and aspect ratio have a large impact on performance. In general a higher profile (with larger mass) regenerator produces a larger temperature span with higher sensitivity to heat load, and larger pressure drop. For the no load case, it was observed that the maximum temperature span is obtained for warmer heat rejection temperatures than with single puck AMRs. Yet heat load sensitivity in this region increases significantly.

Material layering was implemented to overcome the issue of small cooling power contribution from the colder sections of the AMR. Larger temperature spans were obtained with the use of appropriate alloys and operating conditions. Multi-material AMRs may have a greater cooling capacity than single material AMRs over a limited range of temperature spans. If heat loads or other parameters drive the temperature of some of the layers away from their Curie point, the AMR performance is expected to deteriorate quickly.

Losses due to material discontinuity were observed. A qualitative analysis suggested that there may be a relation between the magnitude of the performance loss and the difference in Curie temperature between two adjacent layers.

The three layer AMR allowed reaching the largest temperature span to date in magnetic refrigeration. The result represents a milestone in the AMR performance because it was obtained with a relatively low field intensity (obtainable with permanent magnets), and small regenerator mass (the combined mass of the two regenerators is 270 g).

6.3 Recommendations

The experimental work performed with the AMRTA disclosed interesting results which may lead to technological opportunities. However, the results are often very specific to operating conditions. This is due to the non-linearity in the material properties and the size of the experimental space (the number of variables affecting the system).

At this time, a reliable numerical model simulating the conditions in the AMRTA is the most valuable tool to support the experimental work. Numerical work would help in the understanding of the physical interactions governing AMRs. Also, a simulation could be used as a predictive tool, replacing the experimental work for a number of scenarios, or even to explore operating conditions that cannot be performed with the available experimental apparatus.

Experimental results show that it is possible to further enhance the performance of the AMRs tested. Frequency, utilization, aspect ratio, regenerator microscale characteristics (particle size, shape, possibly syntherization, etc) should be investigated. More advanced work could also be conducted to improve regenerator geometry (conical AMR shapes, and individual layer length, since so far all layers were of the same size). Some of the preliminary work could be done using a numerical model to predict regenerator performance, so that the experimental work could target on a more focused pool of tests.

In the immediate future, experimental work should focus in comparing multi-layer multi-material and multi-layer single material AMRs. While the current work was mostly focused on no-load conditions, future work should explore a variety of heat load scenarios.

References

[1] Rowe, A., Tura A., Dikeos J., Chahine R, "Near Room Temperature Magnetic Refrigeration", *Proceedings of the International Green Energy Conference,* 12-16 June 2005, Waterloo, Ontario, Canada.

[2] Gschneidner, K.A., and Pecharsky, V.K., *Intermetallic Compounds:* Vol. 3, *Principles and Practise.* John Wiley, pp. 519, 2002.

[3] Rowe, A., "Active Magnetic Regenerators: Performance in the Vicinity of Para-Ferromagnetic Second Order Phase Transition" Ph.D. Thesis, University of Victoria, Victoria 2002.

[4] Yu, B.F., Gao, Q., Zhang, B., Meng, X.Z., Chen, Z., " Review on Research of Room Temperature Magnetic Refrigeration" *International Journal of Refrigeration,* vol. 26, pp 622-636, 2003.

[5] Green, G., Chafe, J., Stevens, J., Humphrey, J., " A Gadolinium-Terbium Active Magnetic Regenerator" in *Advances in Cryogenic Engineering*, vol.35, pp. 1165, 1990.

[6] Zimm, C., Johnson, J., Murphy, R.W., "Test Results on a 50 K Magnetic Refrigerator" in *Advances in Cryogenic Engineering*, vol. 41, pp 1675, 1996.

[7] Zimm, C., Jastrab, A., Sternberg, A., Pecharsky, V., Gschneidner, K., Osborne, M., Anderson, I., "Description and Performance of a Near-Room Temperature Magnetic Refrigerator" in *Advances in Cryogenic Engineering*, vol. 43, pp. 1759, 1998.

[8] Rowe, A., Tura, A., Richard, M-A., Chahine, R. and Barclay, J., "An Overview of Operating Experience Using the AMR Test Apparatus" in *Advances in Cryogenic Engineering* 49B, pp. 1721-1728, 2004.

[9] Gschneidner, K.A., and Pecharsky, V.K., Tsokol, A. O., "Recent Developments in Magnetocaloric Materials" *Rep. Prog. Phys.* 68 1479-1539, 2005.

[10] Richard, M.A., Rowe, A., Chahine, R., "Magnetic Refrigeration: Single and Multimaterial Active Magnetic Regenerator Experiments", J. Appl. Phys. 95, 2146, 2004

[11] Gschneidner, K.A., and Pecharsky, V.K., Ames Laboratory, Iowa State University, Ames, private communication, October 2005.

[12] Hall, J.L., Reid, C.E., Spearing, I.G., and Barclay, J.A., "Thermodynamic Considerations for the Design of Active Magnetic Regenerative Refrigerators", in *Advances in Cryogenic Engineering*, vol. 41, pp. 1653, 1996.

[13] Dikeos, J., "Development and Validation of an Active Magnetic Regenerator Cycle Simulation", MaSc Thesis, University of Victoria, Victoria 2006.

[14] Peksoy O., Rowe A., "Demagnetizing Effects in Active Magnetic Regenerators" Journal of Magnetism and Magnetic Materials, vol. 288, March 2005, pp. 424-432

[15] Rowe, A., and Barcklay, J. "Ideal Magnetocaloric Effect for Active Magnetic Regenerators" J. Appl. Phys. 93, pp.1672, 2003.

Appendix A - Instrumentation

The transducers are wired into a LabView data acquisition system where the analog signals are conditioned and multiplexed within a SCXI assembly and sampled by a PCI 6035E data acquisition (DAQ) board. The SCXI assembly includes a SCXI-1300 terminal block, SCXI-1102 module and SCXI-1000 chassis. The DAQ board interfaces with a pc and is responsible for the analog to digital conversion. The three major parameters identifying the performance of a DAQ board are sampling rate, resolution and range. The PCI 6035E card has 16 bit resolution, 200 ksamples/s sampling rate, and ±10 V voltage range. The sampling rate should always be at list twice the frequency of the signal of interest (Nyquist frequency) to avoid signal aliasing. If several channels are scanned (multiplexing), then the effective sampling rate is determined by dividing by the numbers of channels.

A Virtual Instrument (VI), a custom software program designed within the LabView environment, displays the voltages, converts them into appropriate physical quantities, displaying the output on the screen, and logging them by writing to an excel file. Figure A-1 illustrates a simplified flowchart summarizing the tasks performed by the VI. The grey area within the while loop represents the mathematical conversion of the digital voltage signal into the native units of the measured property. Table A-1 lists the transfer function for each of the transducers.

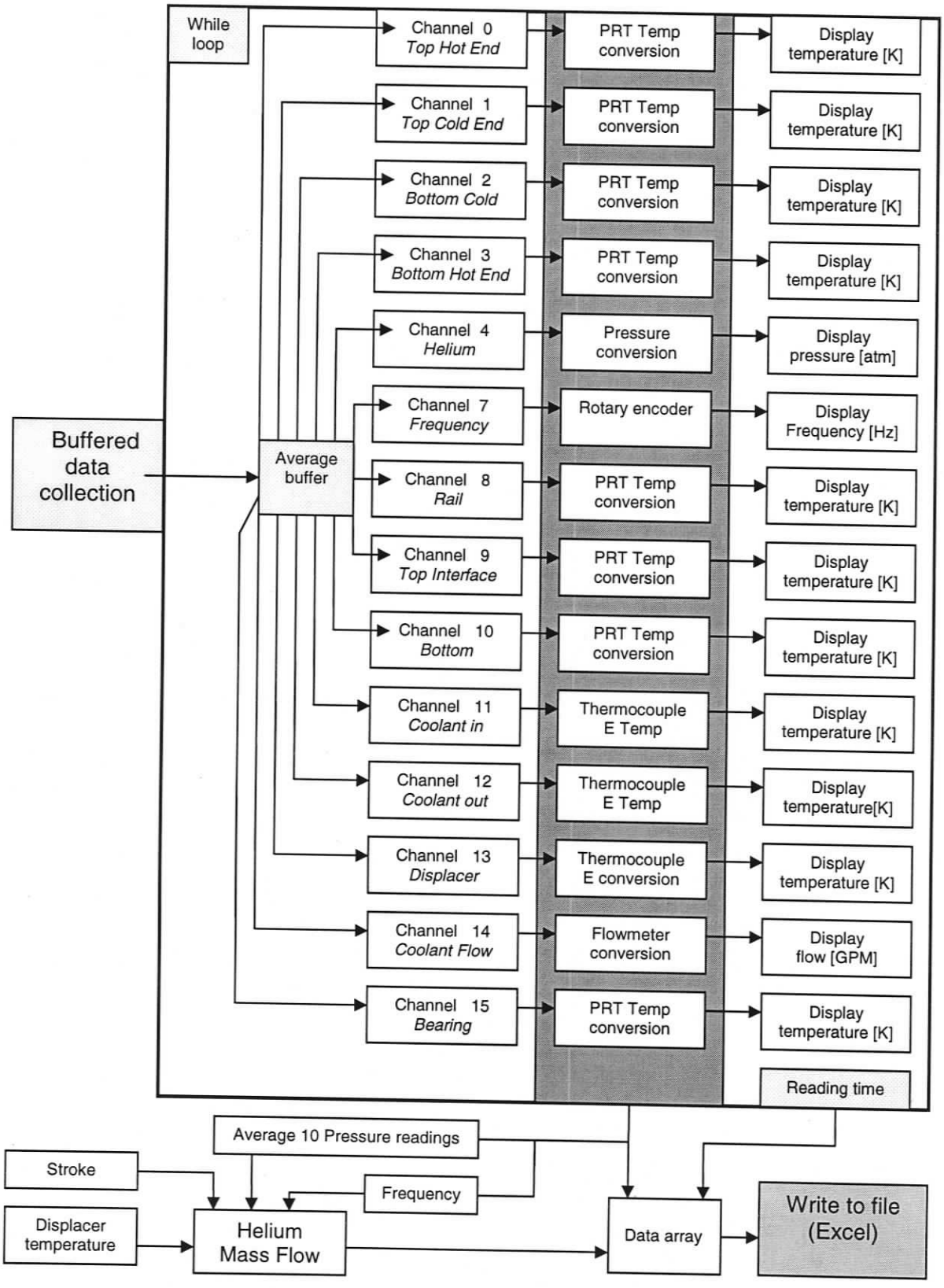

Figure A-1. LabView program flowchart.

Signals can be either continuously sampled or buffered. In other words the ADC can sample once, and then switch to the next channel obtaining a single value per channel every time, or buffer a number of readings (the number of scans to read each time are set by the user), before switching to the next channel. The advantage of the second sampling process is that each buffer read can be averaged reducing the noise level of the input. However buffering can significantly reduce sampling rate. The signals on the AMRTA oscillate at most at 1.2 Hz, and buffer size is generally set at 4000 readings, which allows a 5 Hz sampling rate, 4.17 times the Nyquist frequency. The program does not write to file on each iteration; instead its frequency is manually set by the user, generally at 2 or 4 seconds (0.5 or 0.25Hz). It is important that the write frequency is not a multiple of sampling speed and apparatus frequency, otherwise aliasing can occur.

Table A-1. Transducer transfer functions.

Transducer	*Transfer Function*	*Transducer Accuracy*
PRT [K]	$T = a_0 + a_1 \cdot R + a_2 \cdot R^2 - \frac{a_3}{R}$	±0.1% of resistance at 0°C ±0.13[K] at 0°C
Thermocouple E type [K]	$T = a_0 + v(a_1 + v \cdot a_2 + v \cdot a_3 + v \cdot a_4)))$	±1.3 [K] at 25°C
PX 603 Omega [atm]	$P = \frac{(a \cdot V - b)}{c}$	±0.4% BFSL
Rotary encoder [Hz]	$Hz = (a \cdot V - b) \cdot 2$	360 deg/1000

The PRT transfer function is directly obtained from manufacturer's data, which is ±0.1 K accurate. The function is valid from 325 K to 23 K with accuracy of ±0.3 K below 50K, ±0.1 below 30 K and ±0.4 K over the remaining working range. PRTs placed at the interfaces between pucks have extended leads, so that the wiring fits the regenerator shell (the voltage taps are not directly at the sensing element). Thus a sensor calibration was necessary to take into account the added wire resistivity. Calibration was obtained by comparing the PRTs to type E and K thermocouples at 20°C, 0°C and -22.5°C. It was also assumed that the wire resistivity does not change with temperature.

The thermocouples are standard Type E sensing elements. The SCXI-1300 terminal block features a cold-junction (compensation sensor) with a sensing accuracy of 1.3°C.

LabView software automatically sets up signal conditioning, including cold-junction compensation, amplification, and linearization for Type J, K, E, and T thermocouples.

The thin film pressure transducer requires an excitation voltage 10 to 30 Vdc and outputs 1 to 5 V linearly proportional to the sensed pressure in the 0 to 300 psig range.

Helium mass flow rate is not directly measured, it is instead calculated using frequency, pressure, temperature, displacer stroke and cross-sectional area. Helium mass flow rate is given by:

$$\dot{m}_{he} = \rho_{he} \cdot V \cdot A,$$

where $\dot{m}_{he}$ is helium mass flow rates, ρ_{he} is its density, V is the displacer velocity (averaged over a cycle), and A the cross sectional area of the displacer cylinder. In order to calculate the above expression, velocity and density need to be obtained first.
The ideal gas law determines the helium density:

$$\rho_{helium} = \frac{P}{(R/N) \cdot T},$$

where P is the gas pressure, R is the ideal gas constant, N is the molar density. The average velocity is obtained as follows:

$$V = \frac{l \cdot 2\pi \cdot f}{sqrt(2)},$$

where l is the crank arm length, and f the cycle frequency.

Appendix B- Sample Data Log

AMR M(kg)	He Cp (J/kg*K)	Reg Cp (J/kg*K)	Stroke (m)	Offset (deg)	mag(Tesla)	Gd
0.045	5200	381	0.21	0	2	

Absolute Time	Run Time (s)	PRT-TH (K)	PRT-TC (K)	PRT-BC (K)	PRT-BH (K)	Sys P (atm)
5:21:36 PM	2013.935	306.778	285.132	284.924	306.174	9.42
5:21:41 PM	2018.141	306.475	285.148	284.887	306.48	9.542
5:21:45 PM	2022.047	306.822	285.139	284.912	306.039	9.447
5:21:49 PM	2026.153	306.446	285.128	284.862	306.486	9.571
5:21:53 PM	2030.239	306.652	285.1	284.911	305.972	9.469
5:21:57 PM	2034.064	306.384	285.086	284.817	306.388	9.607
5:22:00 PM	2037.95	306.626	285.083	284.89	306.149	9.412
5:22:05 PM	2042.176	306.446	285.117	284.845	306.495	9.564
5:22:08 PM	2045.951	306.51	285.057	284.879	306.235	9.419
5:22:13 PM	2050.127	306.399	285.065	284.809	306.445	9.6
5:22:17 PM	2054.063	306.677	285.068	284.87	306.174	9.413
5:22:21 PM	2058.209	306.398	285.053	284.79	306.314	9.626
5:22:25 PM	2062.165	306.803	285.085	284.857	306.128	9.432
5:22:29 PM	2066.04	306.46	285.028	284.835	306.211	9.638
5:22:33 PM	2070.116	306.719	285.052	284.839	306.186	9.412
5:22:37 PM	2074.222	306.416	285.024	284.76	306.356	9.621
5:22:41 PM	2078.128	306.61	285.03	284.832	306.261	9.413
5:22:45 PM	2082.144	306.474	285.019	284.804	306.246	9.637
5:22:48 PM	2086.029	306.466	284.994	284.821	306.311	9.426
5:22:53 PM	2090.105	306.574	285.011	284.871	306.238	9.629
5:22:57 PM	2094.191	306.658	285.011	284.825	306.295	9.411
5:23:01 PM	2098.056	306.619	285.004	284.901	306.121	9.599
5:23:05 PM	2102.152	306.503	284.978	284.811	306.318	9.424
5:23:09 PM	2106.048	306.571	284.975	284.864	305.962	9.565
5:23:13 PM	2110.104	306.343	284.945	284.797	306.357	9.448
5:23:17 PM	2114.16	306.6	284.979	284.881	306.125	9.605
5:23:21 PM	2118.055	306.283	284.943	284.784	306.421	9.479
5:23:25 PM	2122.121	306.595	284.964	284.855	306.011	9.57
5:23:29 PM	2126.197	306.424	284.939	284.781	306.434	9.445
5:23:33 PM	2130.072	306.591	284.927	284.806	306.019	9.534
5:23:37 PM	2134.148	306.325	284.921	284.769	306.448	9.477
5:23:40 PM	2138.024	306.564	284.931	284.788	305.961	9.496
5:23:45 PM	2142.1	306.266	284.945	284.746	306.353	9.507
5:23:49 PM	2146.196	306.417	284.907	284.798	305.788	9.537
5:23:53 PM	2150.051	306.335	284.986	284.725	306.379	9.536
5:23:57 PM	2154.137	306.417	284.905	284.773	305.846	9.498
5:24:01 PM	2158.223	306.209	284.926	284.733	306.312	9.505
5:24:05 PM	2162.078	306.615	284.94	284.761	305.983	9.469
5:24:09 PM	2166.184	306.399	284.963	284.715	306.464	9.532
5:24:13 PM	2170.06	306.786	284.961	284.743	306.049	9.447

5:24:17 PM	2174.246	306.458	284.956	284.695	306.522	9.564
5:24:21 PM	2178.212	306.663	284.93	284.748	306.033	9.471
5:24:25 PM	2182.067	306.426	284.91	284.651	306.465	9.601
5:24:29 PM	2186.163	306.809	284.943	284.726	306.087	9.451
5:24:33 PM	2190.049	306.397	284.897	284.65	306.287	9.631
5:24:37 PM	2194.094	306.781	284.942	284.718	306.111	9.427
5:24:41 PM	2198.17	306.391	284.899	284.637	306.435	9.598
5:24:45 PM	2202.066	306.654	284.903	284.707	306.178	9.41
5:24:49 PM	2206.132	306.408	284.872	284.624	306.302	9.626
5:24:53 PM	2210.198	306.828	284.917	284.699	306.158	9.427
5:24:57 PM	2214.083	306.523	284.88	284.69	306.259	9.636
5:25:01 PM	2218.169	306.731	284.888	284.695	306.239	9.41
5:25:05 PM	2222.035	306.585	284.873	284.761	306.164	9.614
5:25:09 PM	2226.111	306.519	284.859	284.687	306.226	9.412
5:25:13 PM	2230.196	306.443	284.874	284.673	306.163	9.634
5:25:17 PM	2234.072	306.336	284.835	284.679	306.252	9.431
5:25:21 PM	2238.148	306.506	284.863	284.744	306.108	9.616
5:25:24 PM	2242.023	306.23	284.808	284.663	306.311	9.463
5:25:29 PM	2246.109	306.544	284.85	284.749	306.003	9.582
5:25:33 PM	2250.045	306.274	284.821	284.652	306.42	9.495
5:25:37 PM	2254.061	306.508	284.817	284.71	305.938	9.546
5:25:41 PM	2258.147	306.267	284.802	284.659	306.362	9.459
5:25:45 PM	2262.202	306.57	284.831	284.735	306.03	9.584
5:25:49 PM	2266.078	306.28	284.812	284.634	306.403	9.493
5:25:53 PM	2270.164	306.505	284.798	284.691	305.899	9.546
5:25:57 PM	2274.039	306.432	284.864	284.625	306.487	9.523
5:26:01 PM	2278.105	306.514	284.782	284.669	305.981	9.505
5:26:04 PM	2281.991	306.51	284.872	284.601	306.583	9.556
5:26:09 PM	2286.067	306.677	284.813	284.654	306.061	9.474
5:26:13 PM	2290.143	306.446	284.847	284.609	306.507	9.522
5:26:16 PM	2294.028	306.814	284.847	284.641	306.086	9.449
5:26:21 PM	2298.104	306.492	284.861	284.595	306.55	9.554
5:26:25 PM	2302.17	306.651	284.81	284.639	306.052	9.472
5:26:29 PM	2306.065	306.45	284.811	284.553	306.48	9.59
5:26:33 PM	2310.131	306.84	284.835	284.622	306.147	9.45
5:26:37 PM	2314.217	306.54	284.845	284.579	306.607	9.555
5:26:41 PM	2318.083	306.886	284.826	284.617	306.218	9.425
5:26:45 PM	2322.159	306.472	284.801	284.543	306.499	9.593
5:26:49 PM	2326.034	306.705	284.801	284.609	306.201	9.406
5:26:53 PM	2330.11	306.389	284.785	284.533	306.278	9.625
5:26:57 PM	2334.196	306.75	284.826	284.608	306.072	9.422
5:27:01 PM	2338.072	306.439	284.779	284.604	306.142	9.631
5:27:05 PM	2342.147	306.631	284.792	284.593	306.139	9.404
5:27:09 PM	2346.213	306.371	284.773	284.518	306.274	9.626
5:27:13 PM	2350.099	306.528	284.769	284.593	306.257	9.409
5:27:17 PM	2354.215	306.481	284.772	284.592	306.196	9.631
5:27:21 PM	2358.05	306.366	284.744	284.575	306.319	9.431
5:27:25 PM	2362.136	306.573	284.766	284.655	306.157	9.609
5:27:29 PM	2366.202	306.553	284.748	284.574	306.273	9.408
5:27:33 PM	2370.078	306.583	284.754	284.651	306.014	9.575

5:27:37 PM	2374.153	306.416	284.732	284.571	306.366	9.43
5:27:41 PM	2378.039	306.538	284.718	284.612	305.956	9.536
5:27:45 PM	2382.105	306.332	284.705	284.559	306.454	9.464
5:27:49 PM	2386.181	306.632	284.742	284.647	306.079	9.573
5:27:53 PM	2390.086	306.358	284.737	284.548	306.465	9.497
5:27:57 PM	2394.142	306.523	284.709	284.596	305.907	9.534
5:28:00 PM	2398.018	306.446	284.787	284.535	306.484	9.527
5:28:05 PM	2402.114	306.499	284.711	284.568	305.947	9.494
5:28:09 PM	2406.189	306.283	284.733	284.537	306.409	9.5
5:28:13 PM	2410.045	306.672	284.764	284.568	306.026	9.461
5:28:16 PM	2413.961	306.409	284.735	284.474	306.445	9.601
5:28:21 PM	2418.207	306.547	284.706	284.566	306.018	9.49
5:28:25 PM	2422.082	306.489	284.771	284.502	306.572	9.565
5:28:29 PM	2426.168	306.717	284.739	284.558	306.068	9.46
5:28:33 PM	2430.054	306.412	284.727	284.465	306.404	9.605
5:28:37 PM	2434.11	306.809	284.773	284.545	306.107	9.437
5:28:41 PM	2438.185	306.447	284.753	284.489	306.516	9.568
5:28:45 PM	2442.081	306.747	284.749	284.54	306.171	9.41
5:28:49 PM	2446.137	306.415	284.719	284.464	306.414	9.608
5:28:52 PM	2450.012	306.621	284.723	284.533	306.279	9.402
5:28:57 PM	2454.108	306.484	284.715	284.496	306.285	9.628
5:29:01 PM	2458.184	306.767	284.74	284.539	306.203	9.406
5:29:05 PM	2462.07	306.566	284.718	284.587	306.177	9.616
5:29:09 PM	2466.126	306.597	284.714	284.52	306.251	9.402
5:29:13 PM	2470.202	306.464	284.716	284.498	306.245	9.628
5:29:17 PM	2474.097	306.42	284.69	284.521	306.329	9.421
5:29:21 PM	2478.163	306.574	284.714	284.584	306.207	9.613
5:29:25 PM	2482.049	306.308	284.665	284.51	306.398	9.456
5:29:29 PM	2486.114	306.607	284.7	284.593	306.071	9.575
5:29:33 PM	2490.04	306.338	284.693	284.5	306.479	9.493
5:29:37 PM	2494.076	306.535	284.671	284.549	305.93	9.534
5:29:41 PM	2498.162	306.272	284.66	284.504	306.38	9.46
5:29:45 PM	2502.208	306.557	284.691	284.586	305.97	9.569
5:29:49 PM	2506.103	306.299	284.694	284.493	306.418	9.497
5:29:53 PM	2510.169	306.472	284.66	284.535	305.885	9.528
5:29:57 PM	2514.045	306.438	284.744	284.487	306.484	9.527
5:30:01 PM	2518.12	306.536	284.667	284.531	305.997	9.485
5:30:05 PM	2522.216	306.342	284.696	284.487	306.446	9.501
5:30:09 PM	2526.082	306.74	284.713	284.514	306.07	9.455
5:30:13 PM	2530.168	306.485	284.738	284.477	306.549	9.532
5:30:17 PM	2534.083	306.848	284.725	284.5	306.156	9.432
5:30:21 PM	2538.119	306.483	284.711	284.449	306.583	9.572
5:30:25 PM	2542.205	306.787	284.716	284.511	306.088	9.451
5:30:29 PM	2546.061	306.417	284.682	284.421	306.364	9.612
5:30:33 PM	2550.177	306.818	284.722	284.499	306.122	9.426
5:30:36 PM	2554.012	306.469	284.685	284.471	306.231	9.628
5:30:41 PM	2558.088	306.729	284.698	284.492	306.197	9.402
5:30:45 PM	2562.284	306.43	284.673	284.412	306.339	9.616
5:30:49 PM	2566.069	306.6	284.671	284.498	306.319	9.403
5:30:53 PM	2570.145	306.559	284.674	284.487	306.311	9.627

5:30:57 PM	2574.291	306.75	284.691	284.483	306.264	9.399
5:31:01 PM	2578.077	306.615	284.681	284.571	306.167	9.6
5:31:05 PM	2582.152	306.481	284.667	284.491	306.236	9.408
5:31:08 PM	2586.028	306.489	284.661	284.554	305.86	9.557
5:31:13 PM	2590.124	306.234	284.635	284.474	306.264	9.438
5:31:16 PM	2593.979	306.407	284.631	284.502	305.841	9.511
5:31:21 PM	2598.055	306.184	284.645	284.47	306.315	9.477
5:31:25 PM	2602.131	306.463	284.648	284.537	305.885	9.542
5:31:29 PM	2606.207	306.254	284.639	284.474	306.339	9.449
5:31:33 PM	2610.093	306.487	284.639	284.504	305.955	9.499
5:31:37 PM	2614.169	306.284	284.664	284.463	306.434	9.49
5:31:41 PM	2618.044	306.678	284.692	284.492	306.051	9.461
5:31:45 PM	2622.14	306.46	284.721	284.452	306.512	9.524
5:31:49 PM	2626.216	306.552	284.649	284.499	305.99	9.485
5:31:53 PM	2630.071	306.494	284.704	284.436	306.583	9.563
5:31:57 PM	2634.157	306.777	284.699	284.487	306.114	9.452
5:32:00 PM	2638.033	306.47	284.659	284.396	306.467	9.606
5:32:05 PM	2642.109	306.886	284.713	284.48	306.186	9.427
5:32:09 PM	2646.175	306.475	284.69	284.419	306.531	9.574
5:32:13 PM	2650.08	306.722	284.688	284.471	306.186	9.4
5:32:17 PM	2654.136	306.388	284.667	284.409	306.279	9.615
5:32:21 PM	2658.212	306.774	284.709	284.48	306.113	9.415
5:32:25 PM	2662.087	306.47	284.678	284.49	306.206	9.622
5:32:29 PM	2666.163	306.647	284.68	284.482	306.219	9.397
5:32:33 PM	2670.039	306.571	284.671	284.562	306.135	9.592
5:32:37 PM	2674.115	306.481	284.655	284.474	306.323	9.409
5:32:41 PM	2678.04	306.544	284.629	284.53	305.957	9.547
5:32:45 PM	2682.076	306.3	284.625	284.472	306.371	9.444
5:32:48 PM	2685.952	306.484	284.632	284.499	305.938	9.502
5:32:53 PM	2690.218	306.389	284.645	284.473	306.32	9.418
5:32:57 PM	2694.123	306.481	284.633	284.508	305.908	9.53
5:33:01 PM	2698.199	306.247	284.621	284.468	306.375	9.458
5:33:05 PM	2702.065	306.537	284.638	284.493	306.011	9.485
5:33:09 PM	2706.131	306.359	284.671	284.452	306.497	9.497
5:33:13 PM	2710.217	306.518	284.631	284.498	305.962	9.516
5:33:17 PM	2714.082	306.502	284.718	284.452	306.555	9.534
5:33:21 PM	2718.158	306.595	284.658	284.492	306.023	9.471
5:33:25 PM	2722.044	306.427	284.687	284.412	306.492	9.576
5:33:29 PM	2726.12	306.783	284.704	284.481	306.088	9.441
5:33:33 PM	2730.185	306.49	284.717	284.443	306.553	9.546
5:33:37 PM	2734.091	306.783	284.701	284.472	306.167	9.419
5:33:41 PM	2738.147	306.697	284.716	284.591	306.431	9.537
5:33:44 PM	2742.032	306.822	284.8	284.668	306.906	9.515
5:33:49 PM	2746.118	307.091	284.912	284.788	307.184	9.508
5:33:53 PM	2750.174	307.225	284.994	284.892	307.343	9.501
5:33:57 PM	2754.07	307.3	285.082	284.977	307.446	9.493
5:34:01 PM	2758.136	307.354	285.15	285.057	307.518	9.486
5:34:05 PM	2762.221	307.378	285.227	285.139	307.561	9.479
5:34:09 PM	2766.087	307.389	285.288	285.2	307.585	9.473
5:34:13 PM	2770.163	307.395	285.344	285.263	307.592	9.466

Encoder (Hz)	Rail T (K)	Water OUT(K)	Displacer T(K)	flow (GPM)	Cylinder T(K)	Mass (g/s)	Fi
0.658	313.508	304.703	300.546	1.108	306.56	1.219	0.253
0.639	313.533	304.661	300.545	1.104	306.697	1.182	0.252
0.64	313.549	304.671	300.54	1.105	306.621	1.185	0.253
0.625	313.558	304.7	300.533	1.09	306.638	1.155	0.252
0.664	313.588	304.714	300.528	1.103	306.603	1.229	0.253
0.624	313.599	304.73	300.524	1.102	306.677	1.154	0.252
0.642	313.611	304.728	300.536	1.109	306.641	1.19	0.253
0.626	313.637	304.778	300.542	1.783	306.681	1.158	0.252
0.633	313.647	304.832	300.548	1.798	306.688	1.173	0.253
0.635	313.665	304.854	300.552	1.786	306.701	1.173	0.252
0.619	313.682	304.882	300.557	1.796	306.717	1.147	0.253
0.628	313.702	304.869	300.56	1.772	306.72	1.161	0.252
0.635	313.723	304.914	300.571	1.793	306.718	1.176	0.253
0.623	313.743	304.904	300.576	1.792	306.747	1.152	0.252
0.623	313.754	304.916	300.592	1.801	306.76	1.153	0.253
0.633	313.77	304.943	300.595	1.788	306.789	1.169	0.252
0.606	313.79	304.971	300.605	1.796	306.79	1.123	0.253
0.623	313.816	305.003	300.607	1.806	306.791	1.152	0.252
0.596	313.824	304.996	300.613	1.793	306.828	1.104	0.253
0.63	313.85	304.912	300.606	1.795	306.816	1.165	0.252
0.604	313.862	304.899	300.602	1.802	306.877	1.117	0.253
0.648	313.882	304.881	300.597	1.801	306.855	1.198	0.252
0.598	313.906	304.913	300.599	1.802	306.879	1.107	0.253
0.673	313.919	304.951	300.594	1.798	306.853	1.245	0.252
0.601	313.937	305.015	300.589	1.797	306.908	1.113	0.253
0.645	313.952	305.085	300.589	1.793	306.894	1.193	0.252
0.616	313.97	305.118	300.591	1.794	306.963	1.14	0.253
0.67	313.984	305.02	300.595	1.801	306.898	1.239	0.252
0.633	314.009	304.772	300.598	1.795	307.007	1.17	0.252
0.69	314.024	304.593	300.598	1.801	306.873	1.277	0.253
0.614	314.049	304.488	300.599	1.794	307.004	1.136	0.253
0.688	314.052	304.514	300.593	1.799	306.874	1.272	0.253
0.632	314.081	304.572	300.587	1.774	307.051	1.168	0.252
0.689	314.102	304.665	300.586	1.804	306.917	1.274	0.253
0.635	314.106	304.796	300.585	1.796	307.051	1.174	0.252
0.689	314.129	304.862	300.585	1.81	306.92	1.274	0.253
0.634	314.142	304.894	300.585	1.796	307.022	1.172	0.252
0.665	314.157	304.914	300.582	1.8	306.967	1.23	0.253
0.635	314.185	304.923	300.582	1.789	307.111	1.173	0.252
0.642	314.201	304.923	300.58	1.807	307.025	1.189	0.253
0.634	314.22	304.878	300.578	1.796	307.085	1.171	0.252
0.633	314.228	304.835	300.581	1.794	307.061	1.172	0.253
0.632	314.247	304.803	300.574	1.793	307.077	1.167	0.252
0.644	314.261	304.811	300.577	1.798	307.079	1.192	0.253
0.629	314.286	304.834	300.576	1.797	307.115	1.162	0.252
0.633	314.295	304.9	300.579	1.802	307.125	1.172	0.253
0.632	314.317	304.957	300.577	1.8	307.148	1.168	0.252
0.617	314.336	305.015	300.577	1.798	307.169	1.143	0.253
0.629	314.354	304.991	300.581	1.797	307.174	1.162	0.252
0.601	314.374	304.861	300.588	1.805	307.219	1.113	0.253
0.627	314.398	304.737	300.583	1.793	307.222	1.159	0.252
0.619	314.411	304.67	300.587	1.789	307.226	1.145	0.253

0.64	314.428	304.67	300.577	1.798	307.26	1.183	0.252
0.602	314.44	304.718	300.575	1.794	307.278	1.114	0.253
0.66	314.463	304.782	300.57	1.806	307.282	1.221	0.252
0.597	314.483	304.866	300.573	1.793	307.325	1.104	0.253
0.684	314.499	304.896	300.571	1.802	307.261	1.265	0.252
0.607	314.518	304.88	300.567	1.802	307.386	1.124	0.253
0.659	314.525	304.879	300.567	1.799	307.346	1.218	0.252
0.596	314.548	304.865	300.564	1.793	307.391	1.104	0.253
0.684	314.566	304.862	300.557	1.805	307.324	1.264	0.252
0.608	314.589	304.868	300.557	1.794	307.451	1.124	0.253
0.689	314.605	304.874	300.556	1.788	307.326	1.275	0.253
0.626	314.617	304.917	300.555	1.796	307.512	1.157	0.252
0.669	314.636	304.948	300.55	1.796	307.377	1.237	0.253
0.633	314.649	304.935	300.547	1.798	307.548	1.17	0.252
0.689	314.678	304.845	300.539	1.803	307.405	1.275	0.253
0.633	314.692	304.788	300.536	1.805	307.529	1.169	0.252
0.669	314.702	304.791	300.534	1.793	307.452	1.238	0.253
0.633	314.728	304.802	300.529	1.795	307.614	1.17	0.252
0.645	314.732	304.836	300.526	1.811	307.528	1.194	0.253
0.633	314.751	304.914	300.518	1.806	307.598	1.169	0.252
0.669	314.776	304.964	300.519	1.8	307.541	1.238	0.253
0.634	314.789	304.987	300.511	1.791	307.605	1.172	0.252
0.643	314.81	304.889	300.513	1.802	307.598	1.191	0.253
0.629	314.825	304.7	300.513	1.797	307.642	1.162	0.252
0.633	314.846	304.603	300.512	1.795	307.652	1.172	0.253
0.634	314.865	304.575	300.518	1.796	307.68	1.172	0.252
0.617	314.881	304.612	300.524	1.809	307.71	1.142	0.253
0.629	314.902	304.668	300.521	1.796	307.726	1.162	0.252
0.633	314.914	304.737	300.525	1.803	307.742	1.172	0.253
0.63	314.924	304.814	300.522	1.786	307.788	1.164	0.252
0.618	314.95	304.853	300.528	1.8	307.807	1.144	0.253
0.643	314.968	304.827	300.529	1.803	307.838	1.187	0.252
0.6	314.979	304.861	300.537	1.809	307.868	1.111	0.253
0.63	315.002	304.865	300.536	1.8	307.873	1.164	0.252
0.598	315.023	304.867	300.536	1.796	307.922	1.106	0.253
0.642	315.032	304.915	300.536	1.807	307.927	1.186	0.252
0.611	315.056	304.972	300.545	1.793	307.992	1.13	0.252
0.665	315.075	305.021	300.548	1.793	307.957	1.229	0.252
0.599	315.094	305.019	300.546	1.797	308.008	1.108	0.253
0.685	315.113	304.904	300.542	1.788	307.947	1.266	0.252
0.61	315.13	304.786	300.542	1.79	308.086	1.129	0.252
0.685	315.149	304.724	300.538	1.811	307.964	1.268	0.252
0.626	315.153	304.704	300.541	1.805	308.159	1.158	0.252
0.685	315.18	304.736	300.536	1.817	308.032	1.267	0.252
0.632	315.199	304.773	300.54	1.793	308.179	1.168	0.252
0.639	315.204	304.849	300.544	1.799	308.115	1.183	0.253
0.627	315.225	304.941	300.539	1.79	308.25	1.159	0.252
0.657	315.244	304.937	300.539	1.789	308.129	1.216	0.253
0.632	315.263	304.862	300.536	1.79	308.273	1.167	0.252
0.638	315.283	304.792	300.539	1.805	308.214	1.18	0.253
0.633	315.299	304.768	300.54	1.797	308.271	1.169	0.252
0.653	315.309	304.751	300.548	1.803	308.24	1.209	0.253
0.632	315.331	304.809	300.544	1.793	308.299	1.167	0.252
0.637	315.345	304.876	300.544	1.795	308.303	1.179	0.253
0.632	315.368	304.927	300.535	1.798	308.353	1.166	0.252

0.626	315.387	304.937	300.532	1.796	308.376	1.158	0.253
0.632	315.394	304.888	300.525	1.792	308.403	1.167	0.252
0.605	315.414	304.804	300.524	1.804	308.456	1.121	0.253
0.631	315.438	304.787	300.513	1.805	308.462	1.166	0.252
0.623	315.457	304.794	300.507	1.808	308.484	1.153	0.253
0.639	315.472	304.803	300.498	1.799	308.528	1.18	0.252
0.603	315.487	304.852	300.5	1.799	308.56	1.117	0.253
0.66	315.504	304.894	300.499	1.783	308.568	1.22	0.252
0.598	315.529	304.958	300.505	1.802	308.629	1.106	0.253
0.682	315.537	304.924	300.505	1.796	308.564	1.261	0.252
0.608	315.565	304.841	300.506	1.795	308.704	1.123	0.252
0.664	315.568	304.74	300.503	1.797	308.675	1.226	0.252
0.599	315.598	304.71	300.503	1.794	308.737	1.108	0.253
0.684	315.617	304.714	300.498	1.801	308.681	1.265	0.252
0.61	315.631	304.731	300.506	1.798	308.819	1.127	0.252
0.684	315.655	304.766	300.503	1.802	308.703	1.265	0.252
0.624	315.669	304.832	300.503	1.788	308.902	1.154	0.252
0.686	315.693	304.86	300.501	1.797	308.778	1.268	0.252
0.63	315.696	304.858	300.506	1.798	308.931	1.164	0.252
0.681	315.722	304.888	300.504	1.809	308.825	1.259	0.252
0.634	315.737	304.906	300.499	1.807	308.938	1.17	0.252
0.653	315.75	304.922	300.502	1.799	308.931	1.208	0.253
0.63	315.769	304.868	300.503	1.789	309.035	1.164	0.252
0.638	315.79	304.793	300.505	1.794	308.992	1.18	0.253
0.634	315.81	304.753	300.501	1.782	309.048	1.171	0.252
0.624	315.828	304.755	300.505	1.801	309.082	1.156	0.253
0.632	315.844	304.785	300.502	1.79	309.109	1.167	0.252
0.637	315.863	304.83	300.507	1.785	309.122	1.179	0.253
0.632	315.878	304.917	300.506	1.799	309.184	1.168	0.252
0.62	315.895	304.998	300.506	1.813	309.216	1.148	0.253
0.631	315.916	304.962	300.501	1.805	309.234	1.164	0.252
0.6	315.936	304.771	300.499	1.801	309.298	1.109	0.253
0.634	315.955	304.605	300.496	1.801	309.317	1.171	0.252
0.599	315.968	304.52	300.495	1.794	309.372	1.108	0.252
0.649	315.993	304.502	300.489	1.8	309.375	1.199	0.252
0.612	316.012	304.53	300.492	1.792	309.469	1.131	0.252
0.673	316.022	304.598	300.483	1.802	309.392	1.243	0.252
0.601	316.05	304.728	300.487	1.802	309.516	1.111	0.252
0.655	316.055	304.786	300.489	1.8	309.498	1.21	0.252
0.617	316.081	304.774	300.493	1.797	309.605	1.141	0.252
0.679	316.106	304.792	300.486	1.821	309.518	1.255	0.252
0.629	316.118	304.799	300.481	1.797	309.648	1.161	0.252
0.682	316.137	304.797	300.481	1.791	309.54	1.26	0.252
0.621	316.163	304.845	300.484	1.787	309.742	1.148	0.252
0.657	316.173	304.884	300.488	1.8	309.641	1.214	0.253
0.631	316.193	304.949	300.489	1.799	309.777	1.166	0.252
0.639	316.203	304.975	300.493	1.804	309.732	1.183	0.253
0.634	316.224	304.936	300.485	1.789	309.794	1.17	0.252
0.649	316.243	304.815	300.489	1.802	309.79	1.2	0.253
0.633	316.258	304.699	300.487	1.793	309.849	1.169	0.252
0.636	316.286	304.642	300.487	1.798	309.877	1.177	0.253
0.634	316.307	304.649	300.486	1.796	309.912	1.171	0.252
0.616	316.317	304.688	300.489	1.795	309.962	1.14	0.253
0.631	316.342	304.751	300.481	1.797	309.989	1.165	0.252
0.598	316.361	304.837	300.481	1.797	310.055	1.106	0.253

0.634	316.374	304.898	300.476	1.812	310.087	1.17	0.252
0.6	316.399	304.876	300.482	1.798	310.15	1.109	0.252
0.654	316.417	304.811	300.479	1.799	310.155	1.207	0.252
0.615	316.437	304.774	300.478	1.802	310.256	1.136	0.252
0.639	316.452	304.75	300.471	1.807	310.226	1.18	0.252
0.603	316.479	304.745	300.47	1.798	310.308	1.115	0.252
0.662	316.487	304.774	300.465	1.804	310.282	1.222	0.252
0.62	316.511	304.794	300.466	1.802	310.414	1.145	0.252
0.681	316.527	304.899	300.465	1.805	310.28	1.258	0.252
0.608	316.545	304.908	300.472	1.793	310.453	1.124	0.252
0.677	316.567	304.817	300.474	1.806	310.353	1.251	0.252
0.624	316.586	304.731	300.478	1.798	310.542	1.152	0.252
0.649	316.602	304.737	300.485	1.802	310.458	1.2	0.253
0.63	316.619	304.761	300.482	1.792	310.563	1.163	0.252
0.668	316.638	304.777	300.479	1.806	310.5	1.235	0.252
0.591	316.654	304.83	300.476	1.787	310.583	1.091	0.252
0.298	316.671	304.856	300.469	1.803	310.646	0.551	0.252
0.007	316.697	304.855	300.438	1.796	310.671	0.013	0.252
0.007	316.715	304.866	300.399	1.789	310.707	0.013	0.252
0.007	316.737	304.853	300.361	1.786	310.735	0.013	0.252
0.007	316.756	304.828	300.325	1.11	310.774	0.013	0.252
0.007	316.78	304.827	300.291	1.1	310.818	0.013	0.252
0.007	316.802	304.84	300.254	1.102	310.854	0.013	0.252
0.007	316.816	304.874	300.218	1.103	310.889	0.013	0.252
0.007	316.829	304.892	300.179	1.107	310.926	0.013	0.252